VILNIUS UNIVERSITY
CENTER FOR PHYSICAL SCIENCES AND TECHNOLOGY

ŠARŪNAS SVIRSKAS

LATTICE DYNAMICS AND ELECTROMECHANICAL RESPONSE IN DISORDERED PEROVSKITES

Doctoral dissertation
Physical Sciences, Physics (02P)

Vilnius 2018

Dissertation was prepared in Vilnius University during 2014-2018

Scientific supervisor – prof. habil. dr. Jūras Banys (Vilnius University, physical sciences, physics – 02P)

VILNIAUS UNIVERSITETAS
FIZINIŲ IR TECHNOLOGIJOS MOKSLŲ CENTRAS

ŠARŪNAS SVIRSKAS

GARDELĖS DINAMIKA IR ELEKTROMECHANINIS ATSAKAS NETVARKIUOSE PEROVSKITUOSE

Daktaro disertacija
Fiziniai mokslai, fizika (02P)

Vilnius 2018

Disertacija parengta Vilniaus universitete 2014 – 2018 metais.

Mokslinis vadovas – prof. habil. dr. Jūras Banys (Vilniaus Universitetas, fiziniai mokslai, fizika – 02P)

ACKNOWLEDGEMENTS

I would mostly like to acknowledge my parents Vanda and Robertas and my sister Gendvilė for the patience and unprecedented support throughout the study years.

A large gratitude goes to my supervisor prof. Jūras Banys who believed in me and made these years an extraordinary journey through unexplored vastness of many complex physical problems. I would also like to thank prof. Robertas Grigalaitis, dr. Jan Macutkevič, dr. Andrius Džiaugys, dr. Martynas Kinka for the excellent collaborations in several projects. I thank doc. dr. Maksim Ivanov for the scepticism, great ideas and never ending scientific discussions in the laboratory since the beginning of my scientific career.

The great appreciation goes to my friends and colleagues Džiugas Jablonskas, Mantas Šimėnas, Ieva Kranauskaitė and Sergejus Balčiūnas who shared a pain of being a PhD student.

This work would not have crystallized without the collaborators whom I met throughout the years. I would like to thank dr. Eriks Birks, dr. Marija Dunce, prof. Seiji Kojima, prof. Jan Suchanicz and prof Jan Petzelt for excellent samples they have provided.

I also greatly acknowledge the opportunities to perform the experiments away from Vilnius University. I greatly thank the crew of Institute of Physics of Czech Academy of Sciences, especially dr. Stanislav Kamba, dr. Tatyana Ostapchuk, dr. Jan Pokorny, dr. Dmitry Nuzhny and dr. Elena Buixaderas. I thank dr. Vladimir Shvartsman and prof. Doru Lupascu for helping me to fulfill my ideas with their excellent experimental facilities in University of Duisburg-Essen. I also appreciate prof. Algimantas Kežionis, prof. Valdas Šablinskas, doc. dr. Tomas Šalkus, dr. Algirdas Selskis who helped/allowed me to perform the experiments in their laboratories.

I thank the staff of Faculty of Physics who always did an amazing work and kept great atmosphere. It is a great experience to be part of this organisation.

Finally, I bow my head to my great friends. I am grateful to Laurynas L., Mindaugas V., Marius J., dr. Evaldas Š., Vytautas S., Ignas M., Gabija K., Laurynas M., Renata M., Arnoldas J., Benas M., Tomas A. for the time spent away from the scientific world.

Table of Contents

Abbreviations

AC – alternating current
DC – direct current
PT – lead titanate
PNR(s) – polar nanoregion(s)
NBT – sodium bismuth titanate
PMN – lead magnesium niobate
PMN-xPT lead magnesium niobate – lead titanate
PZT – lead zirconate titanate
FTIR – fourier transform infrared spectroscopy
PFM – piezoresponse force microscopy
RF(s) – random field(s)
XRD – X-Ray diffraction
(Z)FC – (zero) field cooling
(Z)FH – (zero) field heating

1. Introduction

Defects are the cornerstone that bridges solid state physics and materials science to the novel technological applications. Strict control of defects and their states in a solid state matter offers a powerful tool to tune physical properties (i. e. conductivity, mechanical properties, etc.) of the materials. This was a key aspect in developing the semiconductor electronics to the level it has reached nowadays. Furthermore, the defect chemistry plays a crucial role in other types of materials.

Perovskite oxides are a very important class of materials. The flexibility of the oxygen octahedral system provides many degrees of freedom and tuning possibilities for different kinds of properties. Perovskite oxides can possess very attractive properties such as ferroelectricity, high piezoelectricity, high ionic conductivity etc. Sometimes it is even possible to have multiple ferroic orders simultaneously.

The extensive studies of perovskite oxides started with a ground-breaking discovery of the first inorganic ferroelectric barium titanate[1]. It was quickly identified that barium titanate possesses a very strong piezoelectric effect. The superior piezoelectricity is due to the ferroelectricity and high spontaneous polarization in barium titanate[2,3]. Consequently, other perovskite oxides such as lead titanate were sintered and identified as ferroelectric material.

Later on, studies were concentrated on more complex materials to meet the requirements for practical applications. The versatility of the octahedral system was exploited and the studies from the conventional ferroelectrics were focused on the substituted perovskite oxides. The possibility to introduce different kinds of transition metal ions in the B-site of the perovskite lattice offered many new possibilities. Sintering of so far unbeatable piezoelectric ceramics lead zirconate titanate revolutionized the piezoelectric applications. The complex solid solutions of perovskite oxides revealed exciting phase diagrams with a very robust behaviour.

The substitutional disorder in the perovskite lattice promoted a new phenomenon (a new type of ferroelectric behaviour) widely known as relaxor ferroelectricity (a material referred to as a relaxor). Relaxors were considered as ‘dirty’ displacive ferroelectrics[4] where the long range ferroelectric order is suppressed by the internal random fields. The random fields which arise due to the charge and/or site disorder seem to be the key to understanding the complicated nature of relaxor ferroelectrics[5].

Nowadays, lead-based complex perovskite oxides demonstrate the largest piezoelectric response but the requirement for environmentally friendly materials drives the studies of low-lead containing compounds. Development of lead-free materials is one of the rapidly growing branches of ferroelectricity. The performance of lead-free materials was particularly increased due to the very complex substitutions in the perovskite lattice, which usually has 2 or 3 counterparts and forms exotic and complex phase diagrams[6].

It is evident that perovskite oxides offer a lot of interesting physical phenomena but the essential driving force for further investigations is several important application fields. One of them is the medical ultrasound where the excellent piezoelectric properties of perovskites were utilized for diagnosis on the daily basis. Furthermore, the precise positioning/actuation systems cannot be acomplished without the unique electromechanical properties of perovskite ferroelectrics. Different substitutional ions in the perovskite lattice enable to obtain the high-power generation of ultrasonic waves which is the key ingredient for hidrolocation. Finally, the possibility of polarization switching together with a novel domain wall engineering abilities should enable modern microelectronic devices for telecommunications and computing.

This work is devoted to the investigation of several complex perovskite oxides where the random fields occur due to the charge disorder in A or B site of the perovskite lattice. The experimental investigation is focused on the lattice dynamics and ferroelectric/piezoelectric response of these materials. Combination of such experimental data gives all the necessary information relevant for technological applications and reveals the contribution of the complex chemical nature to the dielectric and electromechanical properties.

1.1 The objectives of the work

The main aim of the thesis is to investigate the macroscopic properties related to the phase transitions in some disordered perovskite oxides via broadband dielectric and vibrational spectroscopies. Another aim is finding the relation between the macroscopic ferroelectric/electromechanical properties and the local polarization patterns and revealing the role of disorder depending on the site where it is present. Several potentially perspective perovskite oxides which were not previously investigated were chosen.

The following goals were formulated in order to achieve the aims of the thesis:

- To investigate the dielectric properties of sodium bismuth titanate (NBT) single crystals in a broad temperature and frequency range;
- To investigate the impact of Mn and Cr dopants on the dielectric properties of NBT single crystals;
- To investigate the dielectric properties of NBT ceramics at microwave frequencies. To determine the contributions of phonons and central peak to the dielectric permittivity;
- To investigate the presence of the ferroelectric order in PMN-17PT single crystals;
- To investigate the lattice dynamics and the relaxor-ferroelectric crossover in the phase diagram of $(0.4\text{-}y)Na_{0.5}Bi_{0.5}TiO_3\text{-}0.6SrTiO_3\text{-}yPbTiO_3$ solid solutions;
- To investigate the electromechanical properties of $(0.4\text{-}y)Na_{0.5}Bi_{0.5}TiO_3\text{-}0.6SrTiO_3\text{-}yPbTiO_3$ and $0.4Na_{0.5}Bi_{0.5}TiO_3\text{-}(0.6\text{-}x)SrTiO_3\text{-}xPbTiO_3$ solid solutions;
- To investigate the local polarization and piezoelectric response of $(0.4\text{-}y)Na_{0.5}Bi_{0.5}TiO_3\text{-}0.6SrTiO_3\text{-}yPbTiO_3$ solid solutions by Piezoresponse force microscopy;

- To compare $(0.4\text{-}y)Na_{0.5}Bi_{0.5}TiO_3\text{-}0.6SrTiO_3\text{-}yPbTiO_3$ solid solutions with some canonical relaxor-$PbTiO_3$ solid solutions;

1.2 Statements presented for the defense

- The dielectric properties of sodium bismuth titanate ($Na_{0.5}Bi_{0.5}TiO_3$) are determined by the anharmonicity and the peculiar bismuth ion dynamics. This A-site disorder perovskite oxide cannot be classified as a relaxor ferroelectric.
- $0.83PbMg_{1/3}Nb_{2/3}O_3\text{-}0.17PbTiO_3$ single crystals undergo spontaneous phase transition. The lattice dynamics of this crystal resembles order-disorder phase transitions.
- The crossover from relaxor to ferroelectric properties is observed in $Na_{0.5}Bi_{0.5}TiO_3\text{-}SrTiO_3\text{-}PbTiO_3$ solid solutions. The different substitutional species at the A-site do not affect the electromechanical properties. The dielectric anomalies are related to the relaxation mode.

1.3 Scientific novelty

- The microwave dielectric properties of sodium bismuth titanate are reported in a wide temperature range (300-800 K);
- The influence of Mn and Cr doping to the conductivity and dielectric properties of NBT single crystals is reported;
- The origin of high temperature dielectric anomaly was explained in NBT;
- The dielectric spectra were investigated in the $0.83PbMg_{1/3}Nb_{2/3}O_3\text{-}0.17PbTiO_3$ (PMN-17PT) single crystals with an intermediary strength of random fields;
- Polarization/strain hysteresis and pyroelectric properties were investigated in $0.83PbMg_{1/3}Nb_{2/3}O_3\text{-}0.17PbTiO_3$ (PMN-17PT) single crystals;

- Local piezoelectric response was investigated in $0.83PbMg_{1/3}Nb_{2/3}O_3$-$0.17PbTiO_3$ (PMN-17PT) single crystals;
- The relaxor to ferroelectric crossover was investigated in (0.4-*y*)$Na_{0.5}Bi_{0.5}TiO_3$-$0.6SrTiO_3$-$yPbTiO_3$ solid solutions via broadband dielectric spectroscopy for the first time;
- The compositional dependence of electromechanical properties was investigated in $Na_{0.5}Bi_{0.5}TiO_3$-$SrTiO_3$-$PbTiO_3$ solid solutions;
- Local polarization response of $Na_{0.5}Bi_{0.5}TiO_3$-$SrTiO_3$-$yPbTiO_3$ was investigated and linked to the morphology and macroscopic properties.

1.4 Publications related to the thesis

1. J. Petzelt, D. Nuzhnyy, V. Bovtun, M. Pasciak, S. Kamba, R. Dittmer, Š. Svirskas, J. Banys, J. Roedel "Peculiar Bi-ion dynamics in $Na_{1/2}Bi_{1/2}TiO_3$ from terahertz and microwave dielectric spectroscopy", *Phase transitions*, vol. 87(10-11), 953-965 (2014); DOI: https://doi.org/10.1080/01411594.2014.953517
2. Š. Svirskas, J. Banys, S. Kojima "Broadband dielectric spectroscopy of Pb-based relaxor ferroelectric (1-x)$Pb(Mg_{1/3}Nb_{2/3})O_3$-$xPbTiO_3$ with intermediate random fields“, *Journal of Applied Physics*, vol. 121, 134101 (2017); DOI: https://doi.org/10.1063/1.4979729
3. Md Al Helal, Md Aftabuzzaman, S. Svirskas, J. Banys, S. Kojima "Temperature evolution of central peaks and effect of electric field in relaxor ferroelectric $0.83Pb(Mg_{1/3}Nb_{2/3})O_3$-$0.17PbTiO_3$ single crystals", *Japanese Journal of Applied Physics*, vol. 56(10s), 10PB03 (2017); DOI: https://doi.org/10.7567/JJAP.56.10PB03
4. Š. Svirskas, M. Dunce, E. Birks, A. Sternberg, J. Banys "Electromechanical properties of $Na_{0.5}Bi_{0.5}TiO_3$-$SrTiO_3$-$PbTiO_3$ solid solutions", *Journal of Physics and Chemistry of Solids*, vol. 114, 94-99 (2018); DOI: https://doi.org/10.1016/j.jpcs.2017.11.007

5. Š. Svirskas, D. Jablonskas, V. Samulionis, S. Kojima, J. Banys “Is there a spontaneous ferroelectric phase transition in $0.83PbMg_{1/3}Nb_{2/3}O_3$-$0.17PbTiO_3$ single crystal?” *Journal of Alloys and Compounds*, vol. 748, 127-133 (2018); DOI: https://doi.org/10.1016/j.jallcom.2018.03.130
6. J. Suchanicz, Š. Svirskas, M. Ivanov, A. Kežionis, J. Banys “Ferroelectric, Dielectric and Optic properties of Mn and Cr doped $Na_{0.5}Bi_{0.5}TiO_3$ single crystals”, *Ferroelectrics* (accepted 2018);
7. Š. Svirskas, V. Shvartsman, M. Dunce, R. Ignatans, E. Birks, T. Ostapchuk, S. Kamba, D. Lupascu, J. Banys “Two-Phase Dielectric Polar Structures in 0.1NBT-0.6ST-0.3PT Solid Solutions”, *Acta Materialia*, vol. 153, 117-125 (2018); DOI: https://doi.org/10.1016/j.actamat.2018.04.052

1.5 Other publications (2014-2018)

1. J. Belovickis, J. Macutkevic, Š. Svirskas, V. Samulionis, J. Banys, O. Shenderova, V. Borjanovic “Dielectric spectroscopy of polymer based PDMS nanocomposites with ZnO nanoparticles“, *Ferroelectrics*, vol. 479, 82-89 (2015); DOI: https://doi.org/10.1080/00150193.2015.1012016
2. V. Samulionis, Š. Svirskas, J. Banys, A. Sanchez-Ferrer, A. Mrzel “Ultrasonic and Dielectric Studies of Polyurea Elastomer Composites with Inorganic Nanoparticles“, *Ferroelectrics*, vol. 479, 67-75 (2015); DOI: https://doi.org10.1080/00150193.2015.1011979
3. V. Samulionis, Š. Svirskas, J. Banys, A. Sanchez-Ferrer, N. Gimeno, B. Ros „Phase Transitions in Smectic Bent-Core Main-Chain Polymer Networks Detected by Dielectric and Ultrasonic Techniques“ *Ferroelectrics*, vol. 479, 76-81 (2015); DOI: https://doi.org/10.1080/00150193.2015.1012011
4. Š. Svirskas, M. Šimenas, J. Banys, P. Martins, S. Lanceros-Mendez “Dielectric relaxation and ferromagnetic resonance in magnetoelectric (Polyvinylidene-fluoride)/ferrite composites”, *Journal of Polymer*

Research, vol. 22, 141 (2015); DOI: https://doi.org/10.1007/s10965-015-0780-9

5. A. Dziaugys, J. Macutkevic, S. Svirskas, R. Juskenas, M. Wencka, J. Banys, S. F. Motria, Yu. Vysochanskii “Maxwell–Wagner relaxation and anomalies of physical properties in $Cu_{0.15}Fe_{1.7}PS_3$ mixed material“, *Journal of Alloys and Compounds*, vol 650, 386-392 (2015); DOI: https://doi.org/10.1016/j.jallcom.2015.07.261
6. J. Belovickis, J. Macutkevič, S. Svirskas, V. Samulionis, J. Banys, O. Shenderova, V. Borjanovic “Ultrasonic and dielectric relaxations in PDMS/ZnO nanocomposite“, *Physica Status Solidi (B)*, vol. 252(12), 2778–2783 (2015); DOI: https://doi.org/10.1002/pssb.201552383
7. M. Silibin, J. Belovickis, S. Svirskas et al. „Polarization reversal in organic-inorganic ferroelectric composites: Modeling and experiment“, *Applied Physics Letters*, vol. 107(14), 142907 (2015); DOI: https://doi.org10.1063/1.4932661
8. I. Anusca, S. Balčiūnas, P. Gemeiner, Š. Svirskas, M. Sanlialp, G. Lackner, C. Fettkenhauer, J. Belovickis, V. Samulionis, M. Ivanov, B. Dkhil, J. Banys, V. V. Shvartsman, D. C. Lupascu, “Dielectric Response: Answer to Many Questions in the Methylammonium Lead Halide Solar Cell Absorbers”, *Advanced Energy Materials*, 1700600 (2017); DOI: https://doi.org/10.1002/aenm.201700600
9. Š. Svirskas, J. Belovickis, D. Šemeliovas, P. Martins, S. Lanceros-Méndez and J. Banys “Temperature and frequency dependence of dielectric and piezoelectric response of P(VDF–TrFE)/$CoFe_2O_4$ magnetoelectric composites“, *Lithuanian Journal of Physics*, Vol. 57(2), 103-111 (2017); DOI: https://doi.org/10.3952/physics.v57i2.3517
10. J. Belovickis, M. Ivanov, Š. Svirskas, V. Samulionis, J. Banys, A. Solnyshkin, S. Gavrilov, K. Nekludov, V. Shvartsman, M. Silibin “Dielectric, Ferroelectric, and Piezoelectric Investigation of Polymer-Based P(VDF-TrFE) Composites”, *Physica Status Solidi(B)*, vol. 255, 1700196-6 (2018); DOI: https://doi.org/10.1002/pssb.201700196

1.6 The list of conferences

1. A. Dziaugys, J. Macutkevic, S. Svirskas, R. Juskenas, J. Banys, A. F. Orliukas, Yu. Vysochanskii, “Dielectric, XRD and ultrasonic investigations of $Cu_{0.15}Fe_{1.7}PS_3$ mixed crystal”, in ECAPD-2014, Vilnius, Lithuania, p. 124, 7-11 July (2014);
2. A. Olšauskaitė, Š. Svirskas, M. Ivanov, T. Šalkus, A. Kežionis, J. Banys, M. Dunce, E. Birks, M. Antonova, A. Sternberg, “Broadband dielectric spectroscopy of $xNa_{0.5}Bi_{0.5}TiO_3$-$(1-x)Sr_{0.7}Bi_{0.2}TiO_3$ solid solutions”, in ECAPD-2014, Vilnius, Lithuania, p. 126, 7-11 July (2014);
3. J. Belovickis, J. Macutkevic, Š. Svirskas, V. Samulionis, J. Banys, O. Shenderova, “Dielectric spectroscopy of polymer based PDMS nanocomposites with ZnO nanoparticles”, in ECAPD-2014, Vilnius, Lithuania, p. 127, 7-11 July (2014);
4. V. Samulionis, Š. Svirskas, J. Banys, A. Sánchez-Ferrer, R. Mezzenga, “Ultrasonic and Dielectric Studies of Polyurea Elastomer Composites with Inorganic Nanoparticles”, in ECAPD-2014, Vilnius, Lithuania, p. 136, 7-11 July (2014);
5. V. Samulionis, Š. Svirskas, J. Banys, A. Sánchez-Ferrer, R. Mezzenga, N. Gimeno, M.B. Ros, „Phase Transitions in Polymers with Highly Ordered Liquid-Crystalline Phases,“ in ECAPD-2014, Vilnius, Lithuania, p. 137, 7-11 July (2014);
6. Š. Svirskas, J. Banys, M. Dunce, T. Ostapchuk, S. Miga, J. Dec, J. Pokorny, C. Kadlec, A. Sternberg, S. Kamba, “Relaxor behaviour in NBT-based solid solutions”, III Polish Lithuanian Ukranian meeting on ferroelectric physics, Wroclaw, Poland, p. O-INV-14, 31 August – 4 September (2014);
7. Š. Svirskas, T. Ostapchuk, M. Ivanov, J. Pokorny, M. Dunce, E. Birks, M. Antonova, J. Banys, S. Kamba, A. Sternberg, “Dielectric, IR and Raman Spectroscopies of $(0.4-y)Na_{0.5}Bi_{0.5}TiO_3$-$0.6SrTiO_3$-$yPbTiO_3$ Solid

Solutions”, Joint International Symposium RCBJSF – 2014 - FM&NT, Riga, Latvia, p. 154, 29 September-2 October (2014);

8. J. Belovickis, J. Macutkevic, Š. Svirskas, V. Samulionis, J. Banys, O. Shenderova, “Ultrasonic Wave Propagation in PDMS with ZnO Nanoparticles”, Joint International Symposium RCBJSF – 2014 - FM&NT, Riga, Latvia, p. 351, 29 September-2 October (2014);
9. A. Olsauskaitė, S. Svirskas, M. Ivanov, T.Salkus, A.Kezionis, J. Banys, M. Dunce, E. Birks, M. Antonova, A. Sternberg, “Dielectric relaxation in $xNa_{0.5}Bi_{0.5}TiO_3$-$(1-x)Sr_{0.7}Bi_{0.2}TiO_3$“, International workshop on relaxor ferroelectrics, Stirin, Czech republic, p. 51, 12-16 October (2014);
10. A. Olšauskaitė, Š. Svirskas, J. Banys, M. Dunce, E. Birks, M. Antonova, A. Sternberg, “Dielectric relaxation in $xNa_{0.5}Bi_{0.5}TiO_3$-$(1-x)Sr_{0.7}Bi_{0.2}TiO_3$ solid solutions”, in 41st Lithuanian national physics conference, Vilnius, Lithuania, p. 248, 17-19 June (2015);
11. Š. Svirskas, A. Olšauskaitė, M. Ivanov, J. Banys, T. Šalkus, M. Dunce, E. Birks, M. Antonova, A.Sternberg, “Two relaxation components in lead-free $(1-x)Na_{0.5}Bi_{0.5}TiO_3$-$xSr_{0.7}Bi_{0.2}TiO_3$ solid solutions”, 13th European meeting on Ferroelectricity, Porto, Portugal, p. 6A_2O, 28 June-3 July (2015);
12. Š. Svirskas, J. Banys, T. Ostapchuk, C. Kadlec, J. Pokorny, S. Kamba, M. Dunce, E. Birks, M. Antonova, A. Sternberg, “Broadband dielectric spectroscopy of relaxors. Case of $(0.4-y)Na_{0.5}Bi_{0.5}TiO_3$-$0.6SrTiO_3$-$yPbTiO_3$ solid solutions”, 13th European meeting on Ferroelectricity, Porto, Portugal, p. 6 B_1I, 28 June-3 July (2015);
13. J. Belovickis, Š. Svirskas, M. Ivanov, V. Samulionis, J. Banys, M.V. Silibin, A.V. Solnyshkin, S.A. Gavrilov, A.A. Dronov, “Ultrasonic and dielectric spectroscopy of polymer based PVDF-TrFE composites with PZT fillers”, 13th European meeting on Ferroelectricity, Porto, Portugal, p. 7B_3O, 28 June-3 July (2015).
14. J. Belovickis, V. Samulionis, S. Svirskas, M. Ivanov, J. Banys, M. V. Silibin, S. Lanceros-Mendez, “Ferroelectric and ultrasonic studies on

polymer based P(VDF-TrFE) composites with PZT, BTO and CFO inclusions", 5th International workshop smart materials and structures, Marrakesh, Morocco, p. 138, 9-12 September (2015).

15. J. Banys, S. Svirskas, M. Dunce, E. Birks, A. Sternberg, S. Kamba, "Broadband dielectric spectroscopy of A-substituted relaxor ceramics", International symposium of dynamical properties of solids DyProSo XXXV, Freising, Germany, p. 101, 13-17 September (2015).
16. V. Samulionis, J. Belovickis, S. Svirskas, M. Ivanov, J. Banys, M. V. Silibin, S.Lanceros-Mendez, "Effect of CFO and PZT fillers on dielectric and ultrasonic properties of P(VDF-TrFE) copolymer based composites", International symposium of dynamical properties of solids DyProSo XXXV, Freising, Germany, p. 117, 13-17 September (2015);
17. S. Svirskas, M. Dunce, E. Birks, A. Sternberg, J. Banys, "Electromechanical properties of $Na_{0.5}Bi_{0.5}TiO_3$-$SrTiO_3$-$PbTiO_3$ solid solutions", conference "Functional materials and nanotechnologies" Vilnius, Lithuania, p. 201, 5-8 October (2015);
18. J. Belovickis, S. Svirskas, V. Samulionis, M. Ivanov, J. Banys, M. V. Silibin, S. A. Gavrilov, K. N. Nekludov, A. V. Solnyshkin, V. V. Shvartsman, "Investigation of dielectric and ultrasonic behavior of PVDF based polymer composites with ferroelectric fillers", conference "Functional materials and nanotechnologies" Vilnius, Lithuania, p.203, 5-8 October (2015);
19. S. Svirskas, J. Banys, T. Ostapchuk, S. Kadlec, J. Pokorny, S. Kamba, M. Dunce, E. Birks, M. Antonova A. Sternberg, "Broadband dielectric spectroscopy of relaxors. Case of (0.4-y)$Na_{0.5}Bi_{0.5}TiO_3$-0.6$SrTiO_3$-y$PbTiO_3$ solid solutions", 5th seminar Properties of ferroelectric and superionic systems, Uzhgorod, Ukraine, p.6, 26-27 October (2015);
20. S. Svirskas, M. Dunce, E. Birks, A. Sternberg, J. Banys, "Electromechanical properties of $Na_{0.5}Bi_{0.5}TiO_3$-$SrTiO_3$-$PbTiO_3$ solid solutions", conference "Functional materials and nanotechnologies" Vilnius, Lithuania, p.201, 5-8 October (2015).

21. J. Belovickis, S. Svirskas, V. Samulionis, M. Ivanov, J. Banys, M. V. Silibin, S. A. Gavrilov, K. N. Nekludov, A. V. Solnyshkin, V. V. Shvartsman, "Investigation of dielectric and ultrasonic behavior of PVDF based polymer composites with ferroelectric fillers", conference "Functional materials and nanotechnologies" Vilnius, Lithuania, p.203, 5-8 October (2015).
22. S. Svirskas, J. Banys, T. Ostapchuk, S. Kadlec, J. Pokorny, S. Kamba, M. Dunce, E. Birks, M. Antonova A. Sternberg, "Broadband dielectric spectroscopy of relaxors. Case of (0.4-y)$Na_{0.5}Bi_{0.5}TiO_3$-0.6$SrTiO_3$-y$PbTiO_3$ solid solutions", 5th seminar Properties of ferroelectric and superionic systems, Uzhgorod, Ukraine, p.6, 26-27 October (2015);
23. J. Banys, S. Svirskas, M. Dunce, E. Birks, M. Antonova, A. Sternberg, "Broadband dielectric spectroscopy of A-site substituted relaxor ceramics", International Chemical congress of Psific Basin Societies, Honolulu, Hawaii, USA, p. 272, 15-20 December (2015);
24. S. Svirskas, J. Banys, A. Kezionis, M. Dunce, E. Birks, T. Ostapchuk, J. Pokorny, S. Kamba, "Dielecric, IR and Raman spectroscopic studies of NBT based solid solution", Fundamental Physics of Ferroelectrics and related materials, Washington, USA, p. 31 January-3 February (2016);
25. J. Belovickis, M. Ivanov, S. Svirskas, J. Banys, M. Silibin, A. V. Solnyshkin, V. V. Shvartsman, "Dielectric and Ferroelectric Investigation of P(VDF-TrFE)-based Composites", Joint 13th International Symposium RCBJSF – international workshop on relaxor ferroelectrics, Matsue, Japan, p. 10, 19-23 June (2016);
26. J. Banys, A. Sakanas, C. E. Ciomaga, L. Curecheriu, V. Buscaglia, M. M. Vijatović Petrovic, R. Grigalaitis, M. Ivanov, S. Svirskas, D. Jablonskas, L. Mitoseriu, J. D. Bobic, B. D. Stojanovic, S. Kamba, "Multiferroic Composites", Joint 13th International Symposium RCBJSF – international workshop on relaxor ferroelectrics, Matsue, Japan, p. 17, 19-23 June (2016);

27. S. Svirskas, M. Ivanov, J. Banys, Md. Al Helal, T. Mori, S. Kojima, “Broadband Dielectric Spectroscopy of $0.83Pb(Mg_{1/3}Nb_{2/3})O_3$-$0.17PbTiO_3$ Single Crystal”, Joint 13th International Symposium RCBJSF – international workshop on relaxor ferroelectrics, Matsue, Japan, p. 23, 19-23 June (2016);
28. S. Svirskas, J. Banys, M. Dunce, E. Birks, A. Sternberg, “Dielectric, Infrared and Raman Studies of Lead-Free $xNa_{0.5}Bi_{0.5}TiO_3$-$(1-x)Sr_{0.7}Bi_{0.2}TiO_3$ Solid Solutions”, Joint 13th International Symposium RCBJSF – international workshop on relaxor ferroelectrics, Matsue, Japan, p. 23, 19-23 June (2016);
29. S. Svirskas, J. Banys, V. V. Shvartsman, D. Lupascu, M. Dunce, E Birks, R. Ignatans, “Peculiarities of relaxor to ferroelectric phase transition in $0.1Na_{0.5}Bi_{0.5}TiO_3$-$0.6SrTiO_3$-$0.3PbTiO_3$ solid solutions”, in Joint IEEE ISAF ECAPD PFM, Darmstadt, Germany, p. 22, 21-25 August (2016);
30. S. Svirskas, J. Banys, V. V. Shvartsman, D. Lupascu, M. Dunce, E. Birks, R. Ignatans, „Phase transition in $0.1Na_{0.5}Bi_{0.5}TiO_3$-$0.6SrTiO_3$-$0.3PbTiO_3$ solid solutions,” IVth Lithuanian Ukrainian Polish conference, LUP IV, Palanga, Lithuania, p. 20, 5-9 September (2016).
31. J. Belovickis, M. Ivanov, S. Svirskas, J. Banys, M. V. Silibin, A. V. Solnyshkin, V. V. Shvartsman, “Dielectric and ferroelectric investigation of P(VDF-TrFE)-based composites”, E-MRS Fall Meeting, Warsaw, Poland, p. 353, 19-22 September (2016);
32. J. Banys, S. Svirskas, D. Jablonskas, S. Lapinskas, S. Rudys, R. Grigalaitis, “Measurement of electrical properties of materials at microwaves”, 6th Seminar Properties of ferroelectric and superionic systems, Uzhhorod, Ukraine, p. 8, 17-18 November (2016);
33. J. Belovickis, M. Ivanov, S. Svirskas, J. Banys, M. V. Silibin, A. V. Solnyshkin, V. V. Shvartsman, “Dielectric and ferroelectric investigation of P(VDF-TrFE)-based composites”, 6th Seminar Properties of ferroelectric and superionic systems, Uzhhorod, Ukraine, p. 12, 17-18 November (2016);

34. M. A. Helal, M. Aftabuzzaman, S. Tsukada, S. Svirskas, M. Ivanov, J. Banys, S. Kojima, “Inelastic light scattering studines on relaxor ferroelectric $0.83Pb(Mg_{1/3}Nb_{2/3})O_3-0.17PbTiO_3$ single crystal”, Fundamental physics of ferroelectrics and related materials, Williamsburg, USA, p. 101-102, 29 January-1 February (2017);
35. S. Svirskas, J. Banys, S. Kojima, „Relaxor to ferroelectric phase transitionin $0.83PbMg_{1/3}Nb_{2/3}O_3-0.17PbTiO_3$ single crystal,“ Materiais 2017, Aveiro, Portugal, p 222, 9-12 April (2017);
36. S. Svirskas, J. Banys, S. Kojima, „Phase transitions in perovskite oxides with heterovalent substitutions: case of PMN-0.17PT single crystal,“ Modern Multifunctional Materials and Ceramics, Vilnius, Lithuania, p. 17, 19-20 April (2017);
37. S. Svirskas, J. Banys, S. Kojima, “Relaxor to ferroelectric phase transition in $0.83PbMg_{1/3}Nb_{2/3}O_3-0.17PbTiO_3$ single crystals”, FM&NT-2017, Tartu, Estonia, p 130, 24-27 April (2017);
38. S. Svirskas, J. Banys, S. Kojima, “Relaxor to ferroelectric phase transition in $0.83PbMg_{1/3}Nb_{2/3}O_3-0.17PbTiO_3$ single crystal,” IEEE ISAF IWATMD PFM, Atlanta, USA, p.II59, 7-11 May (2017);
39. S. Svirskas, M. Dunce, E. Birks, A. Sternberg, S. Kamba, J. Banys, “Phase transitions and dielectric dispersion in $(0.4-y)Na_{0.5}Bi_{0.5}TiO_3-0.6SrTiO_3-yPbTiO_3$ solid solutions”, International conference on Electroceramics, Nagoya, Japan, p. 88, 28-31 May (2017);
40. Š. Svirskas, D. Jablonskas, S. Kojima, J. Banys “Ferroelectricity in PMN-17PT single crystals”, RCBJSF-2018, St. Petersburg, Russia, p. 75, 14-18 May (2018).

1.7 Authors’ contribution

All experimental data that is presented on the sodium bismuth titanate single crystals was gathered by the author. The analysis of the data was also carried out by the author. The microwave dielectric properties of NBT ceramics were also performed by the author. The publications related to these results were prepared by the author in collaboration with prof. Jan Petzelt and prof. Jan Suchanicz.

The dielectric, ferroelectric, piezoelectric and PFM experiments, analysis and the preparation of publications on PMN-17PT single crystal were performed by the author (except for the paper on Raman and Brillouin scattering).

The experimental data on $(0.4\text{-}y)\mathrm{Na_{0.5}Bi_{0.5}TiO_3}\text{-}0.6\mathrm{SrTiO_3}\text{-}y\mathrm{PbTiO_3}$ and $0.4\mathrm{Na_{0.5}Bi_{0.5}TiO_3}\text{-}(0.6\text{-}x)\mathrm{SrTiO_3}\text{-}x\mathrm{PbTiO_3}$ solid solutions was obtained by the author. Some of the data was already published in the master thesis of the author (Svirskas, Š. “Trinariai perovskitai su A-srities kompozicine netvarka: dielektrinė ir Ramano spektroskopijos”, Vilnius, 2014). FTIR and Raman spectroscopic experiments were performed in the Institute of Physics of the Academy of Sciences of Czech Republic in 2014. The supervisor was dr. Stanislav Kamba.

All piezoresponse force microscopy images were obtained in the Institute of Materials Science, University of Duisburg-Essen. The work of the author was supervised by dr. Vladimir Shvartsman. Three weeks were spent in the facility by the author to obtain the experimental results. The analysis of the images was performed by the author under the supervision of dr. Vladimir Shvartsman.

2. Overview

The fundamental knowledge necessary to understand the interpretation of experimental results is presented in this chapter. The goal of the chapter is to present the basis of the theory so the less experienced reader would have the basic ideas behind the physics of the work. The chapter is concentrated on general concepts with some characteristic examples to emphesize the complexity of the topic.

The particular features and relevant physical properties of the investigated materials are presented together with experimental results (i. e. Chapter 4).

2.1 Perovskite oxides

The chemical formula of conventional perovskite oxides is ABO_3. The oxygen anions form an octahedral cage. The B-site cation lies inside the oxygen octahedra. A-site cation takes place between the network of oxygen octahedra. The perovskite lattice is depicted in Figure 2.1.1.

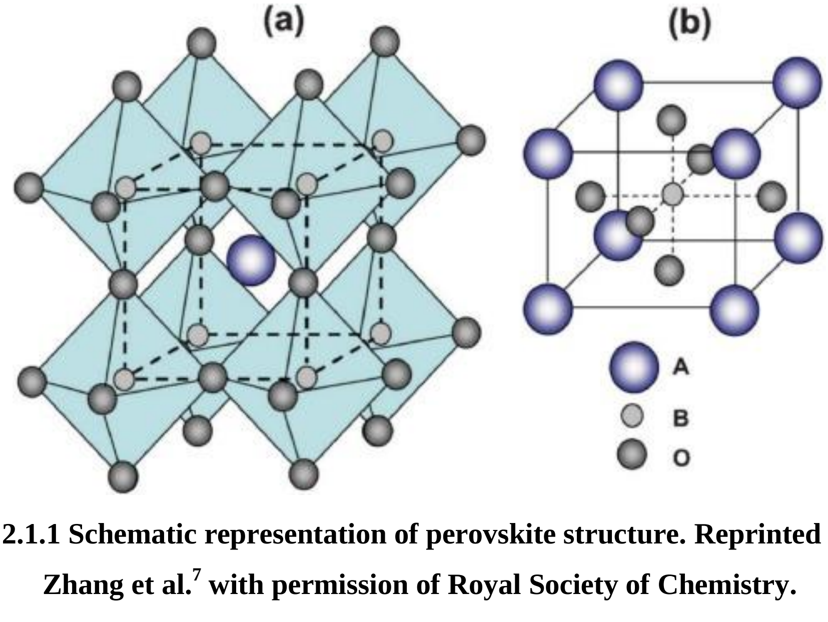

Figure 2.1.1 Schematic representation of perovskite structure. Reprinted from K. Zhang et al.[7] with permission of Royal Society of Chemistry.

The sum of valence of cations must be 6+ to satisfy the charge neutrality in the perovskite lattice. The most classical ferroelectrics consist of 2+ valence and 4+ valence ions at the A and B-sites respectively.

The perovskite lattice is quite flexible. The different perovskite sites can host a wide variety of cations. The space group of the lattice depends on the cation radii. The different sizes of cations can induce many different physical properties. If the small cation like titanium is placed at the B-site, it tends to off-center from its ideal position. This causes spontaneous polarization to occur. Thus, the pyroelectric, piezoelectric and ferroelectric properties can occur in such lattices. The larger ions also tend to distort the oxygen octahedral. This leads to various oxygen tilting modes which are of antiferrodistortive nature[8,9].

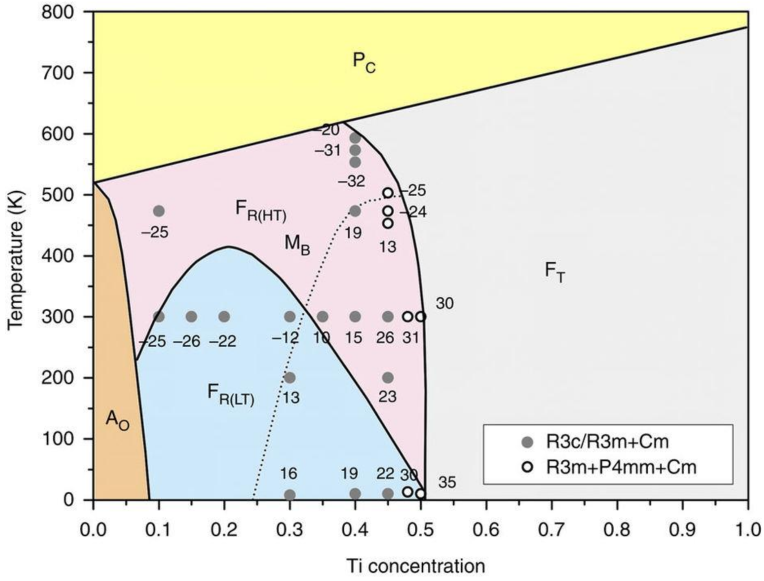

Figure 2.1.2 Phase diagram of lead zirconate - lead titanate ($PbZr_{1-x}Ti_xO_3$). Reprinted by permission from Springer Customer Service Centre GmbH: Springer Nature, Nature Communications from N. Zhang et al.[10], copyright (2014).

Another attractive feature is the possibility to produce mixed systems where several different cations can host A and/or B-sites simultaneously. This offers a lot of possibilities to tune physical properties by combining quite different features of the perovskite oxides. One of the most exciting phase diagrams of the solid state physics is well renowned mixture between antiferroelectric lead zirconate ($PbZrO_3$) and ferroelectric lead titanate

($PbTiO_3$). The richness of that phase diagram is presented in Figure 2.1.2. Zirconium and titanium ions possess a valence of 4+ in the perovskite lattice. There are no restrictions of compositional ratio of Zr and Ti ions. It is possible to sinter any composition throughout the phase diagram. One of the most important features of such phase diagrams is so called morphotropic phase boundary. This is a narrow concentration region where the lattice does not possess the structure of the end members of phase diagram. The complicated mixed structure can occur. Sometimes, new lower symmetry phase can appear (i. e. usually, it is monoclinic). The MPB of lead zirconate titanate is in the vicinity of 50:50 Zr:Ti ratio. It is evident from the Figure 2.1.2 that the phase diagram is quite robust and can possess various physical properties.

It is possible to introduce cations with a different valence in the perovskite lattice. It induces defects (particularly oxygen vacancies). It alters the domain wall mobility in ferroelectric perovskite oxides. It might also increase the oxygen ion conductivity which is relevant for the solid oxide fuel cells. The doping levels are quite low and the phase diagrams are not studied extensively. Sometimes it is even hard to identify the valence states of the dopants (ocassionally some cations even have a mixed valence states).

A particular interest is focused on the disordered perovskite oxides where different valence species occupy the same lattice sites. The charge disorder is introduced in the perovskite lattice and it produces many fascinating physical phenomena. Both ions have a different valence than the ideal 4+ ion. Thus, in order to preserve the charge neutrality, these ions should arrange in some particular manner. One of the examples is a canonical relaxor $PbMg_{1/3}Nb_{2/3}O_3$ (PMN). The Mg and Nb ions have valences of 2+ and 3+ respectively. In order to have a charge balance the ratio of Nb:Mg ions should be 2:1. This ratio corresponds to the effective valence of 4+. Unfortunately, the ordering in such materials is not properly understood. According to some studies, it is not possible to achieve full ordering in some materials (like PMN). The regions with a 2:1 Nb:Mg ratio exists but other regions have a disorder of these two ions[11]. The perfect ordering could be reach in the system where the ratio between B site ions is 1:1. One of the examples is lead scandium niobate ($PbSc_{1/2}Nb_{1/2}O_3$)[12,13]. The perfect 1:1 ordering can be achieved by anealling and/or quenching procedure. It was shown that perfectly ordered and disordered samples have drastically different macroscopic properties[12–14].

Further chapters will mainly focus on the physical properties and main features of both classical and disordered perovskite oxides. The phenomenon related to ferroelectricity will be presented and discussed.

2.2 Ferroelectricity

Ferroelectricity is a phenomenon which is an electrical analogue to the ferromagnetism. One of the most important features of ferroelectricity is the occurrence of permanent dipole moment (or polarization) in the material. This is not sufficient condition for the material to be classified as a ferroelectric. Another important requirement is the ability to control the direction of polarization by an external electric field. If this requirement is not satisfied than the material is considered to be only pyroelectric. This is a functional definition of ferroelectricity[15].

N. Setter stressed an important structural aspect which was also known previously[15]: the material is a ferroelectric if it underwent the structural phase transition from symmetric parental phase to a lower non-centrosymmetric phase whose polar directions are linked to each other by the lost symmetry operations of parental phase. This means that in order to have a ferroelectric material you must have a structural phase transition.

The ferroelectric phase transitions can be described by Landau-type phenomenological theory. In this case it is another analogy to the ferromagnetism since macroscopically this phenomenon can be described in the same manner as ferromagnets if the proper order parameter is chosen. The polarization in proper ferroelectrics is proportional to the order parameter. There are two boundary definitions of the order parameter in ferroelectrics. First one is the displacement of some atoms from its ideal centrosymmetric positions. These types of ferroelectrics are called displacive ones. The displacement of the atoms in the symmetric phase is absent while below the phase transition temperature the displacement becomes non-zero.

The second type is the ordering of some atoms or their groups. In this case the material can be well described by the multi-well potential. The atoms can occupy one of these positions. At the symmetric phase both of these positions are equivalent, so statistically the atoms occupy both positions in the same manner and thus order parameter is zero. Below the phase transition temperature one of the positions starts to dominate and order parameter becomes non-zero.

Both of these microscopic models of ferroelectricity can be described with an anharmonic potential[16]. In this sense the difference between these models is related to the different height of potential barrier between the equivalent positions relative to the energy kT_C (k is Boltzmann constant and T_C – phase transition temperature).

The distinction between order-disorder and displacive type ferroelectrics is not trivial. The difference between these two boundary cases can be identified by the investigation of the static dielectric. The expansion of thermodynamic potential of a ferroelectric phase transition in terms of order parameter is described by the following equation[17]:

$$G(T,E,p) = \frac{1}{2}\alpha(T-T_C)\eta^2 + \frac{1}{4}\beta\eta^4 + \cdots - a\eta E \qquad (2.2.1)$$

Where G – is the free energy, η – order parameter; T – temperature; T_c – phase transition temperature; α, β – expansion coefficients; aη – polarization; E – electric field. From this equation it is possible to determine the temperature dependence of the static dielectric permittivity (the second derivative of the thermodynamic potential with respect to an electric field):

$$\varepsilon = \frac{C_{CW}}{T-T_C} \qquad (2.2.2)$$

This is the Curie-Weiss law which is also applicable for the magnetic susceptibility in ferromagnets. This equation can give a hint to the type of phase transition. The Curie-Weiss constant C_{CW} determines the height of the potential barrier and yields the information about the phase transition mechanism. For the displacive type ferroelectrics this constant is much larger than for the order-disorder ones.

2.3 Lattice dynamics in perovskite oxides

The ferroelectricity is considered to occur due to the instability of the zone center phonon mode. This means that the eigenfrequency of the lowest frequency mode tends to zero when the phase transition temperature is approached. The fundamental work of the Cochran[18] revealed that the temperature dependence of the squared frequency of the lowest frequency TO phonon is linear vs. temperature:

$$\omega_s^2 = A(T - T_C) \tag{2.3.1}$$

By combining the Cochran law (Eq. 2.3.1) with Lyddanne-Sachs-Teller relation[19] it is possible to arrive to the Curie-Weiss law for the static dielectric permittivity (Eq. 2.2.2).

The conventional perovskite oxides (barium titanate, lead titanate, strontium titanate and others) usually have a high temperature cubic phase (space group $Pm\bar{3}m$). Most of the materials which will be studied belong to the same space group at the highest temperatures. There is one formula unit in the primitive lattice of this space group. This means that there are 5 atoms which need to be considered. So there are $3N$ ($N = 5$) vibrational degrees of freedom. The cubic perovskite oxide has 15 phonons. There are 3 acoustic modes and 12 optical modes. The optical modes belong to the $3F_{1u}$ and $1F_{2u}$ modes. Both of these optical modes are triply degenerate. The F_{1u} symmetry modes are only IR active. F_{2u} mode is weakly polar and thus not detectable with the infrared techniques. The cubic perovskite structure under consideration supposed not to have Raman active modes.

The graphical representation of the normal vibrations in the cubic phase is depicted in Figure 2.3.1. The vibrations of titanium ions against the oxygen octahedral are called the Slater mode (Figure 2.3.1 (a)). Another vibration where the whole oxygen cage vibrates against the A-site framework is called the Last mode (Figure 2.3.1 (b)). The bending of oxygen octahedral, the Axe mode is depicted in the Figure 2.3.1 (c)[20].

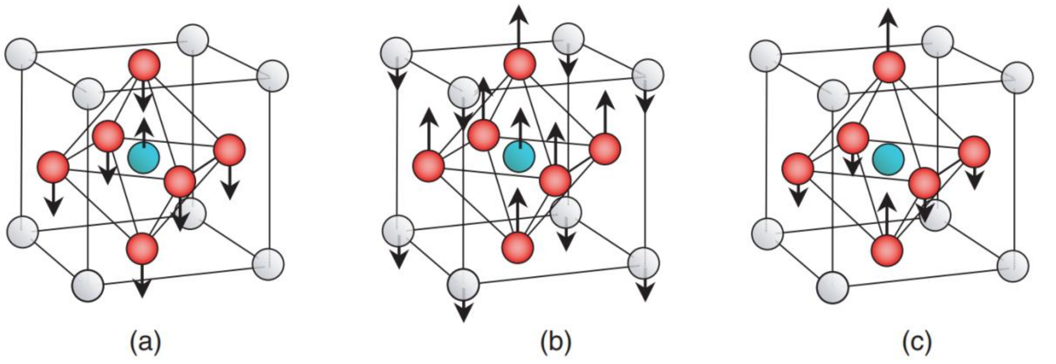

Figure 2.3.1 Normal vibrations of cubic perovskite oxide. (a) Slater mode; (b) Last mode; (c) Axe mode. The picture is taken from Hlinka et al.[21]

The ferroelectric instabilities can be related to either Slater or Last modes. The lowest frequency phonon is of Last-type in lead-based perovskite oxides while the Slater mode is of lowest frequency in a non-Pb perovskite oxides (note the references by Hlinka et al.[15,16]). When the cubic phase transforms to a tetragonal, each F_{1u} mode splits into $3A_1$ +3E modes. The soft mode is of A_1 (the displacements of the vibration should be along the polarization axis) and exhibit softening in the tetragonal phase. All the A_1 + E pairs are both Raman and IR active. Vibrations with no center of inversion is both Raman and IR active.

The other type of instability is related to the relaxation mode (it is often considered as the heavily overdamped phonon). The phase transition occurs due to the critical slowing down of the dipolar relaxation. The temperature dependence of relaxation time in the framework of the mean-field theory can be expressed as follows[23]:

$$\tau \sim \tau_0 \frac{T-T_C}{T_C} \tag{2.3.2}$$

The instability of phonons does not play an important role in the order-disorder phase transitions. The dielectric properties of such phase transition has a well pronounced dielectric relaxation at the microwave frequencies. When the probing frequency becomes lower than $\frac{1}{2\pi\tau_0}$ the minimum in the temperature dependences of dielectric permittivity is observed.

The two ferroelectric instabilities mentioned above are only the theoretical limits. The real cases of the phase transitions in perovskite oxides are much more complicated. It is quite difficult to find the purely displacive or order-disorder system in the perovskite oxides. There are many experimental evidences with a theoretical justification which show the coexistence of order-disorder and displacive type dynamics[22,24–27]. Usually, the coupling between the lowest frequency phonon and the relaxation mode is observed in the vicinity of the phase transitions. Such complexity is promoted in complex perovskite oxides with substitutional disorder.

2.4 Relaxor ferroelectrics

The main features of relaxor ferroelectrics will be reviewed in this section. A lot of properties will be discussed in the framework of the relaxor PMN which is the most extensively studied relaxor material. It is considered to be a canonical relaxor system.

Relaxor ferroelectrics is a special class of ferroic materials which macroscopically are cubic[28] and do not show any spontaneous ferroelectric phase transitions. Relaxor ferroelectric properties are primarily caused by the substitutional disorder in the perovskite lattice[11,29,30]. In other words, the disorder (site, charge) is mandatory for the relaxor properties to occur.

Many peculiar properties of relaxors were observed. Relaxors are considered to be of displacive type since the underdamped polar phonon experiences softening above the Burns temperature[31,32]. Thus, relaxors were initially classified as ‘dirty’ displacive ferroelectrics[4].

The peculiarities concerning relaxors started piling since the early studies. Burns and Dacol observed the birefringence occurring in relaxors at certain temperature[33]. Birefringence should not occur in cubic crystals. The appearance of birefringence and deviation of linear dependence of refractive index[34] indicated that some kind of polarization fluctuations occur. These polarization fluctuations were associated to the microscopic polar entities referred to as polar nanoregions (PNRs). The main feature of the polar nanoregions is that they are dynamical entities, not static ones. Thus, they should be distinguished from (nano)domains. This is one of the most debatable concepts in relaxor physics. PNRs can only be observed by indirect experiments. It is considered that they appear at Burns temperature where their size is only several unit cells. PNRs grow with the decrease of temperature up to several nanometers[35–37]. One of the direct observations of these nanosized polar entities can be performed by Piezoresponse force microscopy. The labyrinth-like polar structures were identified in several relaxor systems[38–42]. These polar structures have a fractal nature which was also identified by different experimental techniques[43]. The idea of PNRs is quite vague and some opinions exist which dispute the necessity of such concept to describe the properties of relaxors[44].

One of the most fascinating properties of relaxors is their response to external electric fields. The main feature which distinguishes them from other ferroic systems is giant dielectric permittivity which is accompanied by the broad dielectric relaxation. The dielectric relaxation extends more than 10 orders of magnitude in frequency[45,46]. The temperature of the permittivity peak depends on the probing frequency (i. e. that is the maximum of real part of permittivity shifts to higher temperatures when the probing frequency is increased). Such behaviour is often referred as a diffuse phase transition despite the absence of any detectable structural changes. Firstly, the unique dielectric properties were explained by a superparaelectric model[47] which assumes the polar pseudospins embedded in a disordered matrix. At high temperatures the dielectric permittivity obeys a Curie-Weiss law. The deviation starts to appear below the Burns temperature[11] (although one should be cautious about the Burns temperature because there are many discrepancies in different experiments. Even some doubts can be found in the literature[48]).

Qualitatively, superparaelectric model can reproduce the dielectric behaviour but it fails in any other properties of relaxor ferroelectrics.

Relaxors have a close resemblance to the dipolar glasses. Thus, many properties were attributed to the glassiness of the system. Both of these materials undergo a collective freezing phenomenon. This means that some characteristic relaxation time diverges at a particular temperature T_{VF}. The freezing in relaxors have many similarities to dipolar glasses. It was evidenced by the broadband dielectric spectroscopy[49–54].

The dipolar glasses are materials which have a dipolar frustration in the lattice. This is usually achieved in the mixed systems of ferroelectrics and antiferroelectrics of order-disorder type[55]. The long ferroelectric range is suppressed by the frustration. This is one of the most important similarities between relaxors and dipolar glasses. On the other hand, relaxors are considered as a displacive systems[4]. The most significant distinction between these two types of materials is the possibility to induce the ferroelectric order by an external electric field[56]. The possibility to induce ferroelectric order in relaxors has been confirmed in several systems. This means that relaxor ground state is close to normal ferroelectrics. In the vicinity of low frequency permittivity peak, the ferroelectric phase persists even after removing an external electric field. Experimentally, this has not been achieved for the dipolar glasses.

The significant difference between dielectric relaxation in dipolar glasses and relaxors were also identified. It was shown that the distribution of relaxation times in these two systems is different[51,57]. The analysis of distribution of relaxation times revealed several contributions in relaxors as opposed to the dipolar glasses. Another important difference is the frequency range of relaxation which is much broader in the case of relaxors.

The theoretical background was developed for the glassy systems and can be quite well defined by the phenomenological theory[58–60]. The main idea of these models is that there is an interaction between the fixed length pseudospins which undergo freezing phenomenon, i. e. at the freezing temperature T_{VF} it occupies certain position which cannot be manipulated. The same ideas were applied for relaxor ferroelectrics[61]. The random fields random bonds model of dipolar glasses were extended for the relaxor ferroelectrics (i. e. Spherical random bonds random fields model of relaxor ferroelectrics)[62]. This model is based on the assumption that the rigid pseudospin is placed in the paraelectric matrix. The length of this pseudospin is fixed but it can take any direction on the sphere. This is a generalization of random bonds-random fields model and it can describe all three types of ferroic systems and crossover between them.

Spherical random bonds random fields model can explain the Pb and Nb NMR lineshapes observed in relaxors[63,64]. Unfortunately, this model fails to explain experimental results of nonlinear dielectric properties. According to the SRBRF, the scaled third order nonlinear susceptibility supposed to have maximum in the vicinity of the freezing temperature T_{VF} (as opposed to dipolar glasses where divergence is observed in T_{VF}[65–68]). Some nonlinear studies support this idea[69] while others give slightly different results[70]. The experiments by Dec et al. show that the scaled 3rd order susceptibility has a broad minimum which was confirmed in several relaxor systems[71–74].

The SRBRF model was extended in order to reproduce the experimental data on nonlinear susceptibility. It was called compressible spherical dipolar glass model[75]. This extension revealed the main flaw of SRBRF model: the assumption that the pseudospins are in the rigid matrix is invalid. It was shown that the electrostrictive coupling plays a crucial role in relaxor ferroelectrics. This addition to the model can reproduce the temperature dependence of third order nonlinear susceptibility. It also shows that the random bonds are as important as random fields.

As it was already mentioned, the relaxors are of displacive type. This analogy is also due to the fact that the canonical lead-based relaxors are closely related to the classical displacive type ferroelectric lead titanate ($PbTiO_3$)[76,77]. Thus, many attempts to identify the soft mode in relaxor ferroelectrics can be found in the literature. The softening of the lowest frequency mode was found at high temperatures in the vicinity of the Burns temperature[31,78–80]. When the temperature is decreased and the temperature of low frequency permittivity maximum is approached, this soft mode becomes heavily overdamped[80–84]. This gives rise to the so called waterfall effect. One of the phonon branches in this temperature region becomes overdamped from certain values of momentum q_{wf}. In the reciprocal space it looks like an optical phonon branch "falls" into the longitudinal acoustical branch with the decrease of momentum q[85]. The heavily overdamped regime of TO optical phonon below q_{wf} persists down to the temperatures which correlate with the freezing temperature T_{VF}. This phonon then becomes again underdamped at the Γ point of Brillouin zone. The heavily overdamped phonon at the Γ point is responsible for the broad dielectric relaxation and is often called a "central peak"[79]. This central peak is responsible for the broad dielectric relaxation which is observed at the microwave frequencies and extends to the THz region. The dielectric relaxation of this central peak often resembles the dispersion in order-disorder type ferroelectrics. It is worth noting that the central peak can also be observed in Brillouin and Raman scattering experiments[86,87]. Recently, several sophisticated Raman experiments actually revealed the softening of polar phonon[88,89] thus supporting the displacive nature of relaxors.

2.5 Lead-free relaxor ferroelectrics

The random fields were thought to be the hallmark of the relaxor properties to appear in perovskite oxides[5,90]. Relaxor properties can occur even in the systems where the charge disorder is absent. A large class of barium based complex perovskite oxides exhibit relaxor-like properties. Usually, it is a systems where barium titanate is mixed with some other incipient ferroelectric like barium zirconate[91,92], barium stannate[93]. The ferro-inactive ions like zirconium or tin possess a 4+ valence in perovskite lattice. The dielectric dispersion in the intermediary compositions (i. e. 50:50 Ti:Zr ratio) resembles relaxor properties. It is sometimes considered that despite the absence of different valence states, the weak random fields still exist in the systems. Some authors relate the relaxor behaviour to the Ti-O dipoles and their displacements[94,95], other refer to the same problem by considering the clustering of ferro-active titanium ions[96,97]**.** Sherrington considers such systems as soft pseudospin glasses[98].

The story behind the lead-based canonical relaxors and lead-free relaxors is significantly different. Nobody has come up with the unified explanation which could take into account peculiarities in the different systems. The mechanisms behind the relaxor behaviour in lead-free relaxors is closer to the one proposed by Samara[99] while for lead-based relaxors this mechanism was neglected (the molecular dynamics simulations revealed that lead displacements play important role for the relaxor properties to develop in PMN-*x*PT system[100]). It seems that Ti-O bonds produce the polar clusters while ferro-inactive ions act as a nonpolar matrix in lead-free relaxors.

One of the important features of some lead-free relaxors is that it is impossible to induce ferroelectric phase with an external electric field which is generic feature of relaxors[101]. Absence of the *E*-field induced phase transitions can be found in some NBT-based systems with strontium titanate[102]. This closely relates these systems to dipolar glasses.

3. Experimental techniques

3.1 Samples

This work is concentrated on three different types of complex perovskite oxides. The first one is **sodium bismuth titanate ($Na_{0.5}Bi_{0.5}TiO_3$)** single crystals/ceramics. This material is one of the most important lead-free perovskite oxides. Most of the improvement of piezoelectric properties was achieved on the NBT-based systems[6,103–106]. The complex structural phase transformations of NBT were extensively studied in the literature[107–110]. The pure sodium bismuth titanate has a very unique phase transition sequence with several tilting modes of the perovskite lattice[111,112].

The main purpose of the investigation is related to its microwave properties in a wide temperature range. The dielectric data on NBT single crystals is not available at the microwave frequencies. For the first time, the dielectric spectra in 10 Hz – 1 GHz frequency range and 300 – 800 K temperature range is presented. The same investigations were carried on the Cr and Mn doped NBT.

The ambiguity of ferroelectric and relaxor state of NBT will be resolved. It will be shown that despite having similar features to canonical relaxors NBT demonstrates completely different picture when viewed from the relaxor-ferroelectric perspective.

The investigated NBT single crystals were grown by Czhochralski method. The crystals were grown by prof. J Suchanicz group who confirmed the single perovskite phase of the crystals by XRD experiments (not presented here but the XRD data is accepted for publishing).

The bulk ceramics of NBT were produced by the conventional mixed-oxide route. The samples were sintered for 3 hours in 1150 °C temperature[113]. The relative density of the ceramics was larger than 93 %.

The second single crystal presented in the thesis is **$0.83PbMg_{1/3}Nb_{2/3}O_3$-$0.17PbTiO_3$ (PMN-17PT)**. The extensive study of dielectric, ferroelectric and piezoelectric properties has not been accomplished so far. PMN-17PT crystals are considered to have an intermediary strength of random fields. This composition is in the rhombohedral side of the phase diagram[114]. This region of the phase diagram has not been thoroughly studied. There are several unanswered questions related to the ferroelectric ordering and structural phase transition in the rhombohedral side of the phase diagram.

PMN-17PT (001) single crystals were grown by the modified Bridgeman technique[115]. These crystals were yellowish and transparent. It indicates the high quality of the single crystals. The crystal was produced by the commercial manufacturer.

The last set of materials consists of **$(0.4\text{-}y)Na_{0.5}Bi_{0.5}TiO_3\text{-}0.6SrTiO_3\text{-}yPbTiO_3$** and **$0.4Na_{0.5}Bi_{0.5}TiO_3\text{-}(0.6\text{-}x)SrTiO_3\text{-}xPbTiO_3$** solid solutions. This is a complex ceramics which consist of relaxor counterpart mixed with a lead titanate (analogous system to PMN-*x*PT). The relaxor part is the $0.4Na_{0.5}Bi_{0.5}TiO_3\text{-}0.6SrTiO_3$. The exchange of one of the counterparts by lead titanate leads to a very complex phase diagram where the crossover from glassy to relaxor and ferroelectric states is observed[116–118].

The thorough studies of dielectric properties and lattice dynamics were carried out for the first time in $(0.4\text{-}y)Na_{0.5}Bi_{0.5}TiO_3\text{-}0.6SrTiO_3\text{-}yPbTiO_3$. Furthermore, the detailed studies of piezoelectric and ferroelectric properties in macroscopic and microscopic scales were carried out. It allowed to identify the complex domain structures and their contribution to the macroscopic piezoelectric effect. Many reports can be found in the literature about the excellent properties of similar ternary solid solutions but the lattice dynamics and different types of contributions to the piezoelectricity were not thoroughly studied. It will be shown that despite different microscopic picture of PMN-xPT and NBT-ST-PT solid solutions, the macroscopic response has genuinely the same features.

$Na_{0.5}Bi_{0.5}TiO_3\text{-}SrTiO_3\text{-}PbTiO_3$ (NBT-ST-PT) ceramic samples with a different NBT:PT (or ST:PT) ratio were prepared by the conventional solid state reaction method. Chemical-grade oxides and carbonates (purity > 99.5%)

Na_2CO_3, Bi_2O_3, $SrCO_3$, PbO and TiO_2 were used as starting materials. The powders were weighed according to the stoichiometric ratio, mixed with ethanol and milled in an agate ball mill for 24 hours at room temperature. In a first round, the dried powder was calcined at 850-900 °C for 2 hours. Afterwards, it was milled again under the same conditions for 24 h and calcined for a second time at 1000 °C for 2 h. After another milling step for 24 h, the powder was pressed uniaxially into a cylinder with a diameter of ~17 mm and a thickness of ~10 mm and then compacted under pressure of 30 MPa using a hydraulic press. The ceramic sample was sintered at 1200 °C for 3 h. The calcination was carried out in a covered platinum crucible. The pressed pellet was sintered in a platinum crucible filled with a powder of the same composition. The structural characterization of the produced ceramics can be found in APPENDIX II. Only one of the compositions is presented but the same trends can be observed in different concentration samples. Further information on the preparation and structural aspects can be found in the literature[116,119].

The summary of the investigated samples are represented in Table 3.1. All the electrodes were painted and fired at a certain temperature with a certain conductive paste.

Table 3.1 Summary of the investigated samples.

Sample	Sample form	Preparation method	Electrode	Firing *T*	Orientation
$Na_{0.5}Bi_{0.5}TiO_3$	Single crystal	Czochralski	Ag	750 K	$(001)_c$
$Na_{0.5}Bi_{0.5}TiO_3$	Ceramics	Solid state reaction	Au		N/A
$Na_{0.5}Bi_{0.5}TiO_3$:Mn	Single crystal	Czochralski	Ag	750 K	$(001)_c$
$Na_{0.5}Bi_{0.5}TiO_3$:Cr	Single crystal	Czochralski	Ag	750 K	$(001)_c$
$0.83PbMg_{1/3}Nb_{2/3}O_3-0.17PbTiO_3$	Single crystal	Modified Bridgeman	Ag	750 K	$(001)_c$
(0.4-*y*)NBT-0.6ST-*y*PT	Ceramics	Solid state reaction	Ag/Au	750 K	N/A
0.4NBT-(0.6-*x*)ST-*x*PT	Ceramics	Solid state reaction	Ag/Au	750 K	N/A

3.2 Broadband Dielectric Spectroscopy

The dielectric spectra were investigated in a broad frequency and temperature range. The temperature was measured with Keithley Integra 2700 multimeter which can be equipped with different temperature sensors. For the low frequency experiments 100 Ω platinum resistor or a diode was used. The T type thermocouple was used as a temperature sensor in the microwave frequency experiments. Most of the data was obtained in 100 – 500 K temperature range.

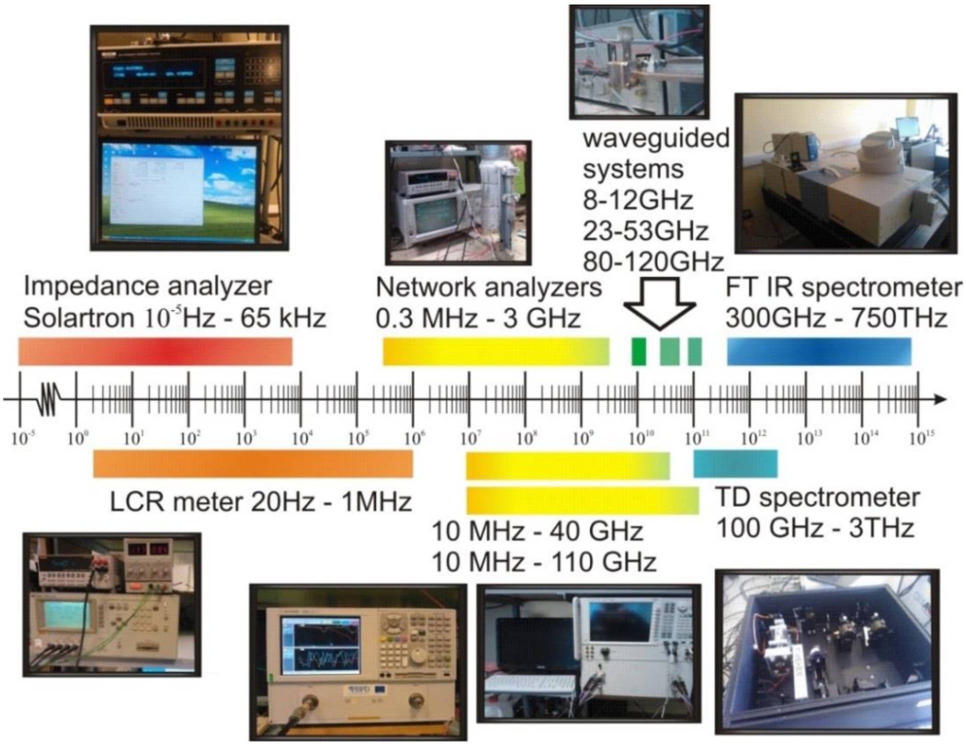

Figure 3.2.1 The schematic representation of dielectric experiments performed in the thesis. The picture is provided by Sergejus Balčiūnas.

The different frequency ranges requires different experimental setups which will be discussed from the lowest frequency range to the highest frequency range. The graphical summary of dielectric experiments is depicted in Figure 3.2.1.

The experiments at low frequencies (5 mHz – 1 MHz) can be performed by measuring the capacitance and loss tangent with a conventional LCR meters. The HP-4824A LCR meter was used for the most of the experiments in this work. The limiting factor for measuring the lowest frequencies (5 mHz – 100 Hz) is the measurement of the current. In order to obtain the data, the SOLARTRON 1296 dielectric interface along with SOLARTRON 1250 frequency response analyzer was used. The dielectric interface allows to measure very low currents which is necessary to measure the capacitance reliably. The simple flat capacitor model was used to extract the permittivity from the capacitance and loss tangent in these experiments.

The capacitance measurement with an LCR meter fails at higher frequencies since the inductance of the experimental setup cannot be neglected. More sophisticated experimental techniques are necessary for the experiments. The measurement of complex reflection/transmission coefficients in the coaxial line is the most convenient method for the 1 MHz – 1 GHz frequency range. The complex reflection and transmission coefficients are related to the impedance of the samples by the following equations:

$$R^* = \frac{Z_2 - Z_0}{Z_2 + Z_0} \tag{3.2.1}$$

$$T^* = \frac{2Z_2}{Z_2 - Z_0} \tag{3.2.2}$$

R^*, T^* denotes the complex reflection and transmission coefficients respectively; Z_2 – the complex load impedance (i. e. the sample); Z_0 represents the characteristic impedance of the transmission line. Z_0 is real and equal to 50 Ω in our case. The load impedance of the sample can be expressed as $Z_2^* = \frac{1}{\mathrm{j}\omega C^*}$. The relation between the complex capacitance C^* and complex dielectric permittivity can be expressed via the flat capacitor model[120].

Two different vector network analyzers were used for the measurements in 1 MHz – 1 GHz frequency (Agilent 8714ET; Agilent E5071C). In the case of complex reflection measurements the sample was placed at the end of short circuited coaxial line. Such kind of experimental setup requires more robust calibration procedure. The calibration procedure is required so the scattering matrix of the experimental setup could be determined. Three calibration loads is necessary to obtain the elements of scattering matrix. The most conventional calibration loads are short circuited coaxial line; open coaxial line and loaded coaxial line (50 Ω load).

The relation between permittivity and capacitance of flat capacitor is only valid for the low permittivity samples. With the increase of permittivity, the distribution of the electric field in the sample becomes inhomogeneous causing the flat capacitor model to fail. This must be taken into account since this work particularly deals with large permittivity samples (sometimes exceeding 10000). The region of coaxial line where the sample is placed must be considered as a circular waveguide. This means that multiple modes with a different distribution of electric field can be excited. This can be taken into account by a so called multi-mode capacitor model developed by Lapinskas et al.[121]. This model extends the reliably measured frequency range and usually eliminates the artificial resonant dispersion due to the excitation of several waveguide modes.

The complex transmittance experiments were carried for the single crystals of sodium bismuth titanate with an Agilent N5071C in a custom-made coaxial line which was developed by Kežionis et al.[122]. High temperature region of the reflection experiments is limited to 500 K. The transmission configuration extends the temperature range up to 1000 K which is necessary for the measurements of NBT single crystals. The whole physics and calibration procedures are based on similar philosophy as previously described. The details of the experimental setup is described in the literature[122].

The coaxial line technique fails above 1 GHz frequency range if the permittivity of samples is large. It faces some difficulties due to the non-ideal calibration loads. Particularly, the short-circuit load has a finite resistance due to the skin effect.

The 8 – 100 GHz frequency region can be covered by the waveguided systems. It is possible to measure scalar reflection and transmission coefficients. In the waveguided systems we deal with a waves and the voltage and current does not have a significant meaning since the wave travels in the space which is confined by the metal walls. The waveguides can support different kind of waves which are described by their electric and magnetic field distribution in the propagating media.

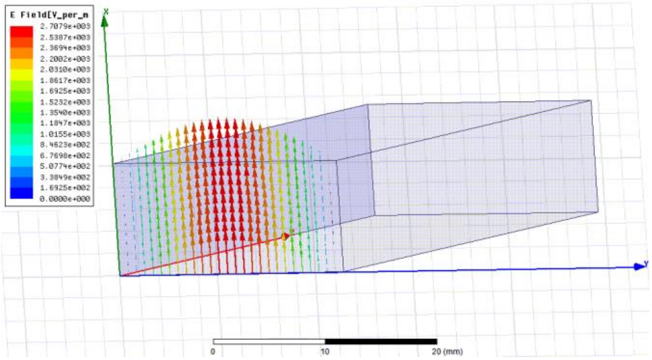

Figure 3.2.2 The electric field distribution of H_{10} mode.

The main requirement for the waveguided system is that only the fundamental mode could propagate. This can only be achieved in a limited frequency range and is only dependent on the cross-section of the waveguide. Thus, several waveguide systems must be used in order to cover wider frequency range. In this work, three different systems were used: 8 – 12 GHz; 25 – 40 GHz; 36 – 55 GHz. The place of the sample is important during the experiments. The advantage of the fundamental mode (Figure 3.2.2) is that it has a single maximum along the longer wall of the waveguide (*E*-field vector is perpendicular to this wall). That place of the waveguide is ideal for the sample to be placed. The electric field has a maximum value while the magnetic field has a minimum value. Thus, the magnetic permittivity does not influence the data and can be neglected. The geometrical restrictions for each of the waveguided systems imply the requirements for the sample geometry. The lowest frequency waveguided system has quite large physical dimensions. Since the sample is placed parallel to the shorter wall of the waveguide, this implies geometry of the samples. It is not possible to get the sufficient amount of the material in order to perform an investigation in 8-12 GHz frequency range. On the other hand, one has to note that for the higher frequencies it is necessary to prepare the samples with much smaller cross-section area. This is often a challenge for the high permittivity samples.

The electrodynamics of cylindrical sample in the waveguide was used for most of the experiments. The detailed description of the Maxwell Equation solutions is provided by J. Grigas[120].

Some experiments required different model. The electrodynamics for the parallelepiped sample in the waveguide is straightforward. The sample is treated as the dielectric inhomogeneity in the waveguide. Thus, there are three separate regions in the waveguide where boundary conditions need to be taken into account. The two regions can be considered as a conventional waveguide and the solutions can be obtained from the wave equations of a z component of the magnetic field (it is the most convenient component for the H_{10} mode). The region where the sample is placed also should be considered and the solution of the wave equations is not trivial. Since the samples usually have a large permittivity, the region where the sample is placed cannot be treated as a region where only the fundamental wave is propagating. Several modes depending on the boundary conditions can appear in this region. The field can be expressed as the superposition of multiple modes. The whole three regions must satisfy the boundary conditions and after applying the mode-matching procedure the solution for the scalar reflection and transmission coefficients can be obtained. The detailed mathematical model is not provided here due to the robustness but it can be found in the literature[120].

The scalar reflection and transmission coefficients are measured by custom-made Elmika R2400 scalar network analyzers. The power of incident, reflected and transmitted waves is detected by the semiconductor low noise diodes for microwave applications. The end of the waveguide is terminated with a load which absorbs the transmitted wave (waveguide is considered to be semi-infinite).

The dielectric permittivity can only be obtained by solving the nonlinear equation $[|R|, |T|] = f(\varepsilon', \varepsilon'')$. This can only be done by solving optimization problem. This is performed by a custom-made solver based on the modified Newton optimization method.

The terahertz spectroscopy was used for the investigation of materials in 100 GHz – 1 THz frequency range. This is a different technique compared to the previously described ones. It is a time-domain technique. The short picosecond pulse is transmitted through the dielectric slab. The response of the sample is Fourier-Transformed in order to obtain the complex transmission coefficient. The transmission coefficient is related to the complex refraction coefficient (which is related to complex dielectric permittivity) according to the following equation[123]:

$$T(\omega) = \frac{4N\exp(\frac{\mathrm{i}\omega(N-1)d}{c})}{(N+1)^2}\sum_{k=0}^{m}\left[\frac{N-1}{N+1}\exp\left(\frac{\mathrm{i}\omega Nd}{c}\right)\right]^{2k} \tag{3.2.3}$$

where N – complex refraction coefficient; d – thickness of the sample; c – speed of light; ω – angular frequency; m – number of reflections in the sample. The detailed description of the experimental setup which was used is provided by P. Kuzel and J. Petzelt[123].

The thin slab of high-permittivity sample is necessary for the experiments. THz spectroscopy is a powerful tool for the investigation of microwave dielectric relaxation. It bridges the low-frequency data with a phonon contribution to the dielectric permittivity.

The combination of all the above mentioned experimental techniques provides most of the information about the dipolar relaxation and dynamics of ferroelectrics and related materials. The ability to access such a broad frequency range is required for the investigation of relaxor ferroelectrics.

The analysis of dielectric spectra requires some relaxation models. One of the most renowned models is the Debye model which can be derived analytically. This model considers that the material consists of dipolar relaxators which do not interact with each other and is described by the Debye-relaxation formula:

$$\varepsilon^*(\omega) = \varepsilon(\infty) + \frac{\varepsilon(0)-\varepsilon(\infty)}{1+\mathrm{i}\omega\tau} \tag{3.2.4}$$

$\varepsilon^*(\omega)$ is the complex dielectric permittivity; $\varepsilon(\infty)$ is the contribution of higher frequency processes (phonons, electrons); τ is relaxation time; ω is the angular frequency. $\varepsilon(0) - \varepsilon(\infty)$ is often denoted as $\Delta\varepsilon$ and is called the dielectric strength of relaxation (this is the quantity which describes the contribution of relaxation process to the dielectric permittivity).

The Debye relaxation describes systems where the relaxation consists of a single relaxation time τ. In other words, distribution of relaxation times of such system has a form of Dirac delta function.

Usually, the dielectric relaxation is much broader than the ones which can be described by the Debye model. Some empirical corrections must be made to the Debye formula to describe broader relaxations. The most general case is called Havriliak-Negami equation[124]:

$$\varepsilon^*(\omega) = \varepsilon(\infty) + \frac{\varepsilon(0)-\varepsilon(\infty)}{(1+(\mathrm{i}\omega\tau_{HN})^{1-\alpha})^{\beta}} \tag{3.2.5}$$

Two additional parameters are introduced in the Havriliak-Negami equation. Parameter α represents the breadth of distribution of relaxation time and is directly related to the peak width of imaginary part of dielectric permittivity. The parameter β represents the asymmetry of the dielectric spectrum. Since the distribution of relaxation times of this equation has a finite width, the parameter τ_{HN} is called the Havriliak-Negami relaxation time. The physical meaning of this parameter is ambiguous. Usually, the mean relaxation time is analysed instead. Sometimes the edge of distribution is also considered. The general aspects of Havriliak-Negami equation,its logarithmic moments and their relation to τ_{HN} can be found in an excellent review papers by Zorn[125,126]. In this work only the mean relaxation time is considered.

In the most general case, the dielectric spectra can be described by the superposition of the Debye relaxations. It can be expressed by the following equation[127]:

$$\varepsilon^*(\omega) = \varepsilon(\infty) + \Delta\varepsilon \int_{-\infty}^{+\infty} \frac{f(\ln\tau)\,\mathrm{d}\ln\tau}{1+\mathrm{i}\omega\tau} \tag{3.2.6}$$

Where $f(\ln\tau)$ represents the distribution of relaxation time. Eq. 3.2.6 can describe any complex dielectric spectra if the distribution of relaxation time is known. Usually, the inverse problem is solved for determining the distribution from the frequency dependences of permittivity[51,127].

The fitting procedure was carried out by the superposition of several Havriliak-Negami equations. Each particular case will be presented and justified where it is relevant.

3.3 Vibrational Spectroscopy

A branch of experimental techniques which deal with the lattice and/or molecular vibrations is called vibrational spectroscopy. The probe which interacts with the lattice vibrations is necessary for these experiments. The lattice vibrations in the solid state physics is characterized by the quasi-particles called phonons. It is generally a chain of atoms which are bonded by electrostatic interactions. This excitation is considered to be localized in the material.

There are two types of phonons in the matter: acoustic and optical phonons. The acoustic phonon is a coherent vibration of the atomic chain. The optical phonon is the anti-phase vibration of the atomic chain (i. e. ions which have opposite charge move in a different direction from their equilibrium position). The characteristic frequencies of optical phonons lies in a far infrared region (hence, the name optical phonon). There can be two different types of phonons depending on the propagation direction vs. the displacement of the atoms. The phonon is called longitudinal if the displacement of the atoms coincides with the direction of propagation and transverse when it is perpendicular to the propagation.

Phonons in the matter can interact with electromagnetic waves. The interaction between electromagnetic waves and phonons occur at the Γ-point of the Brillouin zone. This means that the interaction occurs between the long-wavelength phonons (relative to the lattice constants). There are three main techniques which are capable of probing the phonons at the Brillouin zone center. The optical phonons can be probed by Raman and Fourier-transform infrared spectroscopies while acoustic phonons can be investigated by the Brillouin scattering technique (please note that Raman and Brillouin scattering can be achieved in a very similar experimental setup). In this work only Raman and FTIR spectroscopic studies were carried out.

The polar phonons can be investigated by the FTIR experiments. Phonon is called polar when dipole moment of the atomic chain changes during the vibration. This experiment is closely related to the broadband dielectric spectroscopy since it probes polar vibrations and is closely related to the dielectric function of the material.

The main component of the FTIR spectrometer is Michelson interferometer (Figure 3.3.1). The FIR source is usually the mercury lamp. The beamsplitter splits the signal. One part of the signal goes to the fixed mirror and the other one to the moving mirror. In this case the autocorrelation function is obtained in the detector (interferogram). The power spectrum is obtained after the Fourier transform of the interferogram. The experiment can be carried out in a transmission and reflection mode. In the case of transmission mode the sample is placed between the beamsplitter and detector. The calibration is necessary to determine the response function of the spectrometer**.** The empty sample holder serves as a calibration kit in transmission geometry. The transmittance of the sample can be determined as follows:

$$|T| = \frac{P_S(\omega)}{P_0(\omega)} \tag{3.3.1}$$

where $|T|$ represents the transmittance spectrum; P_s – power spectrum of the sample; P_0 – the power spectrum transmitted through the empty sample holder. Unfortunately, the transmission geometry is usually not suitable for the high permittivity samples. The signal can hardly transmit the sample in the FIR region and it is difficult to prepare sufficiently thin samples for the experiments.

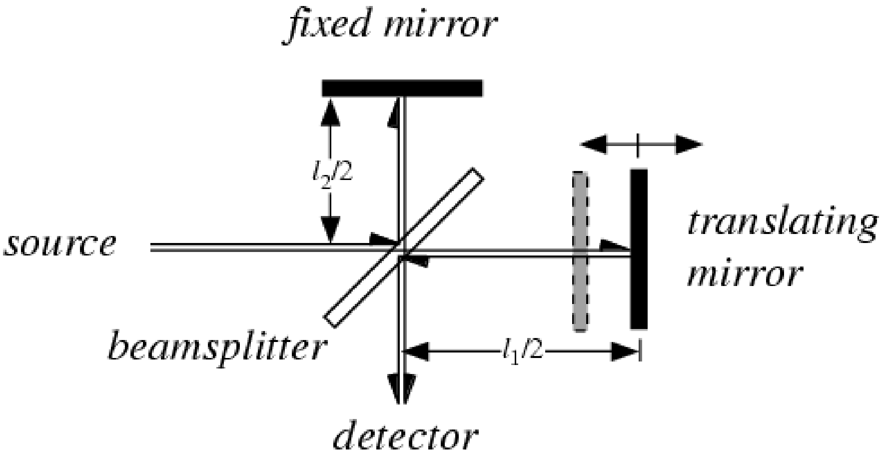

Figure 3.3.1 The scheme of Michelson interferometer. The image source: http://scienceworld.wolfram.com/physics/FourierTransformSpectrometer.html

The investigation of high permittivity solid samples is much more often conducted in the reflection geometry. This can be achieved by placing the sample in the position of the fixed mirror. The calibration is performed by placing a highly-reflective mirror (as it is shown it the Figure 3.3.1). The reflectance spectrum is obtained by using the same equation as for the transmittance spectrum (Eq. 3.3.1). The P_0 represents the power spectrum from the highly reflective mirror and P_s is the power spectrum of the sample.

The relation between the dielectric permittivity and reflectance spectrum is as follows:

$$|R| = \frac{|\sqrt{\varepsilon^*}-1|^2}{|\sqrt{\varepsilon^*}+1|^2} \tag{3.3.2}$$

ε^* denotes the complex dielectric permittivity.

The equation 3.3.2 hints that the determination of complex dielectric permittivity from the reflectance spectrum is not ambiguous. First of all, one needs to solve the nonlinear equation to determine the permittivity. Secondly, there are two unknown quantities (real and imaginary part of dielectric permittivity).

The dielectric function can be modelled by the sum of simple oscillators (3-parameter oscillator model)[128]:

$$\varepsilon(\omega) = \varepsilon_\infty + \sum_k \frac{S_k}{\omega_{kTO}^2 - \omega^2 + \mathrm{i}\omega\gamma_{kTO}} \tag{3.3.3}$$

The term ε_∞ denotes the higher frequency contributions (i. e. electronic contribution), S_k – oscillator strength; ω_{kTO} and γ_{kTO}– frequency and damping of k-th transverse optical phonon.

This model takes into account only transverse modes. It does not allow the tuning of LO frequency and thus the line width of the phonon bands cannot be adjusted. This model works quite well for the materials where the bands are quite narrow and the damping is low. The difficulties arise to describe the spectra of perovskite oxides where the damping and spectral bands are quite broad. This problem can be solved by introducing the so called four parameter oscillator model[129]:

$$\varepsilon(\omega) = \varepsilon_\infty \prod_j \frac{\omega_{jLO}^2 - \omega^2 + \mathrm{i}\gamma_{jLO}\omega}{\omega_{jTO}^2 - \omega^2 + \mathrm{i}\gamma_{jTO}\omega} \qquad (3.3.4)$$

Here, numerator and denominator have only LO and TO parameters respectively. It is obvious that this function is much more robust.

The FTIR spectra were measured with the Bruker Vertex v80 spectrometer in 30 – 3000 cm^{-1}. The spectra were recorded in 100 – 500 K temperature range. The temperature was monitored and controlled by SPECAC WEST 6100+ controller. The T type thermocouple was used as a sensor. The special unit by Bruker was used for the reflection experiments.

Raman spectroscopic experiments are based on the inelastic light scattering. The incident light (laser beam) interacts with an optical phonons. The scattered light has a different frequency than the incident beam. This happens due to the fact that the particle is excited to the virtual states. The relaxation to the ground state is followed by the interaction with optical phonons. If the backscattered photon has a lower energy than the incident beam it is called the Stokes shift; if the energy is larger – the anti-Stokes shift. The intensity of the Stokes shift is much larger since the transition takes place from the ground state which is highly populated (the anti-Stokes shift is due to the jumps from the excited vibrational levels which according to the Boltzmann statistics is less populated).

Raman Spectroscopy can identify different kinds of phonons and supplement the FTIR experiments. The Raman active modes are the ones which has a change of polarizability during the vibration. The Raman signal is proportional to the imaginary part of dielectric susceptibility at a given frequency. This relation arises from the fluctuation-dissipation theorem[130].

The analysis of Raman spectra is less robust than the IR spectrum. The vibrational frequencies are directly related to the peaks in the Raman spectra. Since the Raman spectrum very often consists of multi-peaks, it is relevant to fit it with the superposition of Gaussian-type functions:

$$I(f) = I_0 + \sum_k \frac{2I_k}{\pi} \frac{\Delta f_k}{4(f-f_k)^2 + \Delta {f_k}^2} \qquad (3.3.5)$$

The expression 3.3.5 has the same form as an imaginary part of 3-parameter oscillator model (Eq. 3.3.3). The quantities in Eq. 3.3.5 have the meaning as follows: I_k– intensity of k-th Raman mode; f_k– mode frequency (maximum of the peak); Δf_k – width of the peak (it is proportional to the damping). Please note that all the Raman spectra in this work were normalized by the Bose-Einstein factor.

The experiments were carried by the Renishaw RM1000 micro-Raman spectrometer. It is equipped with an Ar laser operating at 514 nm. It works in a backscattering geometry. The signal was detected by the CCD camera. The experiments were carried out in 80 – 600 K temperature range.

3.4 Ferroelectric/Piezoelectric/Pyroelectric Characterization

The ferroelectric, piezoelectric and pyroelectric characterization of the samples was performed by commercial AixACCT TF2000 analyzer. The device is equipped with a TREK 609E-6 high voltage supply which works in a DC regime up to 4 kV. The device also has a single beam interferometer for the piezoelectric characterization. The sample holder can operate in 200 – 800 K temperature range.

The measurements of the ferroelectric hysteresis can be performed by applying the triangular voltage and measuring the current. The frequency of the triangular wave in the experiments was 10 Hz or less. It can be considered as a quasi-static regime.

The polarization can be calculated from the current response. The integration of the current over time gives an accumulated charge:

$$Q = \int_0^{t_f} I_{meas} \mathrm{d}t \tag{3.4.1}$$

Where, Q is accumulated charge, I_{meas} experimentally measured current; t_f is the duration of the triangular pulse. The integration of the experimental data is performed digitally. Thus, this method is different from the conventional Sowyer-Tower method where the capacitor performs the integration. The polarization can be calculated by simply dividing the accumulated charge by the surface area S of the sample:

$$P = \frac{Q}{S}. \tag{3.4.2}$$

Simultaneously to the measurements of the polarization hysteresis, the displacement hysteresis was measured. The single beam laser interferometer is focused on the top of the electrode which has a spring. The spring deforms when the sample undergoes the deformation due to an electric field. The detector performs the quadrature modulation. This method is capable of measuring the displacements as low as 30 nm (according to the manufacturer the accuracy should be around 10 nm).

The quasi-static piezoelectric and/or electrostrictive coefficients can be determined from the experimental data. If the displacement is caused by the piezoelectric effect, small signal d_{33} can be resolved by the fitting of an experimental data for small electric field amplitudes. The relation between the strain and electric field can be expressed accordingly:

$$s_{33} = d_{33} E_3 \tag{3.4.3}$$

The strain due to electrostriction is proportional to the square of the polarization:

$$s_{ij} = Q_{ijkl} P_k P_l \tag{3.4.4}$$

In the cases which will be dealt in this work (strain along the polarization direction) the Eq. (3.4.4) simplifies to:

$$s = Q_{11}P^2 \tag{3.4.5}$$

The determination of the electrostriction coefficient is evident from the Eq. (3.4.5): It is necessary to plot the strain vs. the square of the polarization and perform the linear fitting procedure.

The pyroelectric current I_{pym} was measured on the heating cycle after the sample was poled. The temperature rate was 10 K/min. The temperature dependence of polarization can be obtained from the pyroelectric coefficient $\gamma(T)$:

$$P = \int_{T_0}^{T_f} \gamma(T)\mathrm{d}T \tag{3.4.6}$$

The temperature dependence of pyroelectric coefficient can be directly determined from the experimental data:

$$I_{pym}(T) = \gamma(T)S\frac{\mathrm{d}T}{\mathrm{d}t} \tag{3.4.7}$$

Where $\frac{\mathrm{d}T}{\mathrm{d}t}$ is the temperature change rate.

3.5 Piezoresponse Force Microscopy

The scanning probe microscopy (SPM) is a set of experimental techniques which probe the nanoscale properties of the materials. The nano-sized probe excites particular response of the material and this response is registered. The godfathers of the SPM experiments are atomic force microscope (AFM) and scanning tunneling microscope (STM). AFM probes the topography of the surface due to the atomic interactions between the tip and the surface of the sample. The STM is suitable only for the conductive samples since it is based on the tunneling effect. The STM signal is registered when the tip of the microscope comes close enough to the surface so the tunneling current starts flowing between the sample and the probe.

The SPM experiments can be performed by a contact mode (the tip touches the sample) and non-contact mode (the constant distance between the sample and the end of the tip is preserved). These experiments allow the scanning of the nanoscale phenomena. The lateral resolution of STM and AFM is less than 1 nm[131,132]. It is also necessary to note that it is a strictly surface probe since the in-depth resolution is lower than the lateral resolution.

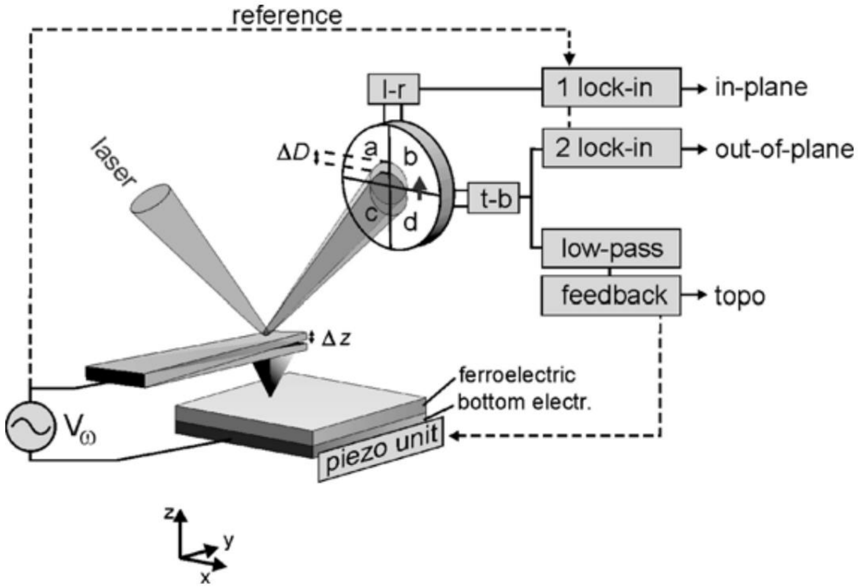

Figure 3.5.1 The representation of piezoresponse force microscope. Reprinted from Kholkin et al.[133] with a permission of Springer Science Business Media, LLC.

The piezoresponse force microscopy (PFM) is a contact SPM method. The interaction between the tip and the sample is due to the piezoelectric effect. The AC voltage is applied between the sample and the tip. The displacement of the tip can be affected by the local polarization of the sample under test. This probes the local piezoelectric response both in-plane and out of plane. The schematic representation of piezoresposne force microscope is depicted in Figure 3.5.1. The deflection of the tip is monitored by the laser beam which is focused on the 4 quadrant detector. This type of the detector is capable of capturing topography, lateral and vertical PFM signals simultaneously. The demodulation of the signals is performed by several lock-in amplifiers which are one of the most important parts of the microscope. The feedback loop is necessary to control the force on the tip.

The total PFM signal consists of several contributions. The electromechanical contribution enables to determine the domain structure (the piezoelectric response is sensitive to the direction of polarization). It is a proper tool to probe the (nano)domain structures in the complex perovskite oxides.

The possibility of applying DC bias between the tip and the ground electrode gives ability to study the ferroelectric switching and sometimes even domain kinetics in ferroelectrics. It is possible to change the domain structure and observe how it relaxes and interacts with the defects. It is very important in the investigation of polycrystalline ceramics and films.

Another thing which can be observed in these experiments is the local polarization hysteresis loops. This is quite a robust experiment which is difficult to describe quantitatively but it might give crucial information about the switching processes at the different locations of ceramic samples. This is relevant for the work which will be presented here.

The PFM studies were performed using a MFP 3D microscope (Asylum Research). Domain visualization was done both in a single frequency and DART mode using an AC voltage with amplitude U_{ac} = 5 V. Both vertical and lateral PFM images were collected. The local piezoresponse hysteresis loops were acquired in the switching spectroscopy mode. In this mode the PFM tip is placed on a selected location and a sequence of dc voltage pulses with duration of 50 ms and magnitude cyclically changed from -50 to 50 V were applied between the tip and the sample. The induced piezoresponse was measured between the pulses (in the off-voltage state) using the DART mode. PFM measurements were performed at room temperature and on heating up to 450 K. Cantilevers ElectriMulti 75-G (Budget Sensors) with conductive Cr/Pt coating, a tip apex radius of 25 nm, and a resonant frequency of f_0 = 75 kHz were used. For analysis of the PFM data WSxM[134] and Gwyddion[135] software were used.

4. Experimental results

4.1 Dielectric Spectroscopy of $Na_{0.5}Bi_{0.5}TiO_3$ (NBT)

Sodium bismuth titanate is one of the unique perovskite oxides with the A-site chemical disorder. This material can exist in a crystalline form and thus attracted many attention due to its very peculiar structural[107,136,137], ferroelectric and piezoelectric[108,138] properties.

One of the most important counterpart of NBT is bismuth which has a very similar electronic structure to lead. The lone pair of bismuth should also promote the covalent bonding between electronic states of A-O ions. Indeed, it was revealed that there are evidence of the covalency due to this lone pair of bismuth[139]. They concluded that the anomalies of physical properties of NBT can solely be attributed to the lone-pair effects[139]. The Raman experiments on which these conclusions were made are only indirect evidence. This shows that the bonding character changes but the exact mechanism is not obvious.

Sodium bismuth titanate has a quite complex octahedral tilting. The octahedral tilting plays an important role and the instabilities of the tilts are related to the some of peculiar structural transformations[111,112,140]. The surprising fact is that the transition temperatures which are obtained by the convenient structural analysis techniques do not correspond to the anomalies observed in the macroscopic response (dielectric permittivity[137,141], polarization measurements etc.). The ferroelectric hysteresis can be observed up to certain temperature which is very often denoted as the depolarization temperature T_d. This temperature shows that the ferroelectric order disappears spontaneously after heating the sample above the T_d. There are no structural changes in the vicinity of the depolarization temperature. This peculiar behaviour has drawn many attention to this system. Especially, when it was revealed that the mixed systems based on the sodium bismuth titanate are promising materials for the electromechanical applications. It was found by Vakhrushev et al. that NBT is more of displacive-type material[108] but the low frequency dielectric data points to some relaxor-like features. The dielectric experiments in a broad frequency and temperature range (which has never been achieved for the single crystals) are exploited to resolve this ambiguity.

4.1.1 Single crystals of NBT

The temperature dependences of complex dielectric permittivity of sodium bismuth titanate (001) single crystal are depicted in Figure 4.1.1. The data is presented for both heating and cooling regimes. There is no dispersion up to 1 GHz frequency in 650 – 900 K temperature interval. This region indicates the paraelectric phase and it follows the Curie-Weiss law. The Curie-Weiss law behaviour in NBT solid solutions was previously reported by Isupov[142]. The heating and cooling cycle curves coincide in this temperature region. The discrepancy can be observed only on heating cycle where weak dispersion is observed at low frequencies (i e. $f \leq 10$ kHz). This dispersion disappears on cooling cycle. This relaxation is not an intrinsic property of the crystal. It is related to the interfacial relaxation between electrode and the crystal (i e. Maxwell-Wagner polarization).

The imaginary part of complex dielectric permittivity shows some differences on heating and cooling cycles. It can be attributed to the above-mentioned Maxwell-Wagner relaxation and/or conductivity. Nevertheless, clear hysteretic behaviour can even be observed at 100 MHz curve. It is possible to associate this hysteresis to the 1st order ferroelastic phase transition which occurs at around 800 K[109,143]. Ferroelastic phase transitions are difficult to detect by means of dielectric spectroscopy. There are no anomalies in real part of permittivity in the vicinity of the ferroelastic phase transition. It rather can be observed only in the imaginary part. It is worth noting that this ferroelastic phase transition occurs due to the tilting of oxygen octahedra[142].

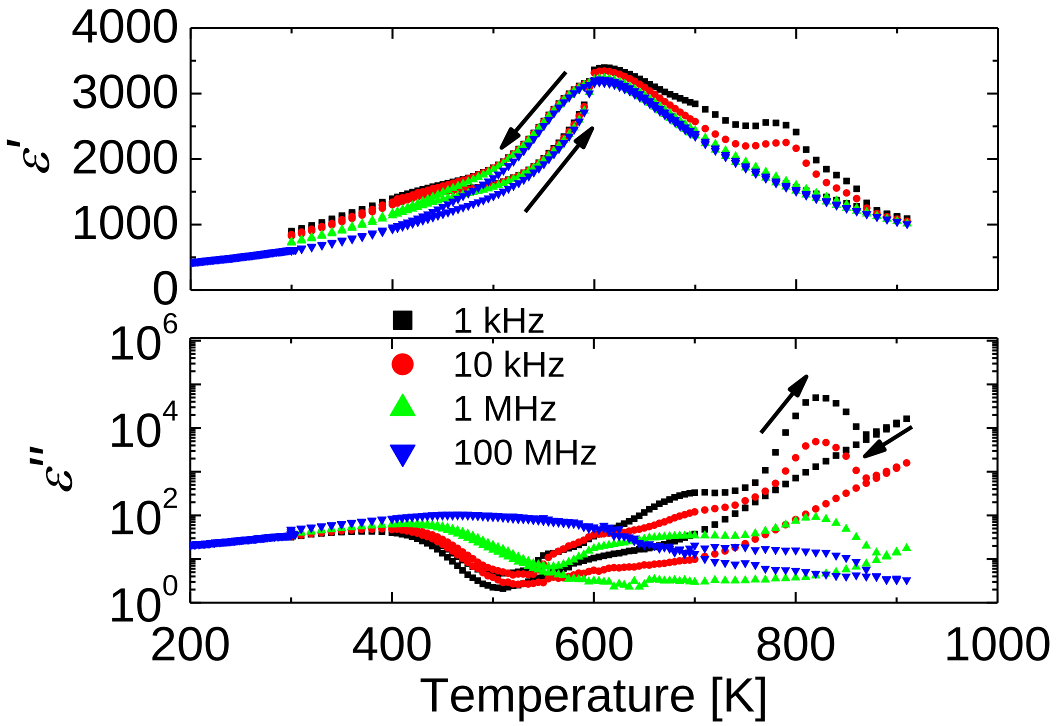

Figure 4.1.1 Temperature dependence of complex dielectric permittivity of NBT single crystal at different frequencies. The data is depicted on heating and cooling cycles.

The thermal hysteresis below the permittivity peak $T_m \approx 600$ K can be clearly evidenced in Figure 4.1.1. This thermal hysteresis is related to a phase transition from rhombohedral to tetragonal phase[111,140]. The phase transition is antipolar and is related to the different tilting configurations of oxygen octahedra. The hysteretic behaviour is due to the fact that this phase transition occurs in a rather broad temperature range. The hysteresis is quite broad which is not usual to classical phase transitions. Such broad thermal hysteresis can be observed during the incommensurate phase transitions. There were several reports on the incommensurate/modulated phase in sodium bismuth titanate[111,112,144].

Another peculiarity of the thermal hysteresis is that the shape of the curve on heating and cooling differs in the vicinity of the T_m. The heating cycle resembles a proper ferroelectric phase transition with quite abrupt increase in the permittivity. A completely different picture is observed on cooling cycle. The same peak looks much broader. The cooling curve resembles the properties of canonical relaxor. These experiments in a rather broad frequency range revealed one significant difference from the canonical relaxors. It seems that there is no dispersion at least up to 1 GHz frequency. This is a significant distinction between canonical relaxors and sodium bismuth titanate where dispersion onsets at frequencies lower than 1 MHz[46]. So the dispersion (if it is present) is different from canonical relaxors and rather resembles the central peak in such classical ferroelectrics as barium titanate. This central peak is often attributed to the coexistence of order-disorder and displacive type dynamics[24,145,146].

Another significant temperature region is 300 – 500 K. This is the region where dielectric data become independent of heating and cooling cycles. It also has a dispersion which often is regarded as a signature of relaxor ferroelectric properties of NBT. The current experiments reveal that the dispersion lies only below 1 MHz. It is a clear distinction from relaxor ferroelectrics where dispersion expands more than 10 orders of magnitude in frequency. One significant similarity to relaxor ferroelectrics can be observed in the imaginary part of permittivity. The fashion how imaginary part develops at different frequencies versus temperature is a signature of relaxor behaviour. The lowest temperature data show constant loss regime which is often observed in canonical relaxors. It is necessary to keep in mind that the rhombohedral phase below 500 K is ferroelectric in NBT. Thus, the relaxation should be associated with the domain wall motion rather than polar nanoregions (or microscopic inhomogeneities). Indeed, according to Strukov and Levanyuk[17] the domain wall dispersion lies in the frequency region below 1 MHz. It is clearly seen from the data above 1 MHz that no additional kink in the temperature dependences of the permittivity can be observed (for the obvious illustration, please refer to Figure 4.1.5).

The evolution of the 300 – 500 K relaxation is much more evident from the frequency dependences of complex dielectric permittivity (Figure 4.1.2). The spectra below 450 K show nearly linear decrease in permittivity in semi-logarithmic scale while in imaginary part the constant loss regime is observed in the whole investigated frequency range. Such broad dielectric relaxations are often found in disordered ferroics. The significant change in dielectric spectrum is observed at 450 K. The drastic decrease of imaginary part is observed relative to the values below 450 K temperature. This change correlated to the depolarization temperature of NBT[138]. This means that the domains which contribute to permittivity disappear in this temperature and thus such gradual drop in the imaginary part of dielectric permittivity. This domain wall-like relaxation becomes much narrower and it is possible to observe the significant microwave relaxation where the maximum of imaginary part is expected to be around 10 GHz. It is necessary to stress that the higher temperature data above 300 MHz is not reliable due to the limitations of the experimental technique. This causes a sudden drop in permittivity which is observed in the vicinity of 1 GHz at temperatures above 450 K. Unfortunately, due to the breadth of the relaxation it is difficult to describe it quantitatively.

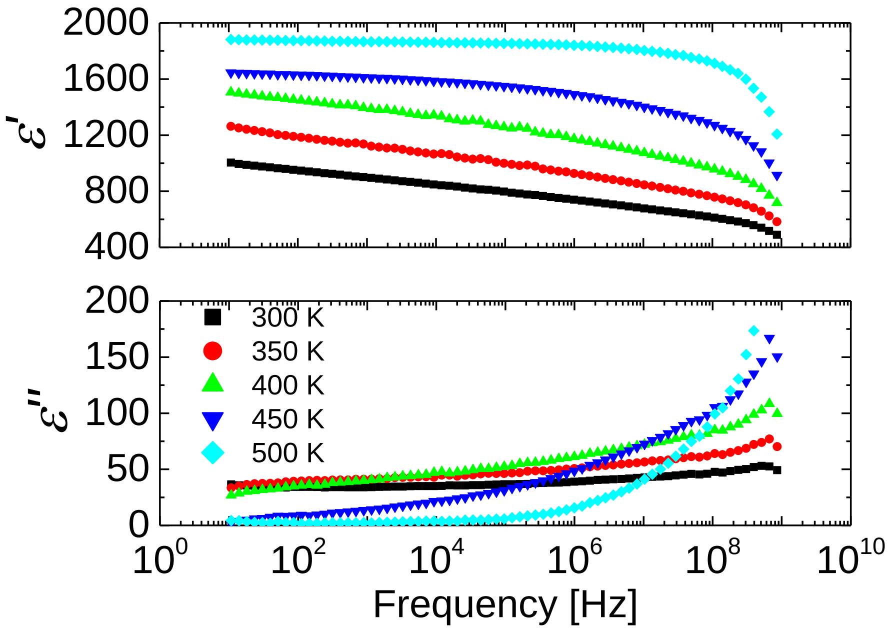

Figure 4.1.2 Frequency dependences of NBT single crystal at different temperatures. The data is depicted only in the temperature region where the low frequency relaxation is observed.

4.1.2 Single crystals of Mn and Cr doped NBT

Very often in order for perovskite oxides to meet specific requirements for the applications it is necessary to modify the electromechanical properties by slightly doping. In the field of electromechanical applications it is known as “hardening” or “softening” of a piezoelectric material[147]. The ‘hardening’ in this sense means that that dopants increase the coercive field, decrease the piezoelectric coefficients of the material and makes it sustainable for the high energy applications. The ‘softening’ of the material on the other hand decreases the coercive field and makes the material much more sensitive to external stimuli. The doping with donor impurities in A or B-site of perovskite lattice leads to the softening while acceptor dopants lead to the hardening. This is usually explained by the change in domain wall mobility. The acceptor dopants pin domain walls while donors increase their mobility[148].

Manganese ions are often used in lead-based materials as a hardening dopant[149–151]. In some cases, the effect of Mn doping was reported to have much more complicated impact on the piezoelectric properties[152]. The EPR studies by Kamiya et al. showed that the mixed valence states (i. e. 3+ and 2+) of Mn can exist in PZT[152]. It is also possible that Mn can have 4+ state in some cases as well (this is allowed by the Goldstone tolerance factor[153]). This means that it is possible for manganese to occupy A-site and B-site (especially in the case of sodium bismuth titanate). So in general Mn cannot be considered strictly as ‘softening’ or ‘hardening’ dopant. The Mn occupancy in perovskite lattice as a dopant is often complicated topic and is still a subject of debate how it is incorporated in the perovskite lattice.

Chromium ions in perovskites most commonly have valence of 3+ and act as an acceptor occupying the B-site of the perovskite lattice. It is possible to obtain the valence 4+ in the perovskite oxide but it is necessary to produce the material under high pressure. One of the examples of such route was demonstrated in $PbCrO_3$[154] and its solid solutions with other lead-based oxides[155]. The reports on more conventional production methods of Cr-doped perovskites deal with the 3+ valence.

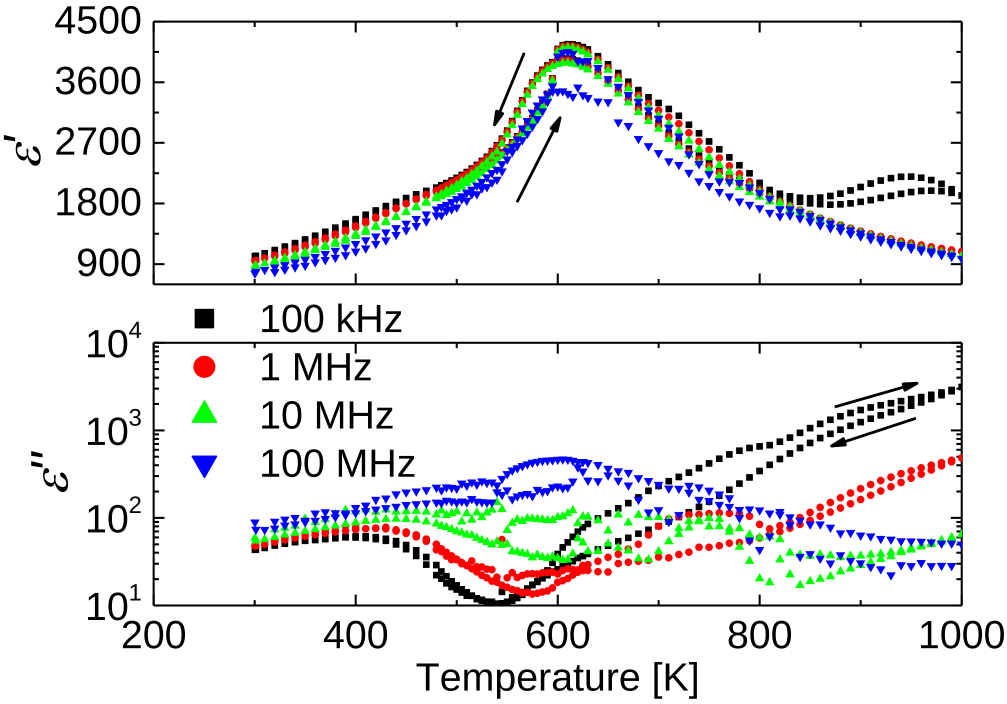

Figure 4.1.3 Temperature dependences of complex dielectric permittivit of NBT:Mn single crystal at different frequencies.

Figure 4.1.3 and Figure 4.1.4 represent the temperature dependences of sodium bismuth titanate doped with 0.05 % manganese and 0.05 % chromium ions respectively. Both crystals display the same temperature evolution as the pure NBT single crystal. All the characteristic temperature regions have similar features. Only minor differences in the maximum temperature around 600 K (Mn and Cr doped samples have maximum slightly shifted to the lower temperatures). Another difference can be observed in the paraelectric phase. A significantly larger dielectric loss can be observed at the lower frequencies indicating the increase of conductivity in the doped samples. The impact of both dopants to the dielectric properties of NBT is similar. The permittivity and loss is larger in both doped crystals (see Figure 4.1.5). The increase of real and imaginary parts of permittivity indicates that the dielectric properties are modified via contribution to the conductivity. This means that the vacancies occurring due to the charge incompatibility in the lattice are not compensated. They created additional dipoles which contribute to the dielectric permittivity.

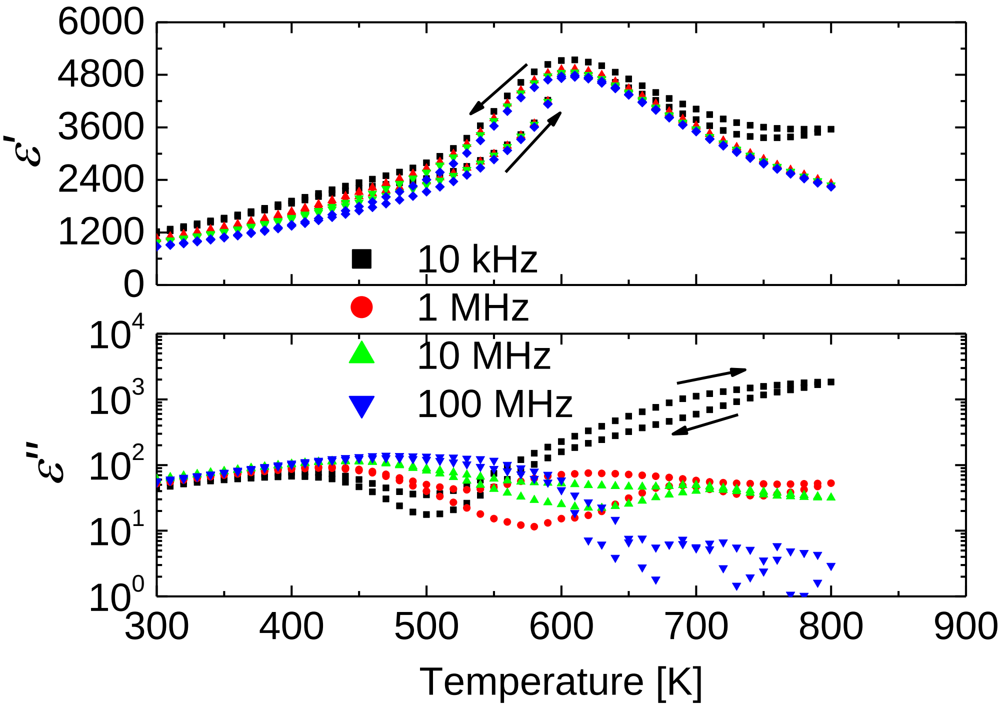

Figure 4.1.4 Temperature dependences of complex dielectric permittivity of NBT:Cr single crystal.

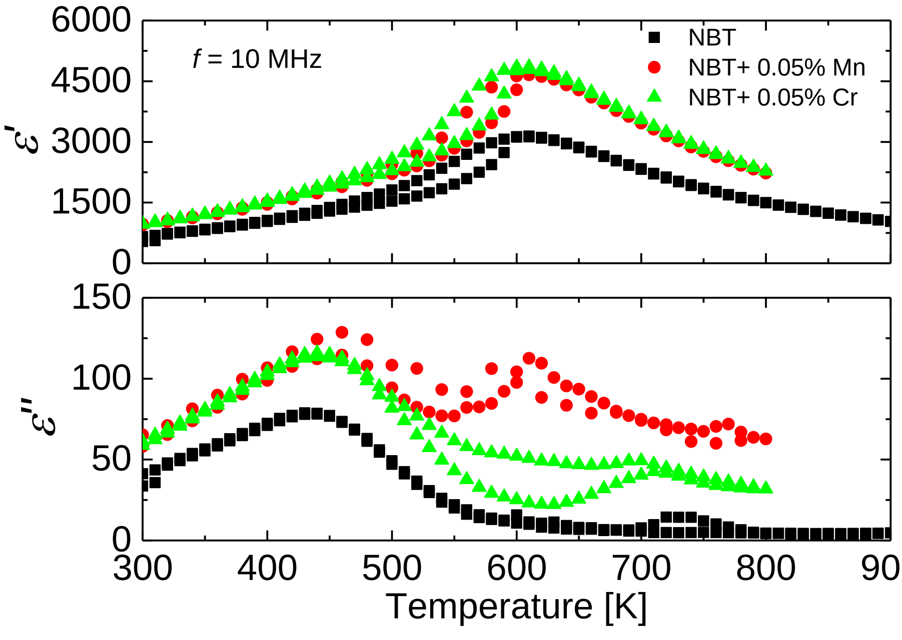

Figure 4.1.5 Comparison of temperature dependences of complex dielectric permittivity of NBT, NBT:Mn and NBT:Cr single crystals.

The DC conductivity at high temperatures was analyzed in order to explain the possible Cr and Mn states in the NBT single crystal. Figure 4.1.6 represents temperature dependences of DC conductivity of all three crystals.

The activation energy of DC conductivity of pure sodium bismuth titanate is 1.6 eV. This value correlates well with a half value of the band gap[156] (as well as with the value obtained for polycrystalline NBT[157]). This means that the conductivity in NBT single crystal is purely intrinsic (i. e. it stems from the intrinsic electrons which are excited to the conduction band) at the highest temperatures. The DC conductivity was determined only above the permittivity peak temperature. The conductivity significantly drops below the peak and thus it is impossible to determine the DC value reliably.

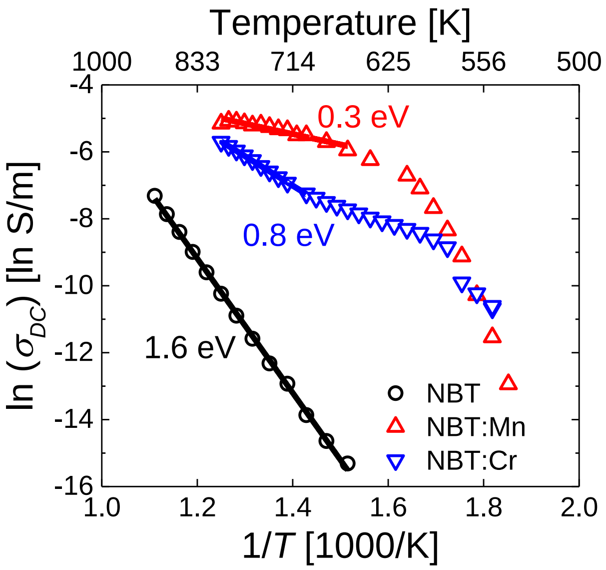

Figure 4.1.6 Temperature dependences of static conductivity in NBT, NBT:Mn and NBT:Cr single crystals. The data is represented in 550 - 900 K temperature were static conductivity can be reliably determined.

The DC conductivity increases with both Cr and Mn doping. The highest temperature region can well be fitted with an Arrhenius law. This indicates that both dopants introduce impurity levels in the band gap of NBT. The activation energies of Mn and Cr doped NBT are different. This hints that the oxidation state of these two dopants is different. The dc conductivity depends on the concentration of charge carriers and the mobility. The temperature dependence of mobility depends on the scattering mechanisms of charge carriers. In the current case there is no reason why scattering mechanism should be dependent on the type of dopants. The reasonable explanation is that the oxidation states of Mn and Cr are different in the NBT crystal. Cr^{4+} state is least probable. It is safe to assume that the Cr^{3+} ions are dominating in the B-site of the doped crystal. The larger conductivity in NBT:Mn crystal can be related to the presence of Mn^{2+} ions. Mn^{2+} state should generate more electrons than Mn^{3+}. The more electrons in conduction band the larger the conductivity.

A very significant difference between NBT:Mn and NBT:Cr crystals can be observed in the temperature evolution of DC conductivity. The increase of conductivity with the increase of temperature is due to the ionization of dopants. The slope of conductivity changes when all the impurities are ionized. The gradual increase occurs due to intrinsic electrons being excited to the conduction band when the temperature is increased. The same ideas apply to the Cr-doped sample except that there are less charge carriers to be excited to the conduction band. It is worth noting that below the inclination point, some oxygen vacancy related conductivity manifests in the frequency dependences of conductivity (not shown here).

The presented picture is in agreement with an experiments performed by Maier and Randall[158,159] on classical perovskite oxides $SrTiO_3$ and $BaTiO_3$. It is also in agreement with experiments performed on NBT doped with Mg and Fe impurities[160] where it was shown that samples doped with less than 1 % of impurities has particularly electronic conductivity.

To sum up, the dielectric studies of NBT crystals did not show any characteristic relaxor features in the vicinity of high temperature peak. The low temperature dielectric relaxation was attributed to the domain wall dynamics since the dispersion lies below 1 MHz. This unambiguously shows the significant difference between the dielectric response canonical B-site relaxors and sodium bismuth titanate.

The analysis of conductivity helped to identify the valence states and the role of Mn and Cr doping. Both of these impurities act as an acceptor dopants with a different valence states in the B-site of the perovskite lattice.

4.1.3 Microwave properties of NBT ceramics

The size of previously discussed NBT single crystals was not sufficient for the measurements in the waveguides. Thus, the dense ceramic samples of NBT were investigated at the waveguide frequencies for complete picture of the prevailing contributions to the dielectric permittivity.

The combination of MW (obtained by author) and Terahertz data gave an insight of different contributions to the dielectric anomalies of sodium bismuth titanate.

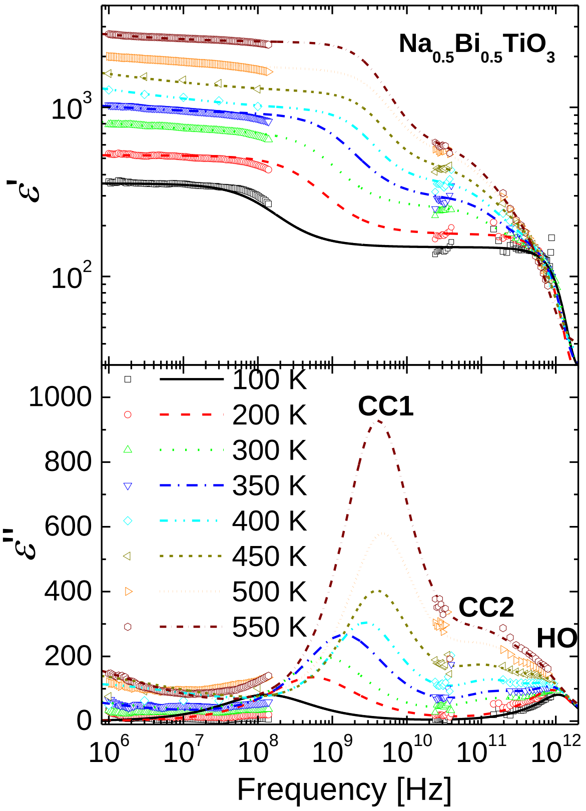

Figure 4.1.7 Frequency dependences of complex dielectric permittivity of NBT ceramics.

Figure 4.1.7 represents the frequency dependences of complex dielectric permittivity of NBT. The solid curves represent the approximation of experimental data. The relaxations are observed above 1 GHz range and are in agreement with previous result on the single crystals. The fitting model consisted of two Cole-Cole relaxations and a damped harmonic oscillator

(HO). The fits at higher temperatures were performed only for the THz data (these fits are not presented here).

The main Cole-Cole contribution (CC1) was introduced to describe the relaxation above 1 GHz. It can be observed in the whole temperature range. The contribution to dielectric permittivity is almost equal to the contribution of harmonic oscillator at low temperatures. The contribution of the central peak significantly increases with an increase of temperature.

Figure 4.1.8 summarizes the temperature dependences of the dielectric strength of different contributions. The graph shows that the contribution of the lowest frequency phonon mode is quite small compared to CC1 relaxation. It is obvious that the main contribution stems from the central peak (CC1 relaxation) and it is the origin of the permittivity maximum around 600 K. This relaxation undergoes a significant softening with a decrease of temperature. A possible scenario is that this is related to the coupling and transfer of the dielectric strength from the harmonic oscillator. The HO does not show any pronounced softening. It actually "hardens" with a decrease of temperature. This is the underlying cause that the Curie-Weiss law is satisfied above the T_m.

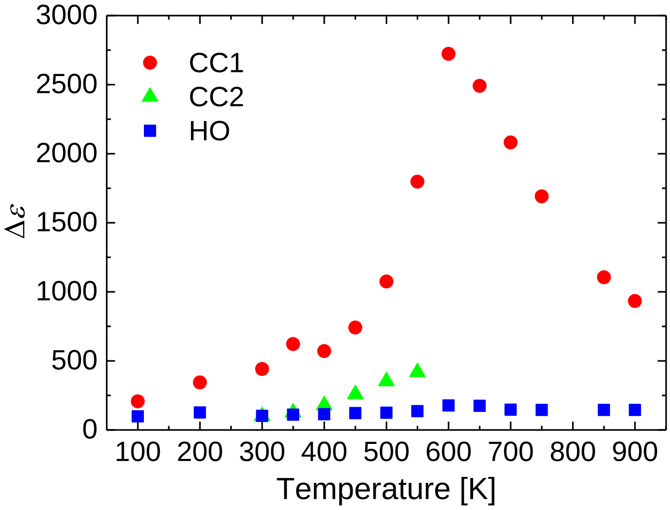

Figure 4.1.8 Temperature dependences of the dielectric strength of different contributions in the dielectric spectra of NBT ceramics.

This peculiar behaviour is related to strongly anharmonic bismuth ion dynamics. It is in agreement with a broad distribution of bond lengths of Bi-

O[110]. This data show that NBT does not act as a typical relaxor. The only common feature of NBT with canonical relaxors is the fact that the anomaly around 600 K cannot be associated to any structural transformations in the material.

4.1.4 Summary

Dielectric spectroscopy of sodium bismuth titanate revealed that the high temperature dielectric anomaly stems from the central mode. NBT cannot be classified as a relaxor since the low temperature dispersion exists only below 1 MHz frequency. The high temperature permittivity peak in NBT does not show any relaxor-like dispersion. This relaxation is due to the strong anharmonic behaviour and hopping of bismuth ions.

The studies of DC conductivity revealed that the Mn and Cr dopants occupy the B-site in sodium bismuth titanate. Significantly larger conductivity of NBT:Mn crystal revealed that Cr and Mn ions have different valence states in the B-site. Mn ions either exist in 2+ states or a mixed state between 2+ and 3+. Cr ions have only 3+ valence state because a conductivity of NBT:Cr sample is lower than NBT:Mn crystal.

4.2 Lattice dynamics and piezoelectricity in relaxor-lead titanate solid solutions

The complex solid solutions where the end members of phase diagram are relaxors and canonical ferroelectrics are of great scientific and technological significance. The phase diagrams of such compositions exhibit morphotropic phase boundary which is a hallmark of excellent dielectric, piezoelectric and ferroelectric properties[161–165]. The solid solutions of relaxors mixed with a lead titanate are capable to compete with the most prominent piezoelectric material lead zirconate titanate which is a solid solutions between classical ferroelectric lead titanate[76,77] and antiferroelectric lead zirconate[166,167].

Lead titanate takes a special place amongst other canonical ferroelectrics in the perovskite oxide solid solutions. The outstanding dielectric and electromechanical properties can be achieved in the solid solutions between canonical relaxors PMN and PZN and lead titanate[168–170]. The properties of lead ions in the perovskite lattice play a crucial role for an excellent piezoelectric performance in these materials[171].

Morphotropic phase boundaries can be found in other solid solutions with different compounds. Recently, one of the most popular complex solid solutions are based on ferroelectric barium titanate and other lead-free perovskites resembling relaxor ferroelectrics[104,172]. An enormous attention to the lead-free piezoceramics arose due to the Restrictive of Hazardous Substances directive by the European Union. Unfortunately, lead-free materials are still behind the lead-based compounds and hardly meet the requirements provided by the lead titanate based solid solutions[6,103,105,106,173].

The lattice dynamics and piezoelectric properties will be presented in two complex relaxor-PT solid solution systems. The difference between these two systems is the lattice site where the charge disorder is present in the relaxor counterpart.

One of them is the commercial PMN-17PT (001) single crystals with a charge disorder in the B-site. The second system is $(0.4\text{-}y)\mathrm{Na_{0.5}Bi_{0.5}TiO_3}$-

$0.6SrTiO_3$-$y$$PbTiO_3$ solid solutions (polycrystalline) where the lead free $0.4Na_{0.5}Bi_{0.5}TiO_3$-$0.6SrTiO_3$ represents the relaxor part. It has a charge disorder in the A-site.

4.2.1 $0.83PbMg_{1/3}Nb_{2/3}O_3$-$0.17PbTiO_3$ single crystals

The PMN-*x*PT is one of the most extensively studied perovskite oxide ferroelectrics. It is composed of what is now considered as a canonical relaxor ferroelectric PMN and ferroelectric PT. There are several reasons which make this system so attractive. First of all, it is possible to sinter any composition throughout the phase diagram (see Figure 4.2.1) quite easily. It is even possible to grow quite large high quality single crystals. It has become a model system of the disordered perovskite oxides.

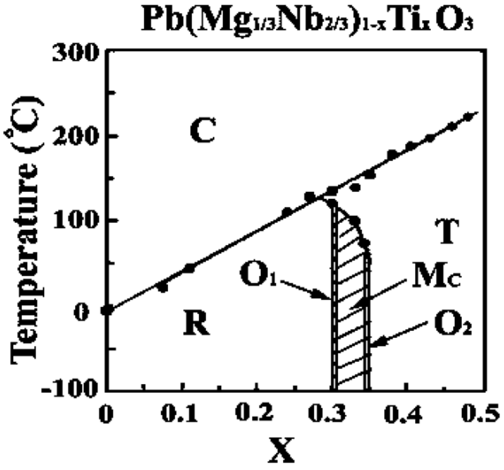

Figure 4.2.1 Phase diagram of PMN-xPT solid solutions. The diagram is reprinted from Guo et al.[174] with the permission of IOP publishing. Solid circles are taken from Shrout et al.[164].

It is widely accepted that the charge disorder in the perovskite lattice is responsible for the appearance of random fields. The random fields prevent the formation of long range order. The increase of PT in the PMN-xPT solid solutions controls the strength of RFs. The titanium ion is electrostatically compatible in the $A^{2+}B^{4+}O_3$ perovskite lattice. It substitutes the $(Mg_{1/3}Nb_{2/3})^{4+}$

in the lattice thus reducing the local charge disorder which is due to the different valence of Mg and Nb ions.

The increase of PT content in the solid solutions promotes the ferroelectric long range order which fully develops to more or less proper ferroelectricity only above the MPB which is around $x = 0.3$[174,175]. The compositions below the MPB undergo relaxor-normal ferroelectric phase transitions from certain concentration of x. Such phase transitions are often observed in a disordered perovskites. These phase transitions are of strong 1st order character but the lattice does not transform to the ideal symmetric phase[176] above the transition temperature. It rather goes to the relaxor phase with often broad dielectric relaxation and properties similar to canonical relaxors[11,177].

The compositions below the MPB are less systematically studied. In many papers the Curie temperature of these compositions are presented as the temperature of permittivity peak at low frequencies[114,178,179]. This is quite contradictory with the structural data presented in the literature. For example, structural phase transition in PMN-10PT was identified by the XRD studies to be around 280 K[180]. This is 20 K lower than the transition line extrapolated in the phase diagram by Ye et al.[178]. The XRD data is supported by Raman studies of Slodczyk et al.[181]. An XRD studies of low PT content compositions showed that the rhombohedral distortion appears in PMN-xPT even for the compositions with $x = 5$ %[182]. The structural analysis by neutron scattering strongly opposes the XRD data. Gehring and co-workers published several papers on the structure of few compositions below the MPB. The same PMN-10PT did not show any rhombohedral distortions even below 100 K temperature[183]. They concluded that the rhombohedral phase observed in the XRD experiments is related to the surface effects (as they call it, anomalous skin effect). Similar skin effect was identified in some other compounds[184]. Indeed, the penetration of X-rays to the sample is strongly dependent on the energy of X-rays. Other neutron studies showed that the structural phase transition occurs only for the compositions above $x = 25$ % of PT[179]. Recent theoretical studies by molecular dynamics also hint that structural ferroelectric phase transition is absent in PMN-25PT[185]. This structural ambiguity has not been resolved even though some of the papers referenced above are older than 15 years. The compositional range where the cubic-rhombohedral structural phase transition exists is debatable in PMN-xPT phase diagram.

PMN-17PT single crystal is below the MPB and in the compositional region where not so many data on lattice dynamics and ferroelectricity have been reported. This crystal is believed to have intermediary strength of random fields. By combining broadband dielectric spectroscopy and investigation of ferroelectric and electromechanical response the formation of long ferroelectric order and its features will be elucidated. This will help to bridge the knowledge between strong RFs perovskite oxides like PMN and compositions above the MPB where the influence of random fields is negligible. It will be shown that the phase transitions appearing in such intermediary systems can be considered as an order-disorder type. The presence of charge disorder possibly masks the characteristic features of an order-disorder phase transitions which can be observed in less complex systems. The temperature evolution of ferroelectric phase will be investigated and discussed in the framework of temperature dependences of polarization and electromechanical properties.

4.2.1.1 Broadband Dielectric Spectroscopy

Figure 4.2.2 represents the temperature dependences of complex dielectric permittivity in PMN-17PT single crystal. Dielectric anomaly is associated with the ferroelectric phase transition at around 330 K from cubic to rhombohedral phase[114,174]. A broad dispersion above the phase transition is observed. The maximum of dielectric permittivity at different frequencies occur at different temperatures. Although, it is important to stress that the shift of dielectric maxima is negligible at frequencies below 1 MHz. The larger shift occurs at microwave frequencies and is clearly observed in the 8 and 29 GHz curves. Additional anomaly can be observed in the temperature dependence of imaginary part (Figure 4.2.2b). This feature only appears at frequencies below 1 MHz. This anomaly can be related to the domain wall motion because it is observed in the ferroelectric phase. Another possibility is that this effect is extrinsic and related to the sample-electrode interface although we neglect this assumption because electrodes were produced with a different conditions (different silver pastes with different annealing temperatures) and the same feature was observed in the experimental data. The Brillouin studies by Kim et al.[186] revealed anomaly in the same temperature region (~320 K) during field-cooling/field-heating experiments. We can conclude that the anomaly we observe is an intrinsic feature of PMN-17PT single crystals.

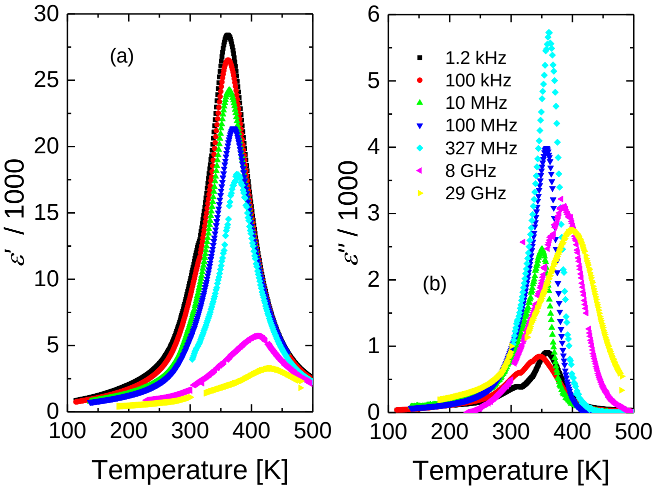

Figure 4.2.2 Temperature dependence of complex dielectric permittivity at different frequencies of the PMN-17PT single crystal.

The dielectric anomaly in the PMN-17PT single crystal is not as sharp as in classical 1st order phase transition; it exhibits particular “diffusivity”. Such picture reminds of organic ferroelectrics with an order-disorder type phase transitions. This phase transition shows very peculiar behaviour. It is expected to observe the minimum in the temperature dependences of dielectric permittivity at certain frequencies (so called critical slowing down). In the present case such minimum was not observed.

The absence of minimum can be explained after the analysis of dielectric spectra which are depicted in Figure 4.2.3. Solid curves represent the approximation by superposition of two empirical Cole-Cole equations (Eq. 4.2.1). One of the components describes the broad feature of spectra which give rise to a constant loss region at the lowest frequencies (it can be considered as a background to a main relaxation). Another component describes the main relaxation which mostly appears at microwave frequencies. The structure of the dielectric spectra in PMN-17PT closely resembles canonical relaxors.

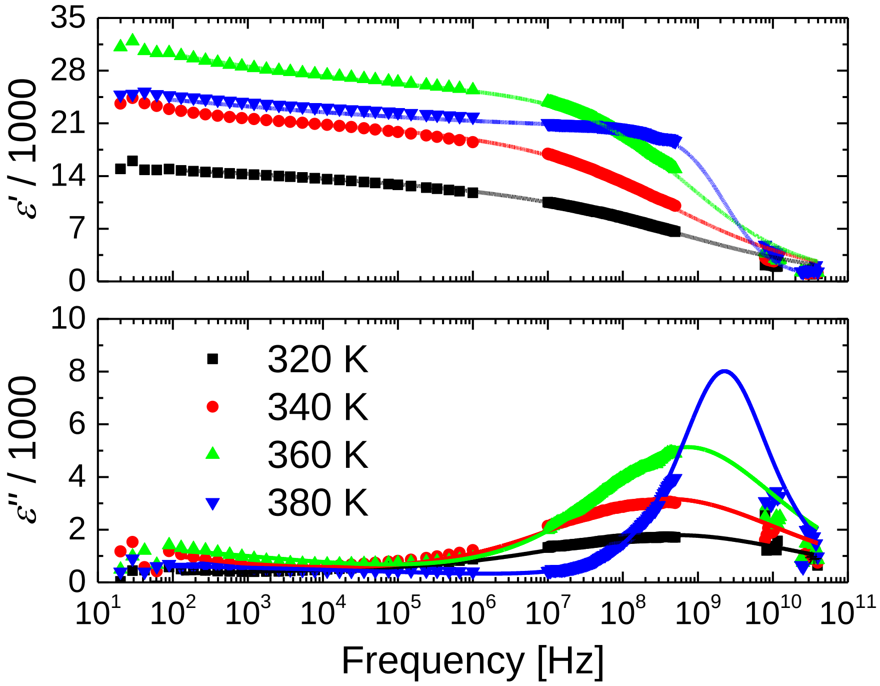

Figure 4.2.3 Frequency dependence of complex dielectric permittivity at different temperatures for a PMN-17PT single crystal.

$$\varepsilon^*(\omega) = \varepsilon_\infty + \frac{\Delta\varepsilon_1}{1+(j\omega\tau_1)^{1-\alpha_1}} + \frac{\Delta\varepsilon_2}{1+(j\omega\tau_2)^{1-\alpha_2}} \qquad (4.2.1)$$

The distribution of relaxation times in the PMN-17PT single crystal is much broader than Debye-type relaxation. The minimum in order-disorder type systems is observed for the materials where the dielectric dispersion is close to the Debye relaxation. Any broadening of the spectra is masking the minima. This can be easily shown by the modelling of 2nd order phase transition (refer to APPENDIX I).

The Cole-Cole relaxation time was analysed more carefully (Figure 4.2.4). It is well accepted that relaxor ferroelectrics undergo freezing which is described by Vogel-Fulcher law. This freezing phenomenon manifests as the divergence of characteristic relaxation time vs. temperature. One of the key signatures of the freezing in relaxor ferroelectrics is the constant loss regime observed at low temperatures. The constant loss regime hints that the distribution of relaxation times in the system becomes infinitely broad. In our case, the PMN-17PT crystals undergo structural phase transition from relaxor-like to normal ferroelectric phase. It is difficult to discuss such system in the framework of Vogel-Fulcher law because the long range ferroelectric order onsets before the freezing supposed to appear. The parameters which are obtained by describing characteristic relaxation time by Vogel-Fulcher law have questionable physical meaning.

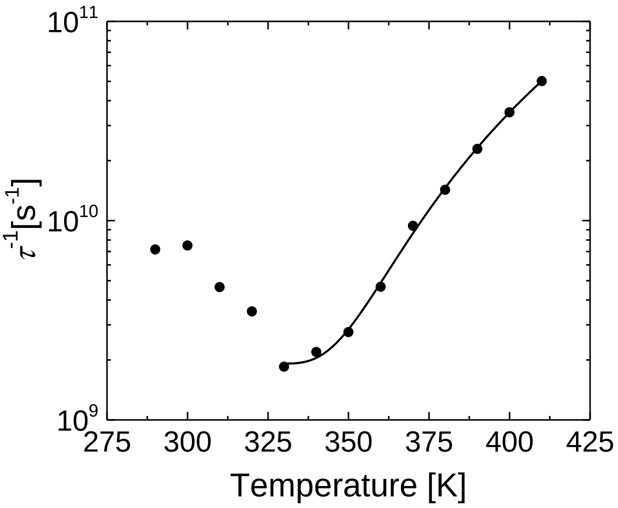

Figure 4.2.4 Temperature dependence of inverse mean relaxation time. Solid line is approximation with the critical slowing down model.

$$\frac{1}{\tau_{mean}} = \frac{1}{\tau_0} + \frac{1}{\tau_1}\left(\frac{T-T_C}{T_C}\right)^{\beta} \tag{4.2.2}$$

The latter statements require another approach for analysing mean relaxation time. Thus, the modified order-disorder model (Eq. 4.2.2)[86] was applied for the analysis. The solid curve in Figure 4.2.4 is approximated by Eq. 4.2.2. The critical slowing down model is capable to describe the mean relaxation time of higher temperature phase. There are four fitting parameters which are presented in Table 4.1. One of them is the phase transition temperature (Curie temperature) which correlates with the phase diagrams by Noheda et al. and Guo et al.[114,174].

Table 4.1 Parameters obtained from the critical slowing down model.

$\frac{1}{\tau_0}, s^{-1}$	$\frac{1}{\tau_1}, s^{-1}$	T_C, K	β
1.9×10^9	2.7×10^{12}	330	2.8

Parameter β for proper order-disorder type phase transitions should be equal to 1. For the PMN-17PT this parameter is 2.8. The interpretation of such value is related to the large random fields in PMN-PT. Similar value was obtained for the PZN-PT[86] single crystals which are known to have strong random fields. Parameter τ_0 indicates that the minimum in the temperature dependence of dielectric permittivity should be observed at microwave frequencies (waveguide region above 2 GHz). Unfortunately, the experiments did not show the minimum in microwave dielectric data.

The determination of the phase transition type (order-disorder or displacive) is quite a difficult task. Order-disorder type phase transitions are mostly observed in organic ferroelectrics such as KDP[187], TGS, TSCC[188,189]. It is difficult to find systems of order-disorder type in inorganic compounds as perovskite oxides. As mentioned before there are evidence that classical ferroelectrics demonstrate a coexistence of order-disorder and displacive phase transitions[24–27]. The microscopic origin of polarization is off-centering of cations in the perovskite oxides. Therefore, in the temperature range far from T_C, the displacive nature is dominant. However, in the vicinity of T_c, the shallow minima of the potential (for example, the 8-site model in $BaTiO_3$) cause the order-disorder nature and the soft mode becomes overdamped. However, in vibrational spectroscopy, it is difficult to distinguish between overdamped soft mode and relaxation process of order-disorder nature in the vicinity of T_C.

Order-disorder and displacive models of phase transition are examined under the assumption of homogeneity. Relaxors, on the other hand, are heterogeneous systems and are often considered as order-disorder systems[190] although the picture is much more complicated. In general, Mg ions favor on-centered, while Nb and Ti ions favor off-centered (ferro-active) positions. Far above the Curie temperature, Nb and Ti ions show the displacive nature, but in the vicinity of T_c the order-disorder nature according to the 8-site model is fulfilled. The charge disorder and lattice mismatch by the random occupation of three different cations may be the cause of the diffusive nature of soft mode. In addition, off-centered cations might couple to the off-center Pb ions which may also show order-disorder nature. These off-center displacements in shallow potential minima can be the origin of the fact that the minimum of dielectric permittivity near T_C is smeared (refer to APPENDIX I).

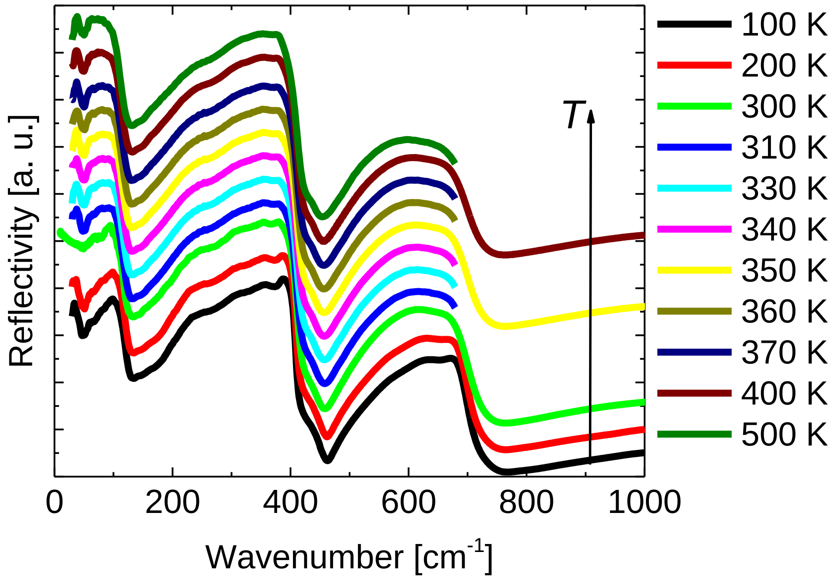

Figure 4.2.5 Temperature dependences of FTIR spectra in PMN-17PT single crystals.

The temperature evolution of the IR spectra is depicted in Figure 4.2.5. There are no significant changes in the spectrum above 200 cm^{-1}. The only minor change is that some of the features coalesce into one broad band. Some of the vibrations can be distinguished only at low temperatures. There are no frequency shifts in the spectra. This means that the contribution of phonons to the dielectric permittivity is constant.

There are some changes in the lowest frequency TO phonon mode (i. e. below 140 cm^{-1}). The TO mode around 95 cm^{-1} changes with an increase of temperature. The whole band in this frequency region gets broader. This indicates the change in the damping of the TO mode. The increase of damping is observed up to 500 K. This kind of behaviour is inherent to relaxors. The phonon spectrum below the T_m becomes underdamped. The phonon in the vicinity of the permittivity peak is heavily overdamped at the Brillouin zone center. It becomes underdamped only above the Burns temperature. The Burns temperature could not be reached with the experimental setup.

The room temperature FTIR spectrum with an addition of THz data show that this overdamped phonon is not related to the low frequency dielectric relaxation. These two components coexist but the main contribution to the dielectric permittivity stems from the central peak. This is another proof that the anomaly in PMN-17PT single crystals has an order-disorder character and has nothing to do with the lowest frequency phonon. These results support the Brillouin scattering data[186].

4.2.1.2 Ferroelectric, Piezoelectric and Pyroelectric Properties

The ambiguity about the presence of the ferroelectric phase transition can only be resolved by the polarization switching experiments. Thus, the investigation of polarization and strain hysteresis is necessary. Figure 4.2.6 represents hysteresis loops of the PMN-17PT single crystals at different temperatures. The sample was heated above the Burns temperature (600 K) and cooled down to room temperature before the experiment. The ferroelectric hysteresis loop is observed at room temperature (the black curve represents the very first measurement after the sample was cooled down). This indicates that the ferroelectric phase in PMN-17PT condenses spontaneously on ZFC. The room temperature phase must be non-cubic. One can argue that the ferroelectric phase is induced by an external electric field. Our case does not show an electric field-induced phase transition at room temperature. Only a single switching peak in current-voltage characteristics is observed. In the case of electric field-induced phase transition, two peaks in current vs. voltage characteristics exist. The loop itself has a different shape (for example, compare hysteresis loops in PMN[89]). Furthermore, the strain vs. electric field has a piezoelectric character. The piezoelectricity cannot manifest in the cubic crystal so it is another justification of a non-centrosymmetric phase, since canonical relaxor ferroelectrics have an electrostrictive character at temperatures where phase transition can be induced by an electric field.

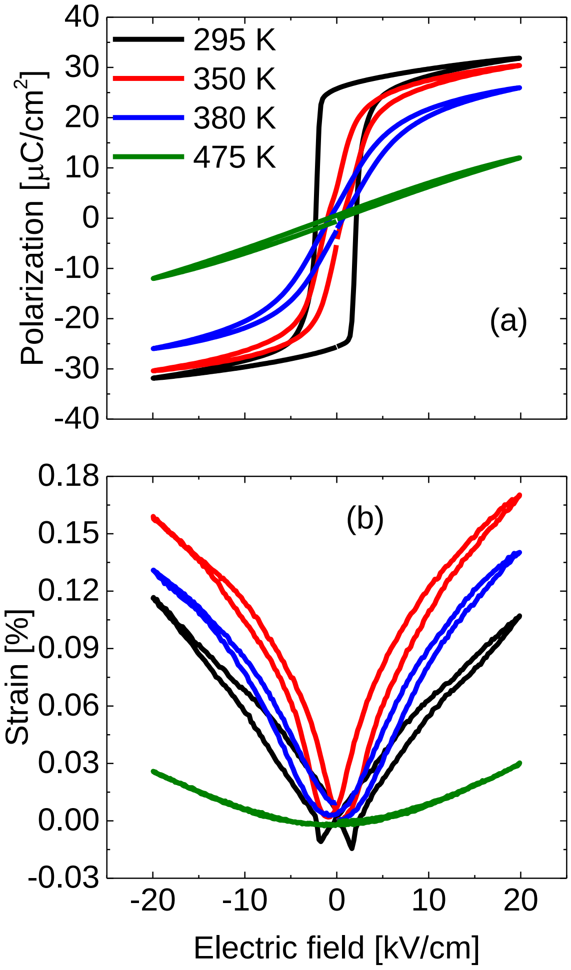

Figure 4.2.6 Electric field dependence of polarization (a) and strain (b) of PMN-17PT single crystals.

The temperature region in the vicinity of a permittivity maximum has rather slim polarization hysteresis loops. This temperature region shows characteristic relaxor ferroelectric hysteresis loops (two peaks in voltamperic characteristics are observed). The electromechanical properties in this region show large hysteretic behaviour which is characteristic to an electric field induced phase transitions in relaxors. It also resembles electrostrictive behaviour. The highest temperature region shows the paraelectric behaviour in both polarization and strain hysteresis. The clear electrostrictive character is observed in strain vs. field plot. This is usual behaviour for cubic perovskite oxides.

Further investigations of polarization and strain hysteresis were carried out by applying unipolar electric field with a different amplitude in order to clarify the non-existence of an electric field induced phase transition. Figure 4.2.7 represents the electric field dependence of polarization at 295 K. The induced polarization should change linearly with the electric field. This regime was observed for the lowest amplitudes (i. e. up to 0.8 kV/cm). A nonlinear behaviour was clearly observer after applying electric field of 1 kV/cm. The abrupt increase of maximum polarization and large histeretic behaviour was observed. It is related to the ferroelectric switching. The further increase of electric field amplitude revealed the linear behaviour.

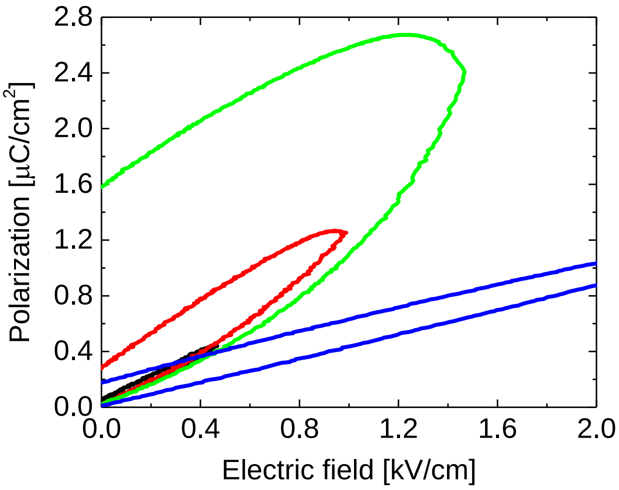

Figure 4.2.7 Electric field dependence of polarization in PMN-17PT single crystal at 295 K temperature.

The maximum induced polarization is larger for lower fields (i. e. below 1 kV/cm). It might be related to the reversible (nano-)domain wall movement. The unpoled sample is in a polydomain state. Several different domains and domain walls can exist. These walls are very sensitive to an external electric field and thus can be moved easily. Such movement gives larger contribution to induced polarization (via contribution to dielectric permittivity). After certain value of the electric field the sample switches to a different state. The field value of 1 kV/cm corresponds to that reported by Helal et al. where the single LA mode splits into two peaks[191]. They also reported about another transition to macroscopic monodomain structure at higher fields, but in our polarization experiments no correspondance to this value was detected. It is expected that the field of 1 kV/cm is sufficient for driving the sample to a single domain state. Concentration of domain walls decreases drastically (or disappears completely) after applying such field. The absence of domain walls would explain the decrease of inclination of induced polarization at higher fields. The contribution to the induced polarization solely comes from the lattice. This experimental result is a strong evidence that the phase transition is not being induced by the field but rather the field drives the sample to a single domain state.

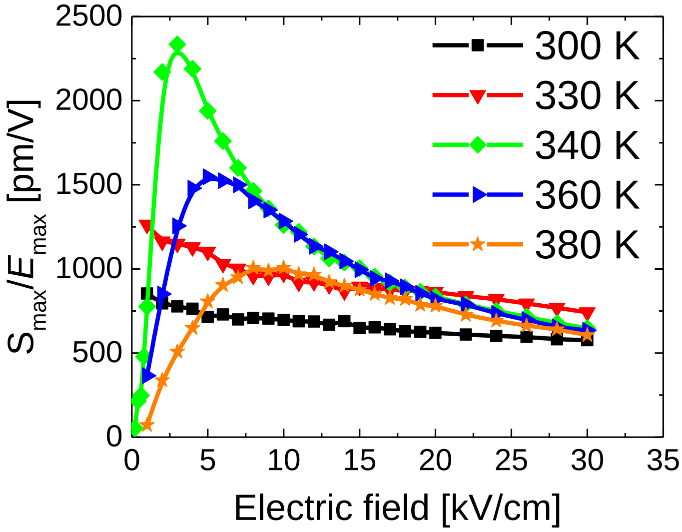

Figure 4.2.8 Electric field dependence of the effective d_{33} coefficient at different temperatures.

Field dependence of electromechanical behaviour was investigated for a single domain sample. Figure 4.2.8 represents the ratio of maximum strain to electric field amplitude. This ratio roughly represents the value of piezoelectric coefficient d_{33} (we will call this ratio as effective d_{33}) for certain amplitude of electric field $E_{\max}$ in a monodomain ferroelectric phase (black and blue curves in Figure 4.2.8). The electric field dependence of effective piezoelectric coefficient d_{33} shows weak dependence on the maximum value of the applied electric field. This shows that there are no additional contributions to the strain and we can conclude that the poled sample is fully monodomain.

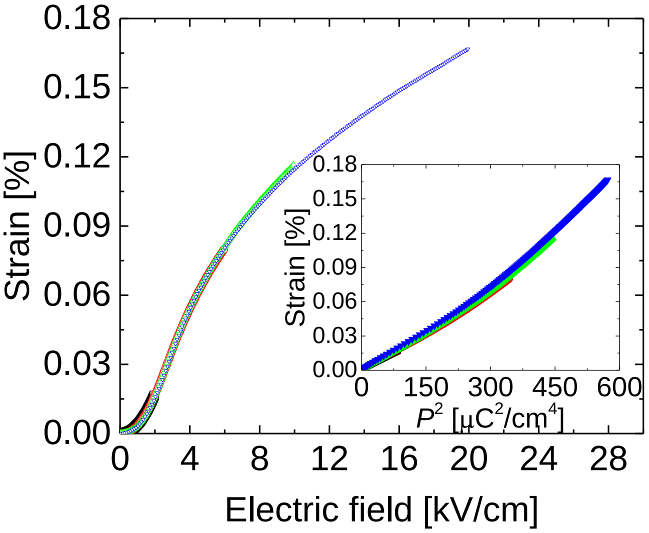

Figure 4.2.9 Electric field dependence of strain at 360 K. The inset represents strain vs. the square of polarization.

The electric field dependence of effective piezoelectric coefficient d_{33} becomes more complicated above the 330 K (green curve in Figure 4.2.8). The $d_{33}(E_{max})$ function appears to have a maximum. This maximum is closely related to the electric field inducible phase transition. The long range ferroelectric order is lost above 330 K but still can be induced by an electric field. This is the true E-field inducible phase transition region in PMN-17PT and it only appears above 330 K. The strain vs. electric field has a different physical nature below and above this maximum. The strain at low field regime is due to the electrostriction. The electromechanical response can be considered as a piezoelectric effect above the maximum (i. e. after inducing ferroelectric phase). The convergence of the ratio S_{max}/E_{max} to the room temperature value (i. e. black curve) hints the same physical origin of the strain. The quadratic field dependence of strain at low fields (at low fields $P \sim E$) is evidenced in Figure 4.2.9. The inset of Figure 4.2.9 shows the linear behaviour of strain vs. the square of polarization and unambiguously identifies the electrostrictive behavior at the lowest field. The change of the slope can be observed at higher values of polarization. This is related to the electric field inducible phase transition and indicates the change of electromechanical response. Surprisingly, the dependence of strain is nearly linear at the highest fields. The strain at 340 – 400 K temperature range can be described by two distinct electrostriction coefficients Q_{11}. The Q_{11} of high field region is larger by roughly 20 % compared to the low field region. This is quite confusing result bearing in mind that ratio S_{max}/E_{max} at higher fields mimics the same behaviour as in a monodomain ferroelectric state. The strain *vs.* P^2 suggests that the strain can be described by electrostrictive type behaviour in an E-field induced phase. The temperature dependences of Q_{11} and small signal d_{33} can be found in the Figure 5 of APPENDIX I.

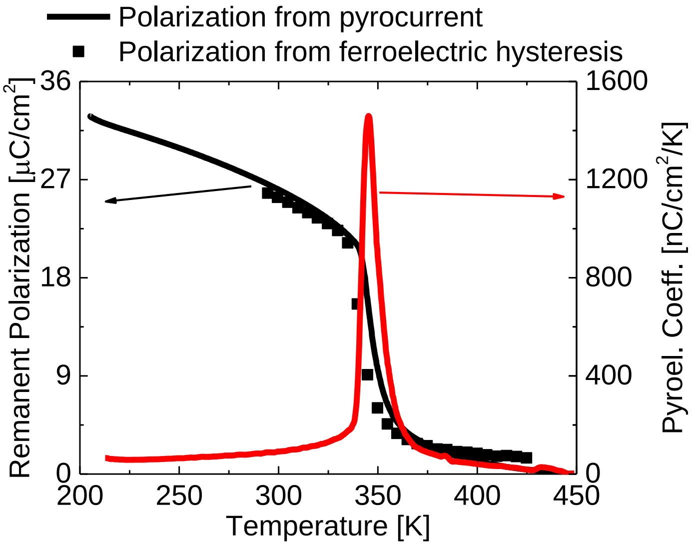

Figure 4.2.10 Temperature dependence of remanent polarization and pyroelectric coefficient.

Temperature dependences of pyroelectric coefficient and remanent polarization are depicted in Figure 4.2.10. The data which was obtained from the ferroelectric hysteresis loops (i. e. Figure 4.2.6(a)) is consistent with the pyroelectric measurements. The poled PMN-17PT undergoes a first order phase transition. The abrupt polarization drop is observed at the temperatures which correlated with the permittivity maximum (see Figure 4.2.6(a)).

Unfortunately, this temperature does not correlate with a critical slowing down temperature which was obtained from the dielectric spectra[192]. There was also an attempt to perform pyroelectric measurements for the unpoled sample. Even in the unpoled sample (not presented here) the peak can be detected at the same temperatures as for the poled sample. Pyrocurrent measurements are very sensitive for the structural changes and the data on the unpoled sample supports the idea that the structural phase transition exists in PMN-17PT.

Above the 350 K temperature pyroelectric data show non-zero remanent polarization indicating that there are static PNRs which contribute to the pyrocurrent. The small remanent polarization above the permittivity peak maximum was observed in pure PMN[49] as well.

4.2.1.3 Local Piezoelectric Response

The macroscopic experimental data strongly support presence of the spontaneous ferroelectric phase transition in PMN-17PT single crystals. On the other hand, such experiments might not be sensitive enough for very small structural changes. This would be very important if the coercive field and the field that is necessary to induce ferroelectric order would be nearly equal in magnitude. In such a case more sophisticated experiments would be required to unambiguously detect the structural phase transition.

The ferroelectric phase should exhibit domain structure in the ferroelectric phase. It should abruptly disappear above the phase transition temperature. The domain structure can be easily probed by the piezoresponse force microscopy. The PFM studies were performed on the unpoled PMN-17PT single crystal.

Figure 4.2.11 and Figure 4.2.12 represents the Vertical (first column) and Lateral (second column) PFM images at room temperature. On a larger scale (Figure 4.2.11) the significant PFM contrast can be observed in the amplitude of VPFM image (Figure 4.2.11(c)). The LPFM images barely show any PFM response. This is the evidence that the polarization is perpendicular to the scanned surface. This corresponds to the (001) pseudocubic direction of the crystal.

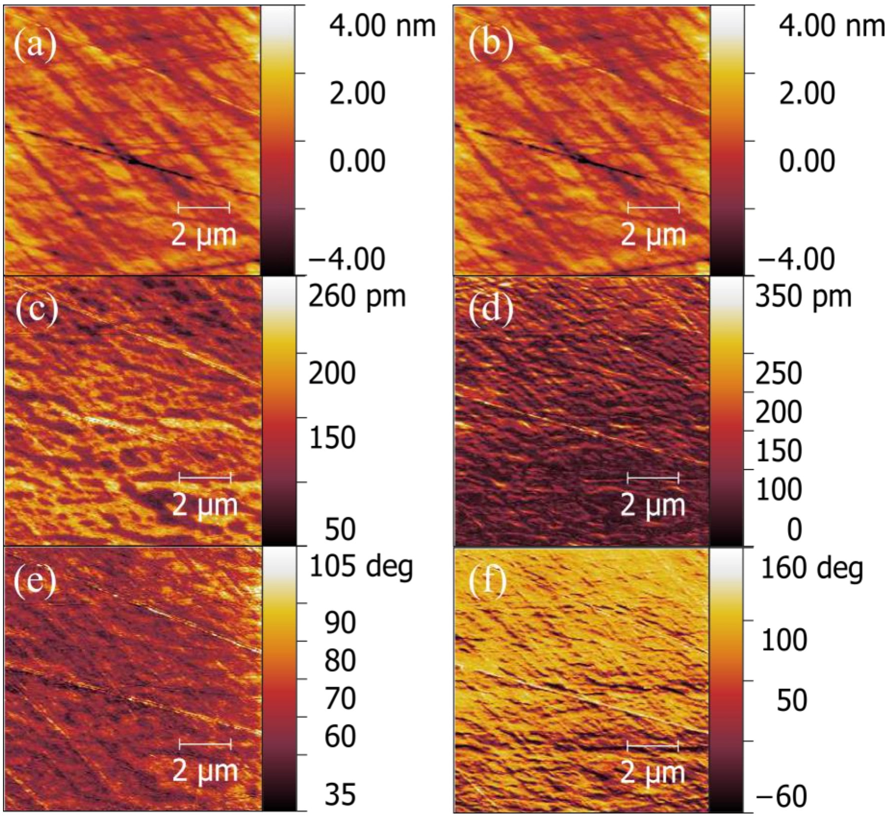

Figure 4.2.11 Room temperature PFM images of PMN-17PT single crystal. First column represents vertical response; second column represents lateral response. Image (a), (b) represents the topography of the scanned area; (c), (d) represents the amplitude; (e), (f) represents phase. The scanned area was 10 ^{x} 10 µm^{2}.

The same picture in Lateral images can be observed for larger magnification (second column of Figure 4.2.12). This shows that the Lateral polarization is much smaller or absent in the PMN-17PT single crystal. The VPFM images show distinct polar structure which is even observed in the phase image (Figure 4.2.12(e)). The vertical images exhibit lamellar structure. A very similar patterns were observed by Kholkin and Shvartsman in PMN-20PT single crystals[193]. They reported two distinct types of polar structures in PMN-20PT. The larger domains have same lamellar shape as observed in PMN-17PT single crystal. The other polar structure in PMN-20PT which is not observed in PMN-17PT is small nanosized domains which are embedded in the larger domains and have opposite direction[193]. The dimensions of larger domains in PMN-17PT are similar to the ones in PMN-20PT.

Slightly different situation can be observed in PMN-10PT single crystals[194]. The domains in PMN-10PT resemble the lamellar structure but they are not as coarse as in the larger PT compositions. It is clear that the increase of PT content increases the size of larger domains yet preserving the same topology of the polar structure.

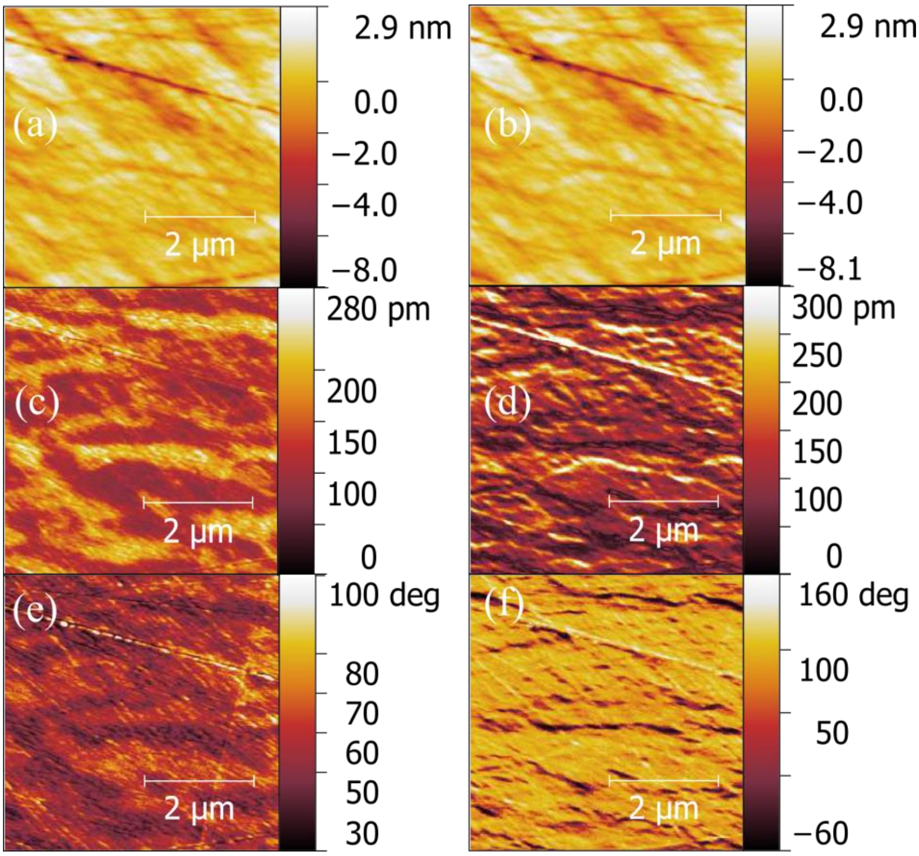

Figure 4.2.12 Room temperature PFM images of PMN-17PT single crystal. First column represents vertical response; second column represents lateral response. Image (a), (b) represents the topography of the scanned area; (c), (d) represents the amplitude due to piezoelectric displacement; (e), (f) represents the phase of displacement. The scanned area was 5 × 5 µm^2.

The temperature evolution of VPFM signal is depicted in Figure 4.2.13. The PFM images are presented in 3 characteristic temperatures according to the dielectric permittivity data (see Figure 4.2.2): i) at room temperature, below permittivity peak (first column); ii) in the vicinity of the permittivity peak at low frequencies (second column); iii) above the permittivity peak (third column). The piezoresponse can be observed at all the images of amplitude (row 2 in Figure 4.2.13). Almost the same applies for the phase images (row 3) except for the 400 K image where the polar structure is less visible. This indicates that with the increase of the temperature the piezoresponse signal decreases but still is preserved above the permittivity peak (please note that the scales are different but the important thing which indicates the decrease of PFM signal is the visibility of topography in the row 2 and 3).

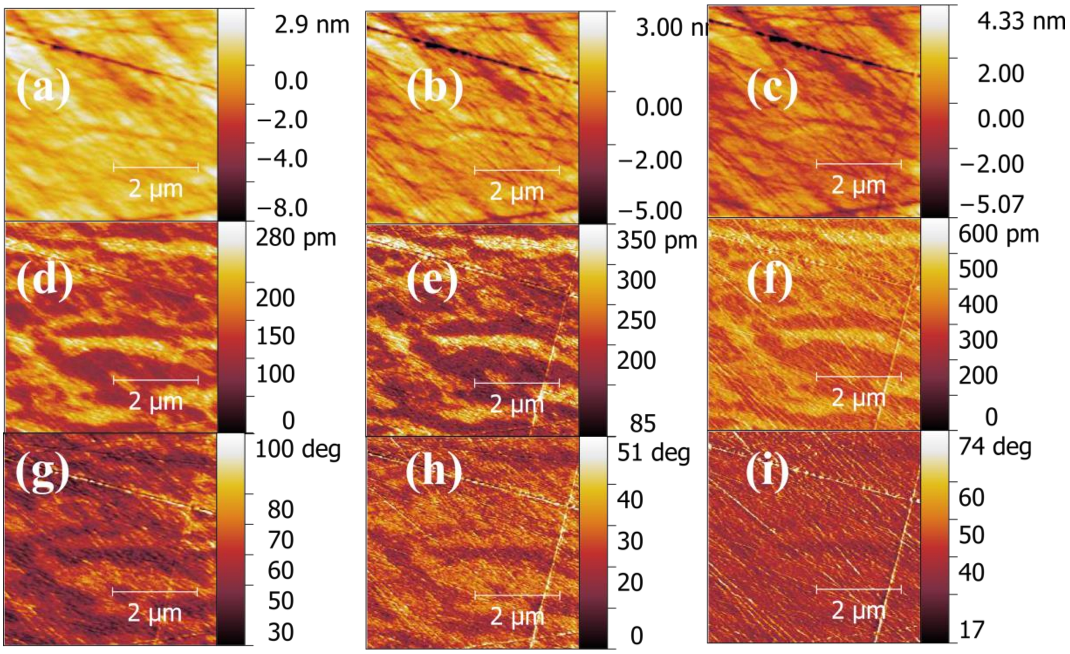

Figure 4.2.13 Vertical PFM response of PMN-17PT single crystal at different temperatures. First column represents the scans at 295 K; second column at 350 K; third column at 400 K. First row represents the topography; second row represents amplitude; third row represents phase. The scanned area was 5 × 5 µm^2.

The macroscopic response (Figure 4.2.6) show significant differences at the same temperatures compared to the PFM images. This hints that with an increase of temperature the random fields start to play a crucial role and decrease the correlation length. This means that the domains which are nearby do not interact yet preserve its polar nature locally. Shvartsman et al.[40] concluded that in some PMN-*x*PT compositions the ferroelectric order develops in a broad temperature range. Interestingly, no abrupt changes can be observed in the PFM images. Some 1st order characteristics of macroscopic properties should imply that something significant should be observed at the nanoscale as well. It seems that the time-scale which is probed here cannot detect such changes. Some other experiments (TOF ultrasonic data) coupled with the current results hint rather slow kinetics of polar (nano)domains at the mesoscale. It also shows that due to the existence of random fields the ferroelectric phase transitions cannot be associated to purely classical order-disorder or displacive models but all the results indicate that the spontaneous ferroelectric phase transition is present in PMN-17PT.

4.2.1.4 Summary

The studies of lattice dynamics and electromechanical response of PMN-17PT crystal revealed that the ferroelectric order in PMN-17PT nucleates spontaneously despite the questionable presence of the structural phase transition. The transition to the ferroelectric state is of order-disorder nature. No phonon softening was observed and the dielectric relaxation is due to the relaxation mode (so-called central mode).

The PFM studies of local polarization did not reveal any conventional ferroelectric domains. The lamellar like polar regions which are typical for relaxor ferroelectrics were observed in the vertical PFM images.

4.2.2 $Na_{0.5}Bi_{0.5}TiO_3$-$SrTiO_3$-$PbTiO_3$ solid solutions

One of the key which lead to the breakthrough in the lead-free piezoelectric materials was the complex solid solutions with different ions in a different perovskite sites[6,104]. The structural complexity increases the electromechanical performance but is not sufficient enough to compete with the lead-based perovskite oxides. It was found that the lead-based relaxor-PT compositions in the vicinity of MPB undergoes the polarization rotation which is thought to be the origin of the superior piezoelectric performance[195,196]. A similar polarization rotation was identified in pure sodium bismuth titanate (this rotation occurs with the change of temperature)[110].

This chapter deals with a different relaxor-PT system. The charge disorder is situated solely at the A-site of the perovskite lattice. The charge disorder is due to the different valence of sodium and bismuth ions. This can be controlled by substituting sodium and bismuth with an ion of 2+ valence. The lead ion is chosen since it has very similar electronic structure. The lone pair electron of bismuth and lead tend to hybridize with oxygen electronic states. It also tends to different ferroelectric off-centering. Ferroelectric displacements of lead is usually along (001) direction while bismuth tends to off-center in (111) direction. These different displacements of ions could enhance the polarization rotation and piezoelectric properties of the complex solid solutions. Finally, it is expected that the excellent macroscopic properties can be achieved by less lead in the solid solutions. This is important for the environmentally friendly ferroelectric materials. The comparison to the canonical relaxor-PT solid solutions will be presented.

4.2.2.1 Broadband Dielectric Spectroscopy

The dielectric properties of the (0.4-y)NBT-0.6ST-*y*PT solid solutions will be discussed in the direction of the increase of the lead titanate concentration.

The temperature dependences of complex dielectric permittivity of 0.3NBT-0.6ST-0.1PT solid solutions are presented in Figure 4.2.14. A diffuse dielectric anomaly and the shift of permittivity peak to higher temperatures can be observed. The dielectric peak broadens with the increase of frequency and can hardly be visible at 300 GHz curve. The real part of permittivity becomes weakly dependent at such high frequencies (the values of permittivity are close to the static value of the phonon contribution). The temperature change of real part of dielectric permittivity is typical for relaxors.

The imaginary part of permittivity shows some common features to lead-based relaxors. The most important difference is the evolution of the loss peaks at different frequencies. The intersection of different frequency curves in

Figure 4.2.14 is not common to Pb-based relaxors. The picture resembles the evolution of loss peaks in dipolar glasses. In the case of canonical relaxors, the peak in losses at different frequencies moves to higher temperatures. Moreover, the higher the frequency the higher the peak value of the losses. The evolution of the loss curves at different frequencies below the peak coincides with each other down to low temperatures where the so-called constant loss regime (frequency independent losses) is fulfilled. The loss curves in 0.3NBT-0.6ST-0.1PT do not coincide with each other at different frequencies. Such behaviour of loss curves can often be observed in glassy systems and indicates weaker polar correlations.

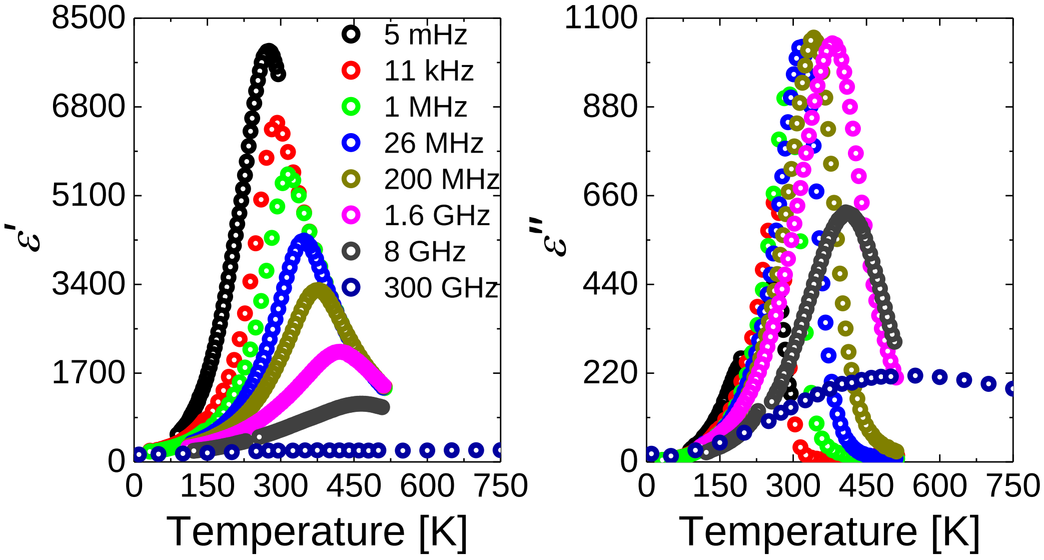

Figure 4.2.14 Temperature dependences of complex dielectric permittivity of 0.3NBT-0.6ST-0.1PT solid solutions at different frequencies.

Surprisingly, the lead role in the 0.4NBT-0.6ST solid solutions depends on which counterpart is being substituted. The relaxor behaviour is much more familiar to lead-based relaxors when the strontium is substituted by lead. The case of 0.3NBT-0.6ST-0.1PT resembles the glassy order-disorder systems. That is quite peculiar behaviour bearing in mind that the replacement of $Na_{0.5}Bi_{0.5}TiO_3$ by lead titanate reduces the charge disorder and thus random fields in the A-site of the perovskite lattice. The substitution of strontium by lead leads to the increase of A-O covalent bonding in the lattice. Due to the increase of covalency, the larger strain occurs in the lattice but the strength of random fields persists. The larger strain affects the random fields and makes the system electrically softer (in terms of response to an external electric field). The stress induced due to the covalent bonding of A-O sites should not change significantly if $Na_{0.5}Bi_{0.5}$ is substituted by the lead. This substitution does not change the correlation length in the system. It might be the reason why 0.3NBT-0.6ST-0.1PT solid solutions resemble the dielectric properties of dipolar glasses. It is important to note that there is a possibility to induce the ferroelectric phase in 0.3NBT-0.6ST-0.1PT solid solutions. The same can be done in 0.4NBT-0.5ST-0.1PT system but the field that is necessary to induce the ferroelectric order is nearly two times lower than in 0.3NBT-0.6ST-0.1PT. The details of this fact will be discussed in the preceding chapters. The difference between the strength of electric field that is required to induce the ferroelectric phase supports the interpretation of the dielectric data.

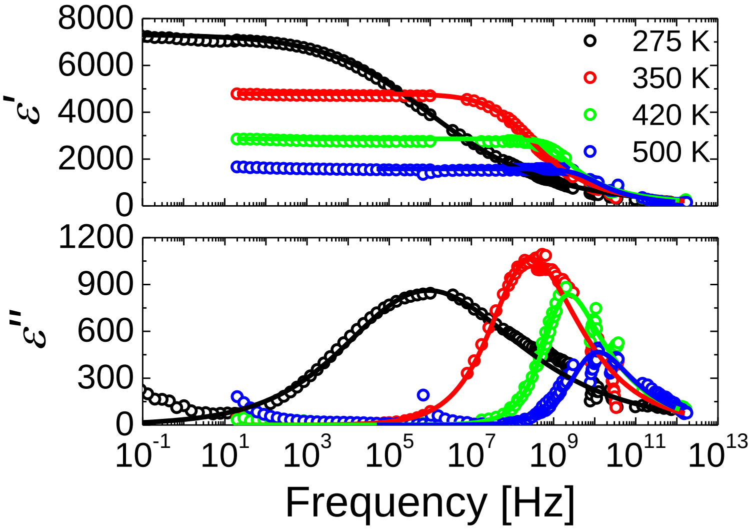

Figure 4.2.15 Frequency dependences of complex dielectric permittivity of 0.3NBT-0.6ST-0.1PT solid solutions at different temperatures.

The frequency dependences of complex dielectric permittivity of 0.3NBT-0.6ST-0.1PT solid solution are depicted in Figure 4.2.15. It is evident that the dielectric relaxation broadens when temperature is decreased. The peak in imaginary part of permittivity shifts to lower frequencies with the decrease of temperature. This means that the mean relaxation time shifts to longer times.

A well expressed asymmetry of dielectric spectra can be observed at low temperatures. The asymmetry persists even up to the highest temperatures. The asymmetry can be observed in the parental composition (0.4NBT-0.6ST)[117]. It significantly decreases with the increase of temperature. The asymmetry parameter β converges to 1 with the increase of the temperature (note Eq. 3.2.5). The strontium substituted composition with 10 mol. % of lead titanate had much weaker asymmetry in the dielectric spectrum[117]. It is possible that despite weaker asymmetry the microwave frequency data is not sufficient to spot the asymmetry in 0.4NBT-0.5ST-0.1PT solid solutions. Besides the well pronounced asymmetry, the dielectric spectra resemble canonical relaxors.

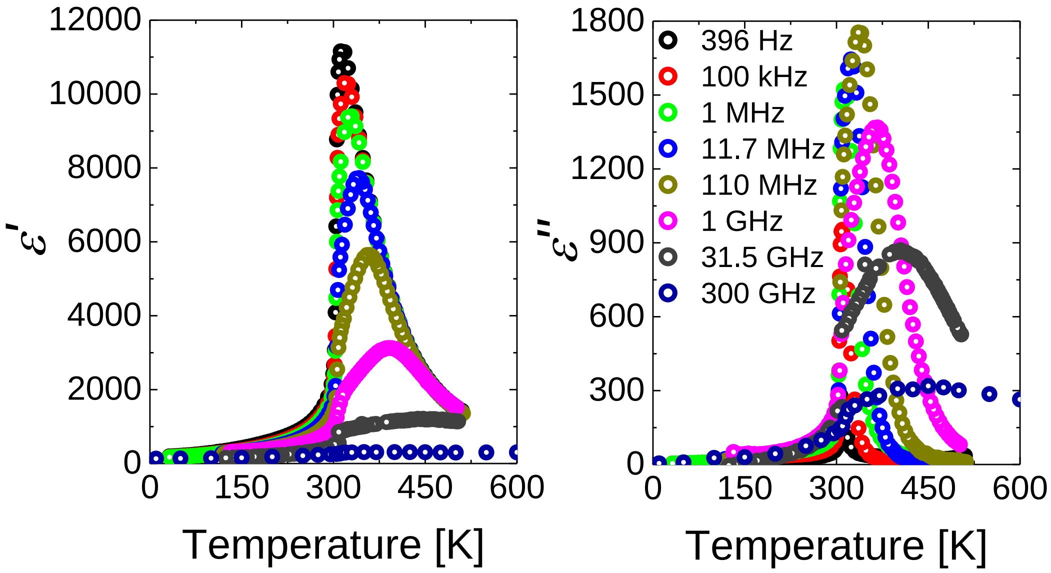

Figure 4.2.16 Temperature dependences of complex dielectric permittivity of 0.2NBT-0.6ST-0.2PT solid solutions at different frequencies.

Figure 4.2.16 represents the temperature dependences of complex dielectric permittivity of 0.2NBT-0.6ST-0.2PT solid solutions. The spontaneous ferroelectric phase transition can be observed in the temperature dependences of complex dielectric permittivity (around 310 K). The phase transition is of first order type since the thermal hysteresis occurs on heating and cooling cycles (refer to Appendix II, same applies for this composition). The dispersion and an obvious shift of the permittivity peak can be observed above the phase transition temperature. This reveals that the high temperature phase is not perfectly cubic. The microscopic polarization fluctuations and random fields start to play a role above the phase transition. Due to a large degree of disorder the polarization fluctuations persists in a quite broad temperature interval. The significant deviation from the Curie-Weiss law can be observed above the phase transition temperature. This shows that the 0.2NBT-0.6ST-0.2PT composition is very close to the relaxor ground state despite the presence of the spontaneous phase transition. The same concentration of the lead titanate introduced in the strontium titanate site in 0.4NBT-(0.6-*x*)ST-*x*PT system drastically increases the temperature of the anomaly[197]. The relaxor anomaly above the transition temperature is situated at higher frequencies (compared to 0.2NBT-0.6ST-0.2PT solid solutions).

This result shows that polar clusters appearing in this system is related to the strain and hybridization of A-O electronic states. The strain due to Pb-O covalency is much stronger. That is the reason the spontaneous phase transition occurs in the system where NBT is exchanged with the PT.

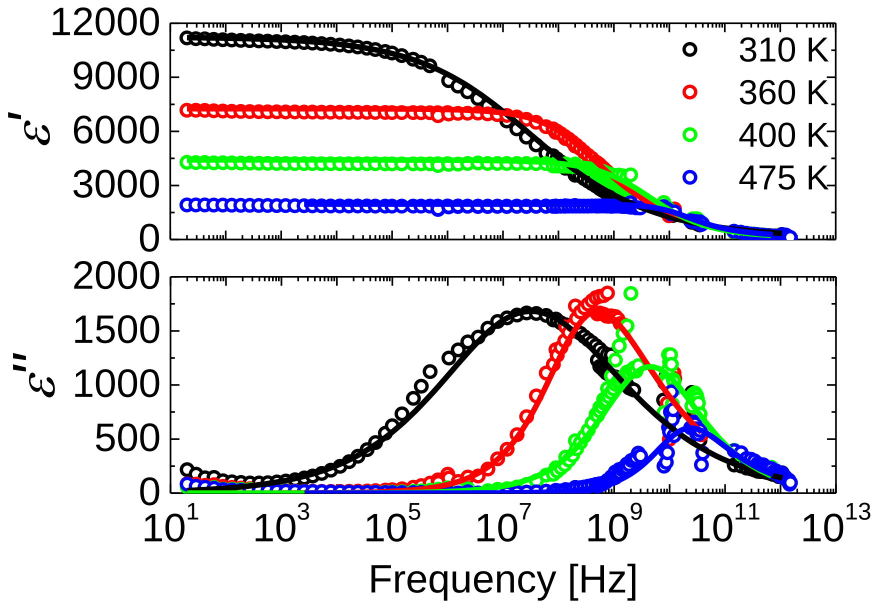

Figure 4.2.17 Frequency dependences of complex dielectric permittivity of 0.2NBT-0.6ST-0.2PT solid solutions at different temperatures.

The dielectric spectra of 0.2NBT-0.6ST-0.2PT are depicted in Figure 4.2.17 (only the data above the phase transition temperature is presented). The same relaxor-like features can be observed in the dielectric spectra. The only difference is that the asymmetry is less pronounced (especially in the vicinity of the phase transition). The dielectric spectra become much broader below the phase transition temperature. Only several curves at different temperatures can be fitted reliably with the empirical models (usually, the Cole-Cole and Havriliak-Negami equations fail to describe broad spectra). There are hints that the relaxation starts hardening (the mean relaxation time starts increasing with the decrease of the temperature) with the decrease of temperature below the phase transition. This feature supposes the order-disorder nature of the phase transition.

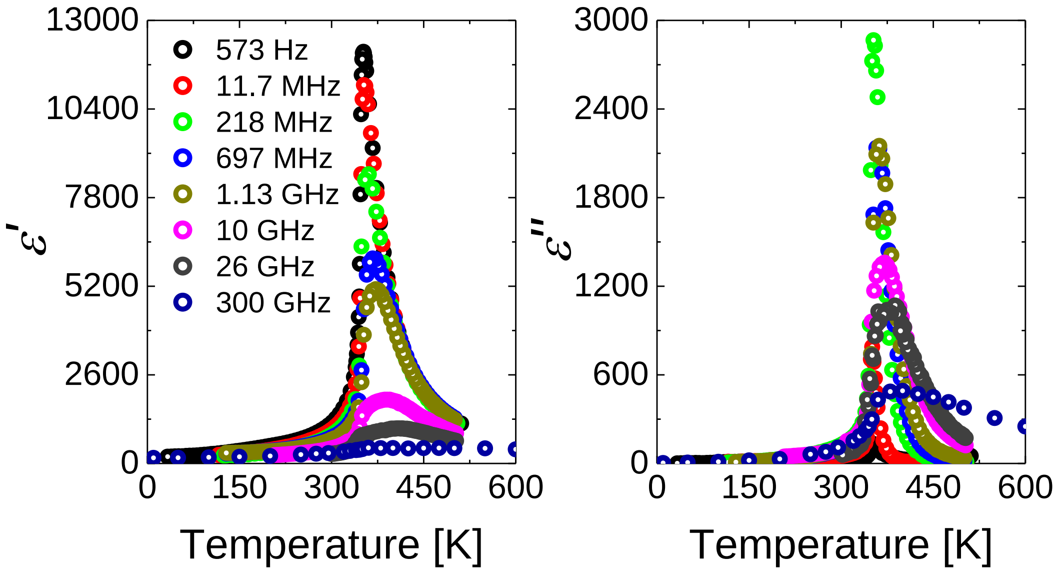

Figure 4.2.18 Temperature dependences of complex dielectric permittivity of 0.1NBT-0.6ST-0.3PT solid solutions.

Further increase of lead titanate concentration up to 30 mol. % shifts the phase transition to higher temperatures. The temperature dependence of the complex dielectric permittivity of 0.1NBT-0.6-ST-0.3PT is depicted in Figure 4.2.18. The first order phase transition can be observed in this graph. A broad dispersion is observed at microwave frequencies above the phase transition temperature *T*c (around 350 K). Such a broad dispersion resembles relaxors, although one important feature is missing in Figure 4.2.18: the shift of permittivity maxima for different frequencies is absent (or negligible) in both the real and the imaginary parts of the dielectric permittivity.

Above the phase transition temperature, deviation from the Curie-Weiss law is observed for the static dielectric permittivity (refer to Figure S6 in APPENDIX II). The temperature variation of dielectric permittivity in the vicinity of its peak is similar to the dependence observed in canonical relaxors[53]. This is contradictory, because one of the most important fingerprints of relaxor ferroelectrics is the shift of the permittivity maximum with temperature. This implies that we cannot ascertain the higher temperature phase to be a relaxor. The deviation from the Curie-Weiss law might be explained by the precursor dynamics[27].

The Terahertz data of dielectric permittivity give a hint that the prevailing contribution to the dielectric permittivity does not stem from the soft ferroelectric phonon. The jump of the permittivity in the vicinity of the phase transition at a frequency of 300 GHz is rather small relative to the dielectric strength of this broad relaxation process. One can expect that the phonon contribution is of the order of 100 and it cannot explain this giant anomaly (see the permittivity measured at 300 GHz, whose temperature dependence is shown in Figure 4.2.18). The contribution to dielectric permittivity mostly comes from the relaxation mode (i. e. central peak). One of the possibilities is that the phase transition is of order-disorder type. The dispersion we observe in the microwave region resembles order-disorder type phase transitions in ferroelectrics.

The dielectric spectra of order-disorder type phase transitions can be well described by the Debye-type relaxation away from the phase transition temperature. Sometimes, the dielectric spectra broaden in the vicinity of the T_c in order-disorder type ferroelectrics. The dielectric spectra of 0.1NBT-0.6ST-0.3PT (Figure 4.2.19) are much broader than the Debye-type relaxation in the whole temperature region.

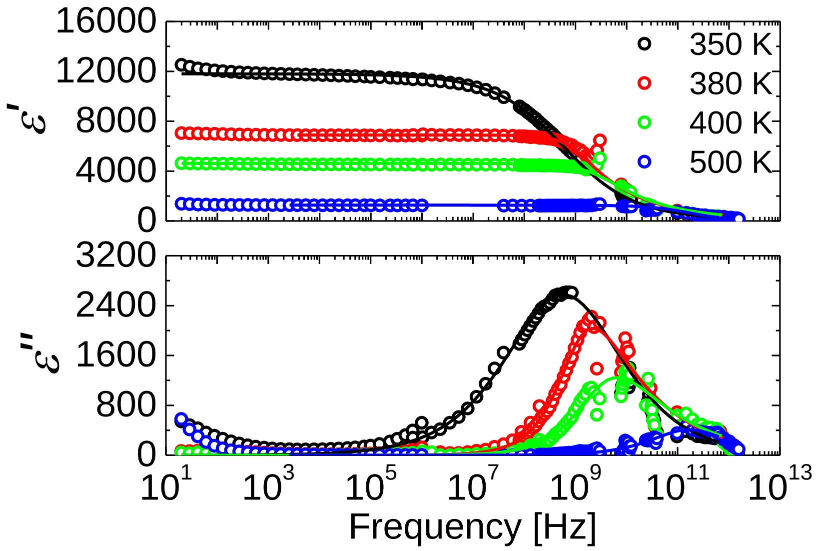

Figure 4.2.19 Frequency dependences of complex dielectric permittivity of 0.1NBT-0.6ST-0.3PT solid solutions at different temperatures.

Purely order-disorder ferroelectric phase transitions in perovskite oxides are usually not observed. It is widely accepted in the ferroelectric community that most perovskite ferroelectrics (such as $BaTiO_3$) exhibit a crossover from displacive to an order-disorder phase transition. Such a behavior is manifested by the coexistence of mutually interacting soft polar phonon and relaxation-type modes, exhibiting a critical slowing down towards T_c[22]. On the other hand, in such compositionally complex solid solutions the anomaly might be related to some other dipolar excitations like polar nanoregions[99].

The results on the dielectric spectra can be summarized by the temperature dependences of mean relaxation time. They are depicted for all the compositions in Figure 4.2.20. The compositions with an absent phase transition show an increase of mean relaxation time with the decrease of temperature. These compositions can be described by the Vogel-Fulcher law. This means that the freezing of polar clusters exist in these relaxor-like systems. The activation energy of the relaxation in 0.3NBT-0.6ST-0.1PT solid solutions (E_a = 0.14 eV) is larger compared to the parental composition (E_a = 0.11 eV). The freezing temperature T_{VF} is higher as well.

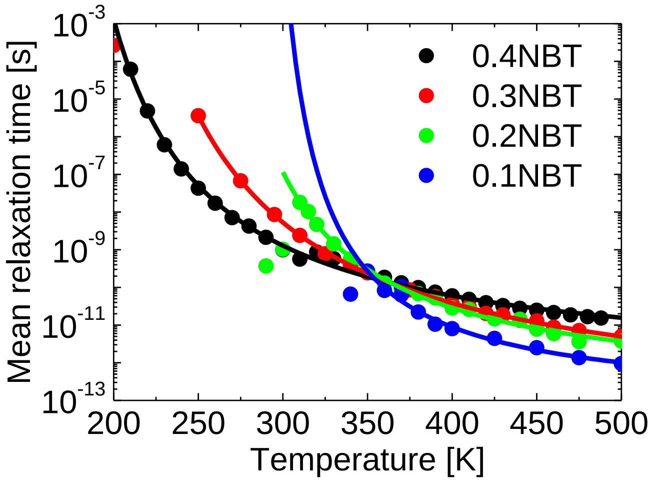

Figure 4.2.20 Temperature dependence of the mean relaxation time in all investigated ceramics. The data on the 0.4NBT-0.6ST solid solutions was taken from the work by Svirskas et al.[117].

The compositions which undergo the spontaneous phase transition have similar behaviour of the mean relaxation time above the transition temperature. The freezing temperature which was obtained is lower than the phase transition temperature in these compositions. This is not uncommon for such highly disordered systems with a spontaneous relaxor to ferroelectric phase transition. So, this result is debatable and barely has a physical meaning (same as in PMN-17PT single crystal). We cannot talk about the freezing of polarization fluctuations below the ferroelectric phase transition. The ferroelectric domains form below the phase transition.

The dielectric spectra were reliably fitted for the 0.2NBT-0.6ST-0.2PT and 0.1NBT-0.6ST-0.3PT compositions even below the phase transition temperature. Unfortunately, the satisfactory curves could only be obtained no more than 20 K below the phase transition. The relaxation hardens below the phase transition temperature. This is a very important experimental fact which might be related to the order-disorder nature of the phase transition. This behaviour is nearly the same as in PMN-17PT single crystals. This feature can be thought as a distinct feature of relaxor-PT solid solutions since similar behaviour has not been observed in other similar disordered systems.

4.2.2.2 Raman and IR spectroscopy

The investigation of lattice dynamics will be concentrated on the Raman spectra. The advantage of Raman data vs. the IR data is that the Raman spectrum is directly related to the imaginary part of permittivity at the given frequency. Furthermore, Raman spectroscopy is more sensitive to the local broken symmetry. It is definitely a sufficient tool to identify the mode softening as well as local structural inhomogeneities. Figure 4.2.21 (a) represents Raman spectra for all compositions at 100 K temperature. This graph illustrates the change of Raman spectra versus the concentration of lead. All the compositions show characteristic Raman spectra for the perovskite oxides.

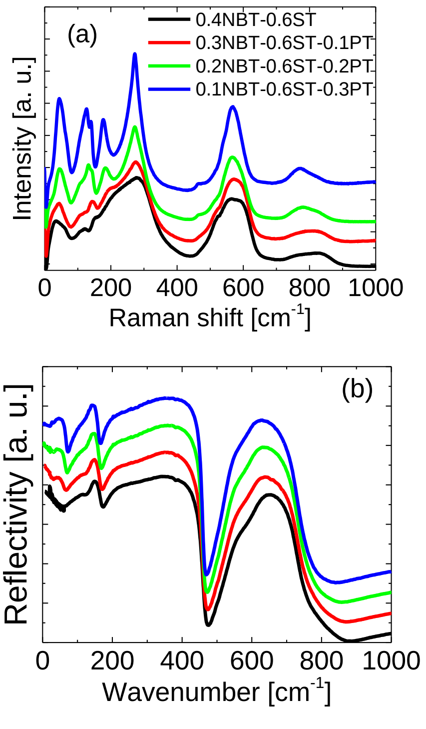

Figure 4.2.21 Comparison of Raman (a) and FTIR (b) spectra for all compositions. Raman spectra are depicted at 100 K temperature. FTIR spectra are depicted at 295 K.

0.4NBT-0.6ST solid solutions have a macroscopic cubic structure. The Raman spectra should be absent but the well-defined vibrational bands can be observed. This is the consequence of broken local symmetry. These Raman bands are quite broad and are often evidenced in complex perovskite oxides.

The addition of lead enhances some of the spectral lines. It is clear that the bands below 400 cm^{-1} develop to sharp, well-defined peaks. The 150 – 400 cm^{-1} band is associated with the Ti-O vibrations. This means that the relaxor compositions have a dynamic disorder of Ti^{4+} ion (local disorder of Ti displacements). The titanium ion can hop in several equivalent positions. This hopping is the reason for the broad spectral line in 150-400 cm^{-1} band. The changes can be observed below 150 cm^{-1} as well. These bands can be associated to A-O vibrations. The number of modes of ferroelectric compositions well correspond to the P4mm symmetry (8 bands can be observed). So, the spectral evolution vs. composition can be explained by the increase of the tetragonal distortions (the structural data is known from the works by M. Dunce et al.[116]).

The IR spectrum of different compositions is depicted in Figure 4.2.21 (b). The increase of lead titanate changes the reflection band below 200 cm^{-1}. The lowest frequency band of 0.4NBT-0.6ST spectrum consists of the relaxation mode (visible up to 100 cm^{-1}). The lowest frequency TO phonon (rather weak one) is around 120 cm^{-1}. This phonon exists in all the compositions. The increase of lead titanate changes the band below 100 cm^{-1} significantly. Another phonon mode emerges which should correspond to the Last mode of the lead titanate (please note that the PMN-17PT has a very similar phonon band which supports this idea). The relaxation mode still exists in the compositions with lead. It is situated below the Last mode. It can only be seen in the THz data (the THz data was recalculated to the reflectivity and depicted in the spectra below 50 cm^{-1}).

The ferroelectric soft mode should be visible in the temperature dependent Raman spectra. Figure 4.2.22 represents the Raman spectra of 0.4NBT-0.6ST and 0.3NBT-0.6ST-0.1PT solid solutions. Raman spectra can be observed in the whole investigated temperature region. The vibrational bands are even active 200 K above the permittivity peak at low frequencies. In both samples the intensity of Raman spectra decrease with the increase of temperature. It seems that the peak positions do not change with temperature.

They only get broader which indicates the increase of the disorder in the lattice. Such behaviour indicates the dynamic disorder in the perovskite lattice.

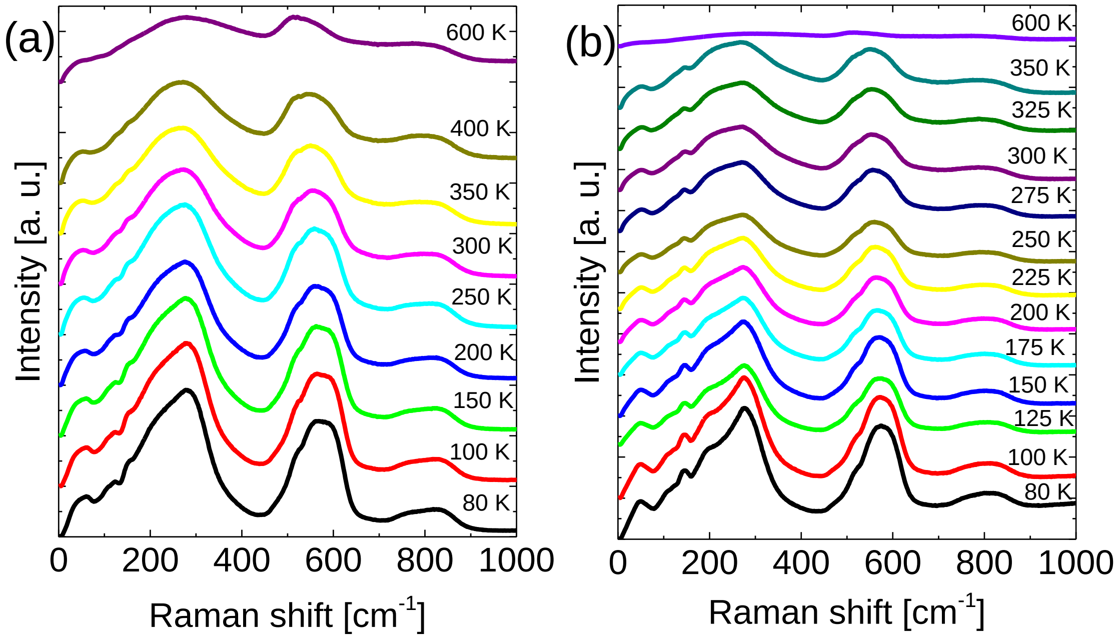

Figure 4.2.22 Temperature dependent Raman spectra of 0.4NBT-0.6ST solid solutions (a) and 0.3NBT-0.6ST-0.1PT solid solutions (b).

The 0.3NBT-0.6ST-0.1PT solid solutions have sharper peaks at low temperatures but they tend to get broader with the increase of temperature. It indicates stronger ordering and the growth of polar clusters and/or correlation length. No softening can be identified from such a broad peaks. It is possible to conclude that the broad dielectric relaxation is a cooperative motion of polar clusters in 0.4NBT-0.6ST and 0.3NBT-0.6ST-0.1PT solid solutions. This can be clarified from the temperature dependences of mode frequencies (Figure 4.2.23). The graph reveals that all the modes have only negligible temperature dependence of frequency. The damping increases with an increase of temperature for some of the modes but this is common phonon behaviour. The intensity gradually decreases with an increase of the temperature. This shows that local symmetry breaking disappears. It becomes more and more cubic with an increase of temperature.

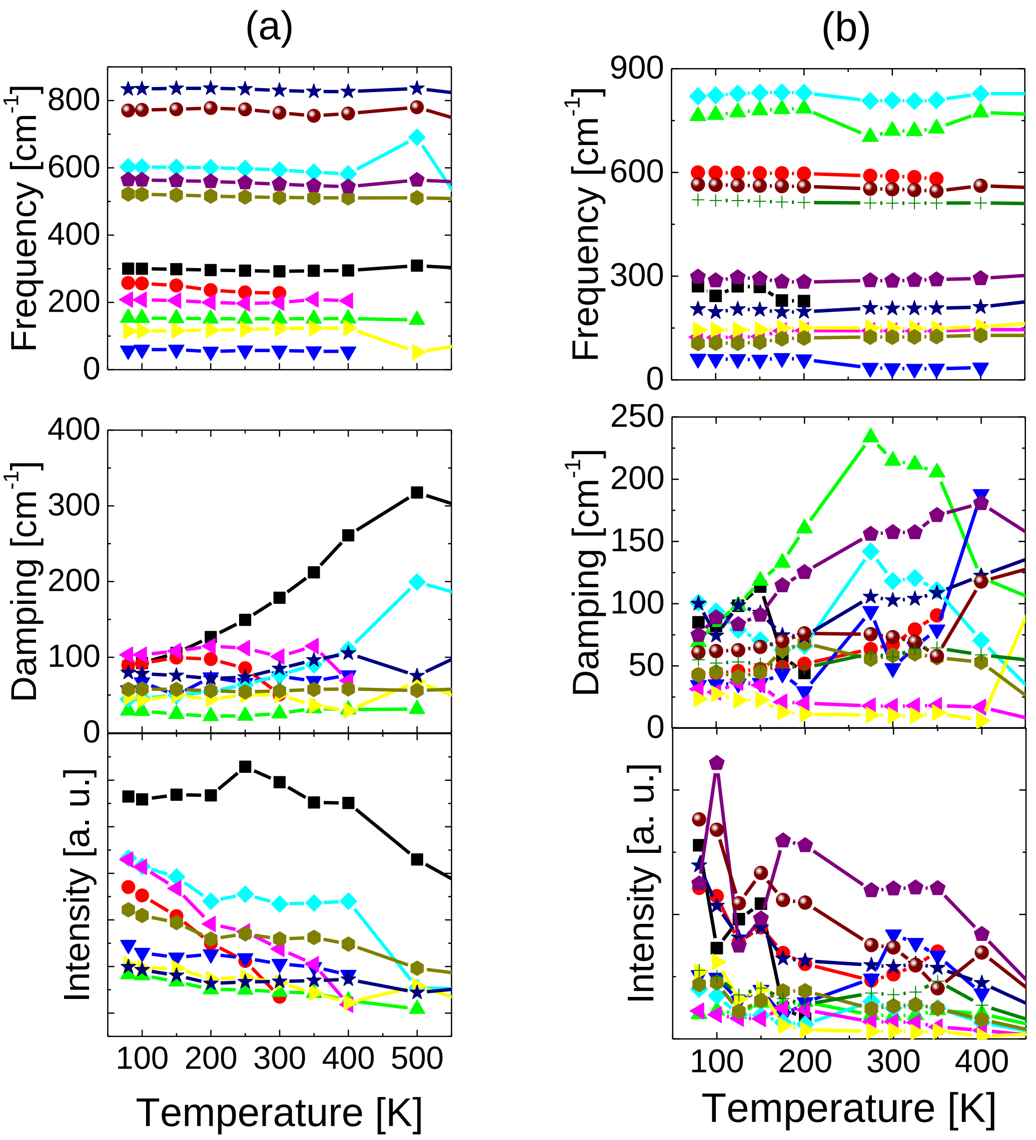

Figure 4.2.23 Temperature dependence of fitting parameters for 0.4NBT-0.6ST (a) and 0.3NBT-0.6ST-0.1PT (b) solid solutions. Top panel represents the mode frequencies; middle panel represents the damping of the mode; bottom panel represents the intensity of the mode.

Figure 4.2.24 represents the Raman spectra of 0.2NBT-0.6ST-0.2PT and 0.1NBT-0.6ST-0.3PT solid solutions. These two compositions have much sharper spectral lines. The main differences are related to the spectral bands below 400 cm^{-1}. The peak at 300 cm^{-1} is much sharper. The intensity of this peak decreases with the increase of temperature but it persists in both compositions even above the phase transition temperature. Together with the decrease of the 300 cm^{-1} peak another broad line develops in the 200 – 300 cm^{-1} range. This development resembles the case of pure strontium titanate[198]. It was associated to the antiferrodistortive phase transition of strontium titanate at 105 K. It hints that the tetragonal distortions develop further with an increase of temperature (note the APPENDIX II which shows that the tetragonality factor is quite low at room temperature). The development of sharp peaks might be related to another structural transformation. Unfortunately, there are no structural data below the room temperature. These huge changes also give some contribution to the dielectric permittivity. It might explain the low temperature ferroelectric dispersions in similar systems[117,197] (such dispersion is evident in the current system as well).

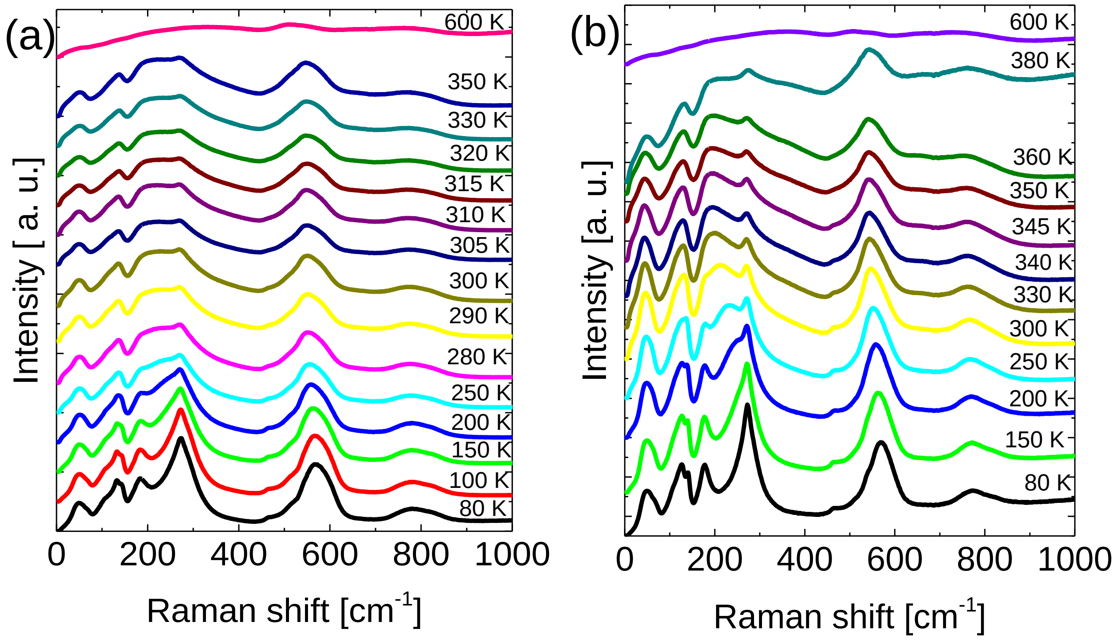

Figure 4.2.24 Temperature dependent Raman spectra of 0.2NBT-0.6ST-0.2PT solid solutions (a) and 0.1NBT-0.6ST-0.3PT solid solutions (b).

Finally, the bands below 200 cm^{-1} can be well distinguished in these two compositions. They are much more intense than in the spectra of lower PT compositions. All the features can well be distinguished at the lowest temperatures. These vibrations can be associated with different A-O bonds (A-site occupied by 4 different ions). It is evident that due to the addition of lead ions the ferroelectric order increases and the A-O vibrations become well defined. The significant softening on the other hand cannot be observed in any of the bands. Only the intensity decreases with an increase of temperature. The

Raman spectra still can be detectable 250 K above the transition temperature. This indicates presence of local polar distortions and dynamic disorder (deviation from the macroscopic cubic symmetry). The temperature dependence of mode frequencies of 0.2NBT-0.6ST-0.2PT and 0.1NBT-0.6ST-0.3PT solid solutions is depicted in Figure 4.2.25.

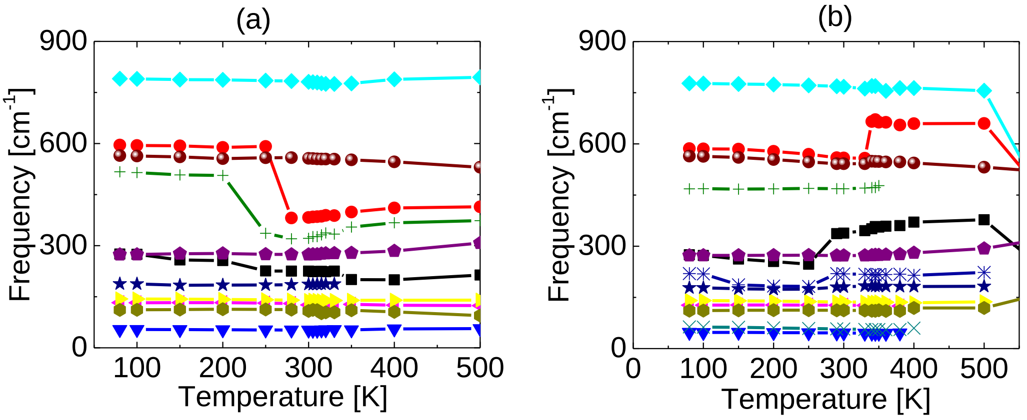

Figure 4.2.25 Temperature dependence of mode frequencies in 0.2NBT-0.6ST-0.2PT (a) and 0.1NBT-0.6ST-0.3PT (b)

The temperature dependences of IR spectra of 0.4NBT-0.6ST and 0.1NBT-0.6ST-0.3PT solid solutions are depicted in Figure 4.2.26. The MIR data (> 550 cm^{-1}) is only depicted at room temperature since that band does not show any temperature changes and is irrelevant for the discussion. Also, only the boundary compositions of (0.4-*y*)NBT-0.6ST-*y*PT system is depicted. The middle ones have similar behaviour and do not provide any additional information about the phonon behaviour.

The phonon spectra of 0.4NBT-0.6ST do not change with temperature. The only difference is below 100 cm^{-1}. This is related to the relaxation which emerges to higher frequencies when the temperature is increase. The relaxation is nearly absent at 10 K. The room temperature spectra show significant increase of reflectivity with the decrease of frequency (this is indication of the relaxation).

Similar evolution of IR spectrum is observed in 0.1NBT-0.6ST-0.3PT. The relaxation mode is absent at 10 K spectra. Here it is possible to observe only the low frequency phonon (around 50 cm^{-1}). The relaxation gradually evolves with an increase of temperature. The largest evolution is observed in the vicinity of the phase transition temperature. The lowest frequency mode overlaps with the relaxation above the phase transition temperature. It might be related to the increase of damping of this TO phonon. It is difficult to distinguish the frequency of this mode but it does not soften. This behaviour is very similar to the PMN-17PT single crystal. The nature of the phase transition is quite similar.

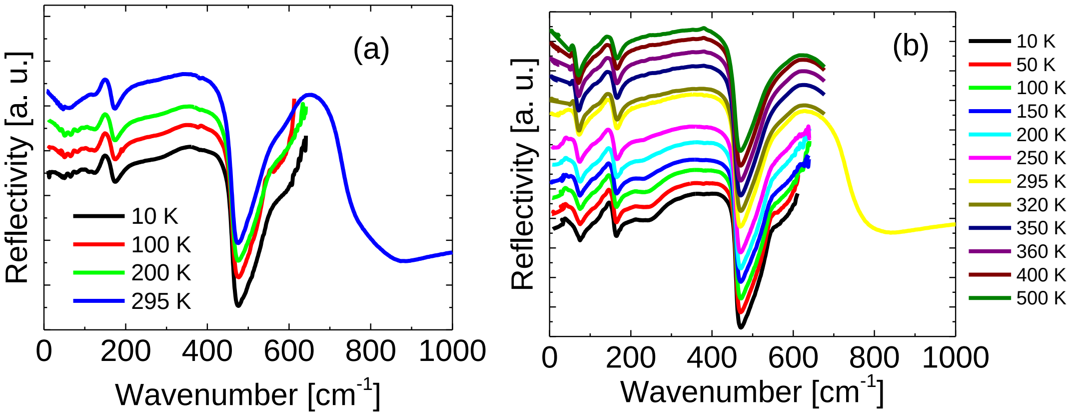

Figure 4.2.26 Temperature evolution of FTIR spectra in 0.4NBT-0.6ST (a) and 0.1NBT-0.6ST-0.3PT (b) solid solutions.

All the compositions with non-zero content of PT have another significant change in the phonon spectrum. The 200 – 400 cm^{-1} band splits (around 250 cm^{-1}). There are several interesting facts about this change in the spectra. Firstly, it occurs at quite low temperatures (below 200 K). There are no indications of structural changes in other experiments. Secondly, these changes are much more obvious for higher PT content ($y = 0.1$ composition has a very weak change but in the spectra of $y = 0.2$ and $y = 0.3$ the change is obvious). Finally, the change of spectra is also observed in Raman spectra. This indicates the non-centrosymetric nature of this band. It might be related to the second order processes of strontium titanate. It is well known that the Raman spectra of strontium titanate are due to the second order processes above the antiferrodistortive phase transition. This is one of the most peculiar properties which can be observed in the lattice dynamics of the NBT-ST-PT system. Unfortunately, without the low temperature structural data it is difficult to draw unambiguous conclusions.

Raman and IR spectra revealed that the (0.4-*y*)NBT-0.6ST-*y*PT solid solutions have common features to PMN-17PT single crystal. It is evident that the phonon softening has no impact to the phase transition and the dielectric anomalies in this system. These anomalies are determined by the ordering and percolation of polar clusters which gradually transform to the ferroelectric (nano)domains. It might be considered as a system with order-disorder character rather than displacive one. The only changes in phonon frequencies can be associated with non-ferroelectric changes of the lattice (or maybe strong anharmonicity).

4.2.2.3 Pyroelectric Properties

The temperature dependences of polarization and pyroelectric coefficient of (0.4-*y*)NBT-0.6ST-*y*PT and 0.4NBT-(0.6-*x*)ST-*x*PT solid solutions are depicted in Figure 4.2.27 and Figure 4.2.28 respectively.

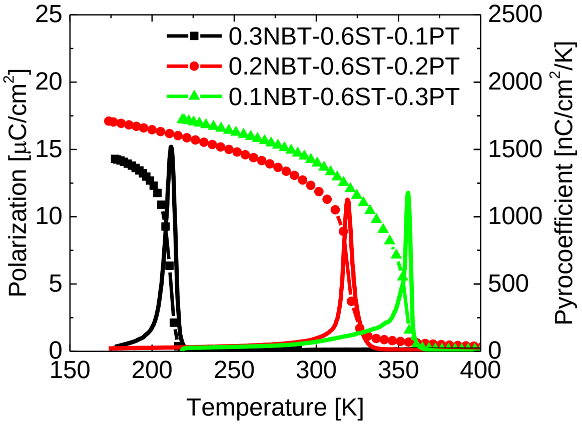

Figure 4.2.27 Temperature dependence of spontaneous polarization and pyroelectric coefficient in (0.4-*y*)NBT-0.6ST-*y*PT solid solutions.

The temperature dependences of remanent polarization in (0.4-*y*)NBT-0.6ST-*y*PT solid solutions show strong 1st order character of phase transition. It is evident that the $y = 0.1$ composition which has the stable ferroelectric phase only after applying an external electric field at a certain temperature has the most abrupt polarization jump. The peak value of pyrocoefficient is largest for this composition. The increase of lead titanate decreases the peak value. Another important feature is the less abrupt jump of polarization in higher lead content compositions. The polarization evolution vs. temperature in 0.1NBT-0.6ST-0.3PT resembles the 2nd order phase transition. It seems that the polarization decreases smoothly until it gradually reaches zero. This is a quite contradictory to the dielectric data which clearly revealed the 1st order character of the phase transition. The polarization gradually decreases in y = 0.2; 0.3 compositions. The remnant polarization is non zero even above the phase transition temperature which was obtained by XRD measurements (or even higher than the temperature of permittivity peak at low frequencies). This is a clear evidence of the polarization persisting above the phase transition temperature. The lead titanate introduces some clusters with a very stable polarization which can contribute to the pyrocurrent even above the phase transition temperature.

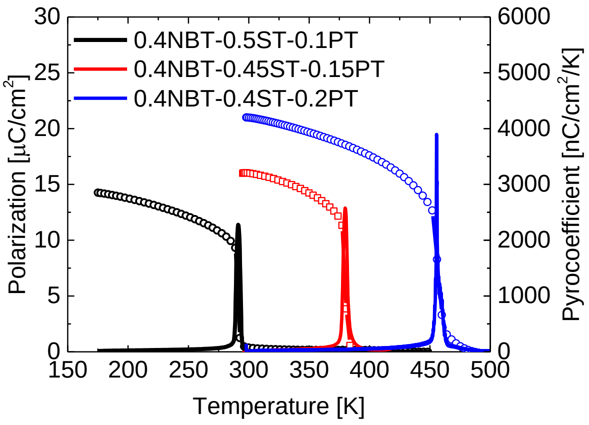

Figure 4.2.28 Temperature dependence of spontaneous polarization and pyroelectric coefficient in 0.4NBT-(0.6-x)ST-xPT solid solutions.

A different scenario is in 0.4NBT-(0.6-x)ST-xPT solid solutions. The low PT ($x < 0.1$) compositions which are not depicted in Figure 4.2.28 cannot be poled thus their pyroelectric response is very weak and can be neglected. All three compositions which are ferroelectric show a very strong 1st order phase transition character. The abrupt jump of polarization is much more evident relative to the (0.4-y)NBT-0.6ST-yPT system. The 1st order character increases with an increase of lead concentration. The saturation polarization values are larger in this system. This can be easily explained by the increase of ferroelectric distortion in 0.4NBT-(0.6-x)ST-xPT. Lead in the strontium site increases the tetragonal distortion significantly and thus the 1st order character is enhanced. Due to this stronger 1st order character, the pyroelectric properties are larger than in (0.4-y)NBT-0.6ST-yPT system. Furthermore, it seems that the polarization barely persists above the phase transition temperature.

This proves that the distortions induced by the bismuth and lead ions are complementary. It can be exploited for the enhancement of internal stresses which should improve the electromechanical/pyroelectric properties.

4.2.2.4 Electromechanical properties

The extensive studies of the electromechanical response will be provided for 0.4NBT-(0.6-x)ST-xPT and 0.4NBT-(0.6-x)ST-xPT solid solutions. This will help to understand how the structural complexity affects the piezoelectric response. The role of domain walls and their contribution to electromechanical properties will be extracted. The electromechanical investigation will be concentrated on the 0.4NBT-(0.6-x)ST-xPT system since the characteristic temperature regions of the anomalies are more convenient. Afterwards the results will be generalized for both systems.

Both of these systems can be divided in several different concentration ranges depending on the stability of the ferroelectric and/or relaxor phase. The different origin of the electromechanical response is observed in different concentration ranges:

i) low PT concentration region (x up to 0.05; y up to 0.1) which exhibits relaxor-like properties in the whole temperature range and in which long-range ferroelectric order could not be induced by even a moderate electric field[116];

ii) Intermediate PT concentration range ($0.05 < x < 0.15$; $y = 0.1$) where it is possible to induce ferroelectric phase with an external electric field. The representative composition $x = 0.10$ has a stable ferroelectric phase at temperatures below $T_t = 290$ K even after removing the external electric field.

iii) High PT concentration range ($x \geq 0.15$; $y \geq 0.2$) where spontaneous 1st order phase transition between relaxor and normal ferroelectric state occurs. The ferroelectric order in this concentration range persists up to temperature T_t on heating. This temperature is located below the permittivity maximum temperature T_m. The difference between T_m and T_t decreases upon the increase of x and y.

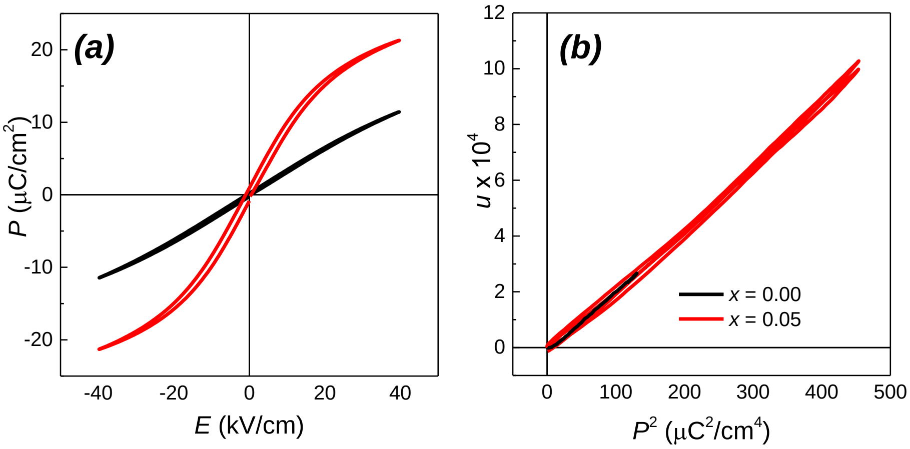

Figure 4.2.29 Polarization as a function of the electric field $P(E)$ for 0.4NBT-(0.6-x)ST-xPT compositions with x = 0.00 and x = 0.05 measured at room temperature (a) and strain as a function of polarization square u(P^2) corresponding to the same $P(E)$ loops (b).

In the low PT concentration region, polarization as a function of the electric field is weakly nonlinear for the composition with $x = 0.00$ and has an expressed trend to saturate for the composition with $x = 0.05$ (Figure 4.2.29 (a)). The latter indicates approaching the intermediate PT concentration range where the ferroelectric state can be induced by a moderate electric field. In spite of different $P(E)$ character when comparing the compositions with $x = 0.00$ and $x = 0.05$, strain as a function of polarization square P^2 is linear according to Eq. 3.4.5 or close to linear in both cases (Figure 4.2.29 (b)). The same trends are observed in the whole temperature range that was investigated, thus the temperature dependences of loops are not presented here.

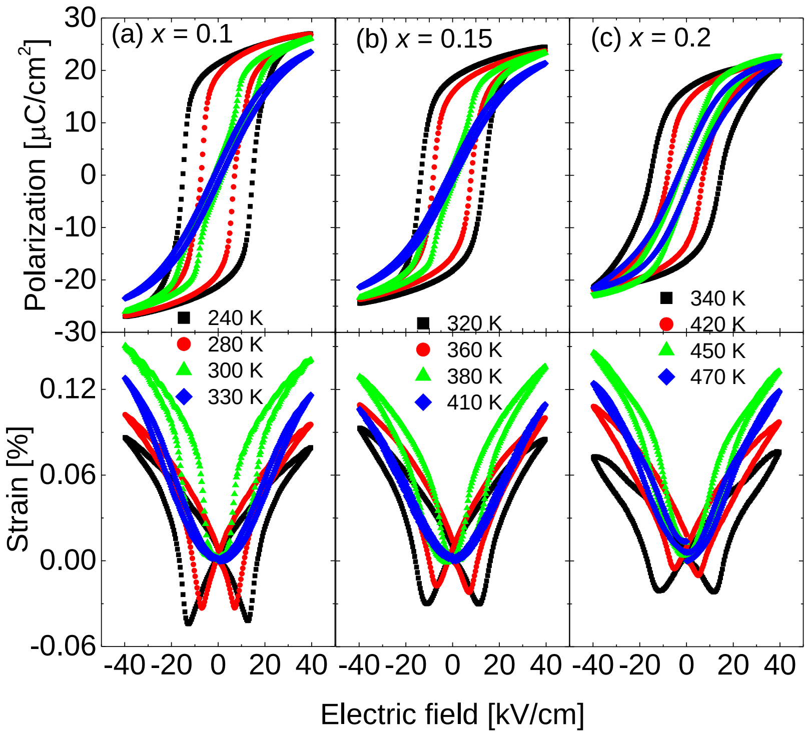

Figure 4.2.30 Temperature evolution of polarization and strain hysteresis loops in 0.4NBT-(0.6-*x*)ST-*x*PT solid solutoins. Top panel: polarization vs. electric field; bottom panel: strain vs. electric field.

The temperature evolution of polarization and deformation hysteresis loops of compositions with $x \geq 0.10$ is presented in Figure 4.2.30. All compositions exhibit well expressed ferroelectric loops. The double hysteresis loops in the temperature region slightly above the phase transition temperature reflect the reversible field induced phase transition between ferroelectric and relaxor states[116,119] (green $P(E)$ curves in Figure 4.2.30 (a) and (b)). The temperature evolution of strain hysteresis loops shows the change of electromechanical behaviour from piezoelectric to electrostrictive. The green curves correspond to double hysteresis loops in Figure 4.2.30 (a) and reflect a phase transition between the relaxor and ferroelectric state. The blue curves represent purely electrostrictive behaviour in all three compositions (i. e. the strain is proportional to the square of the polarization, like in Figure 4.2.29 (b)).

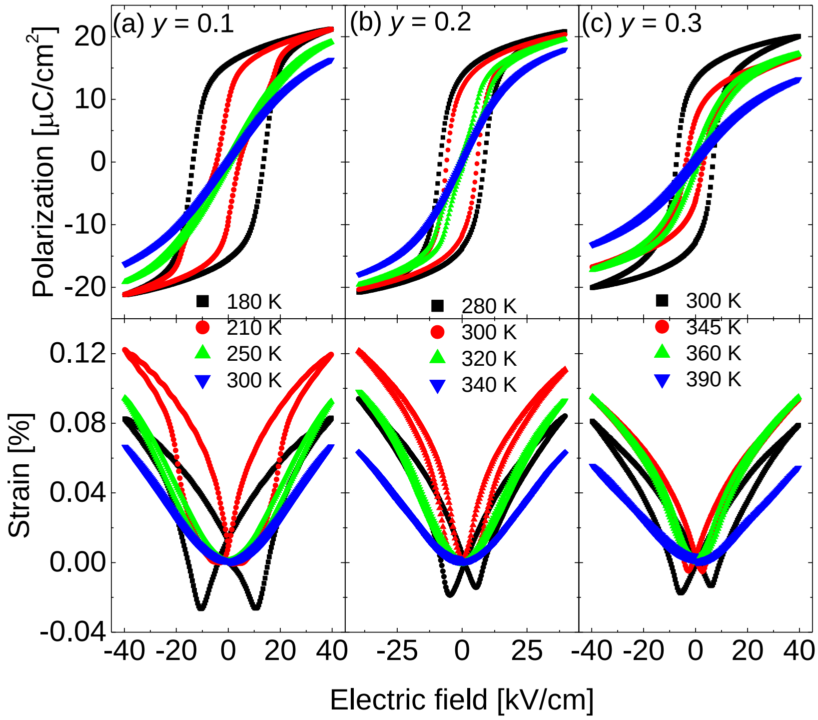

Figure 4.2.31 Temperature evolution of polarization and strain hysteresis loops in (0.4-*y*)NBT-0.6ST-*y*PT solid solutions. Top panel: polarization vs. electric field; bottom panel: strain vs. electric field.

The similar trends in polarization and strain hysteresis loops can be observed in (0.4-*y*)NBT-0.6ST-*y*PT system (Figure 4.2.31). 0.3NBT-0.6ST-0.1PT solid solutions exhibit same features as the other 0.1PT composition. There are only some quantitative differences. The dielectric anomaly in 0.3NBT-0.6ST-0.1PT solid solutions is at lower temperature compared to 0.4NBT-0.5ST-0.1PT. The significant difference between these compositions is the temperature T_t. It is much lower in 0.3NBT-0.6ST-0.1PT solid solutions. The difference between the permittivity peak temperature at a given frequency is also larger in aforementioned composition. Both of these compositions do not show a spontaneous nucleation of ferroelectric domains. This indicates that the cubic structure persists in the investigated temperature region. The ferroelectric order can only be induced by an external electric field.

The higher PT compositions show much stronger relaxor behaviour above the phase transition temperature (from the point of dielectric spectroscopy). The strain hysteresis is not so evident in the region of the *E*-

field induced phase transition. It seems that the hysteretic behaviour is due to the strong 1st order nature of the field induced phase transition (it is even evident from the pyroelectric measurements). The electric field induced phase transition is only visible in a quite narrow temperature region for the 0.4NBT-0.6ST-0.3PT composition. It is a very weak phenomenon and the characteristic inclination of polarization hysteresis (the most obviously seen in the red curve of Figure 4.2.31 (a)) indicating the field induced phase transition can hardly be seen. It was already mentioned that this composition does not resemble the relaxor behaviour. This is also evident from the characteristic hysteresis loops.

Both Figure 4.2.30 and Figure 4.2.31 clearly revealed that the addition of lead to the parental composition affect the electromechanical behaviour and polarization hysteresis in the same manner. Onwards, the explanation of the nature of electromechanical behaviour in these systems will be focussed on the 0.4NBT-(0.6-x)ST-xPT system since the anomalies are situated in much more convenient temperature range (in the very vicinity or above room temperature). This helps getting more accuarate results at the lowest field regime.

The chemical complexity of these solid solutions should give a very complex electromechanical response. The detailed studies of the strain vs. different amplitudes of applied electric field should reveal the nature of electromechanical response and the contribution of domain walls and nonlinearities to the electromechanical activity. It will also help to identify the electromechanical properties in the vicinity of the E-field induced phase transition. Thus the detailed studies of the temperature dependent electromechanical response will be presented for the compositions with $x \geq 0.1$.

The intermediate PT concentration range (i. e. composition with $x = 0.10$) demonstrates similar behavior to the low concentration compositions at temperatures above $T_t = 290$ K. Strain as a function of polarization in the relaxor state can be described by Eq. 3.4.5 with a similar value of Q_{11} (Table 4.2). Below T_t, the electric field-induced ferroelectric state persists after electric field is turned off. Thus, it is more appropriate to discuss the temperature range

$T < T_t$ of the compositions with $0.05 < x < 0.15$ (i.e. with $x = 0.10$) together with the ferroelectric state of compositions with $x \geq 0.15$.

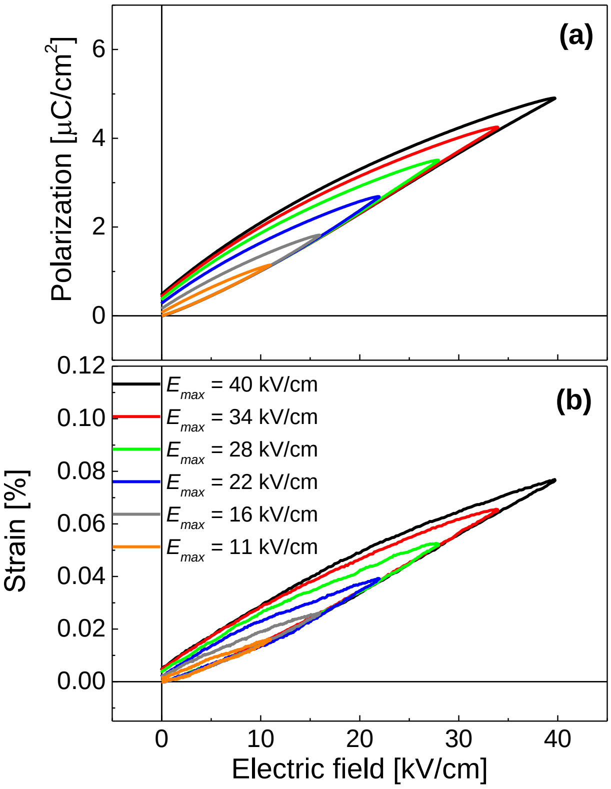

Figure 4.2.32 Polarization as a function of the electric field $P(E)$ (a) and strain as a function of electric field $u(E)$ (b) for unipolar electric field pulses of various amplitudes $E_{\max}$ for the composition $x = 0.15$ at 300 K.

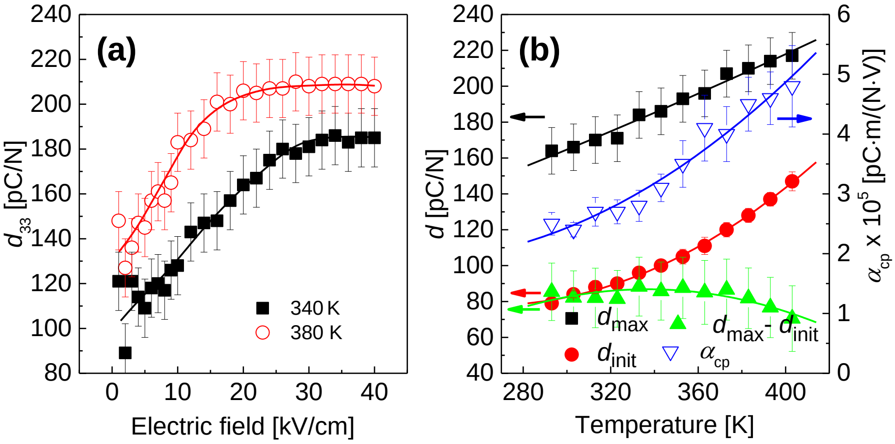

Figure 4.2.33 Piezoelectric coefficient as a function of the electric field amplitude $d_{33}(E_{\max})$ for the composition x = 0.20 at 340 K and at 380 K (a), as well as temperature dependence of parameters d_{init}, α_{cp} and d_{max} (b) evaluated from the Rayleigh law.

The strain response to unipolar electric field pulses of various amplitudes E_{max} was measured in the ferroelectric phase for $x \geq 0.1$ to obtain the piezoelectric coefficient d_{33}. $P(E)$ and $u(E)$ dependences are depicted for the composition $x = 0.15$ at 300 K as an example (Figure 4.2.32). Hysteresis is clearly seen in the $u(E)$ as a functions of the electric field amplitude E_{max}. Such a situation is well known in the research of piezoelectricity in ferroelectrics. It is frequently characterized by the Rayleigh law, which can be applied to describe the hysteresis of either polarization or strain[199]:

$$\begin{gathered} P = \varepsilon_0\Big(\big[\varepsilon_{\mathrm{r}}'(0) + \alpha E_{\mathrm{max}}\big]E \pm \tfrac{\alpha}{2}\big[E_{\mathrm{max}}^2 - E^2\big]\Big) \\ u = \big(d_{\mathrm{init}} + \alpha_{\mathrm{cp}} E_{\mathrm{max}}\big)E \pm \frac{\alpha_{\mathrm{cp}}}{2}\big(E_{\mathrm{max}}^2 - E^2\big), \end{gathered} \tag{4.2.3}$$

Where ε_r' and ε_0 are weak-field dielectric permittivity and vacuum dielectric permittivity, respectively, d_{init} is the reversible part of piezoelectric coefficient d_{33}, α and α_{cp} are the Rayleigh coefficients. The $u(E)$ hysteresis described by Eq. 4.2.3 represents the linear dependence of $d_{33}(E_{\mathrm{max}})$[199]:

$$d_{33}(E_{max}) = d_{init} + \alpha_{cp} E_{max} \tag{4.2.4}$$

The unipolar electric field pulses were applied in the present case so Eq. 4.2.3 cannot be applied to describe $P(E)$ and $u(E)$ hysteresis, only Eq. 4.2.4 can be examined. The measured quasistatic dependence of $u(E)$ at low E_{max} is quite noisy, nevertheless $u(E_{\mathrm{max}})$ can be extrapolated by using a linear dependence according to Eq. 4.2.2. $d_{33}(E_{\mathrm{max}})$ curve approaches saturation at a higher electric field which is better pronounced at higher temperatures (Figure 4.2.33 (a)). The value of d_{33} extrapolated to $E_{\mathrm{max}} = 0$ and denoted as d_{init}, besides the purely intrinsic value of d_{33}, can also contain some contribution from the reversible domain wall motion. Both d_{init} and the maximal value of $d_{33}(E_{\mathrm{max}})$, further denoted as d_{max}, increase if the temperature is increased (Figure 4.2.33 (b)). Therefore $d_{33}(E_{\mathrm{max}})$ is characterized in terms of d_{init}, α_{cp} and d_{max} according to Eq. 4.2.4. According to Hall[199], d_{init} corresponds to the intrinsic piezoelectric effect, which is proportional to dielectric permittivity[3]. So the increase of $d_{\mathrm{init}}(T)$ reflects the increase of dielectric permittivity upon approaching the phase transition temperature T_{c}. The increase of parameter $\alpha_{cp}(T)$ reflects the increasing distance of irreversible domain wall motion at the same electric field value. From such a point of view, it is remarkable that a threshold electric field value exists, above which $d_{33}(E)$ saturates and the total irreversible contribution ($d_{\max}$ - d_{init}) does not increase with temperature (Figure 4.2.33 (b)).

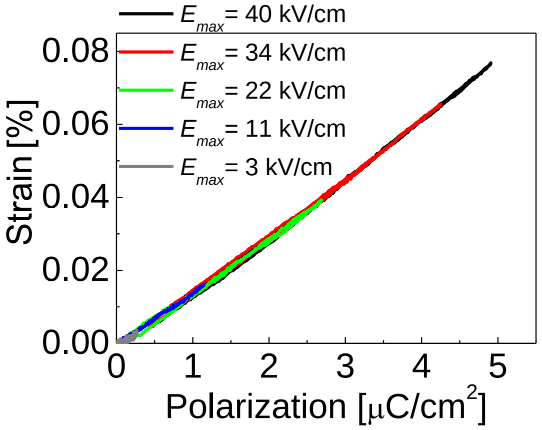

Figure 4.2.34 Strain as a function of polarizations $u(P)$ in 0.4NBT-0.45ST-0.15PT solid solutions at 300 K. Different curves represent the different amplitude of applied electric field $E_{\max}$.

Contrary to $u(E)$, $u(P)$ dependence is almost linear and shows no hysteresis (see Figure 4.2.34). $g_{33}=u/P_{\max}$ in a ferroelectric phase (Figure 4.2.35) is independent of $P_{\max}$ ($P_{\max}$ corresponds to various $E_{\max}$ that were chosen in the experiment), reflecting linear behavior of strain as a function of polarization. Furthermore, g_{33} rather weakly depends on temperature. Only upon approaching the temperature T_t, $g_{33}(P_{\max})$ has a weak trend to increase, while $g_{33}(P_{\max}$ = const.) as a function of temperature decreases (Figure 4.2.35 (b)). It is a rather surprising result considering the complex nature of polarization. The polarization should contain contributions from different types of domain walls as well as the induced polarization. Thus, the hysteresis and the nonlinearity of the electric field-induced strain are related to the electric field dependence of polarization (i. e. the nonlinearities observed in $u(E)$ is due to hysteresis and nonlinear behavior inherent to $P(E)$).

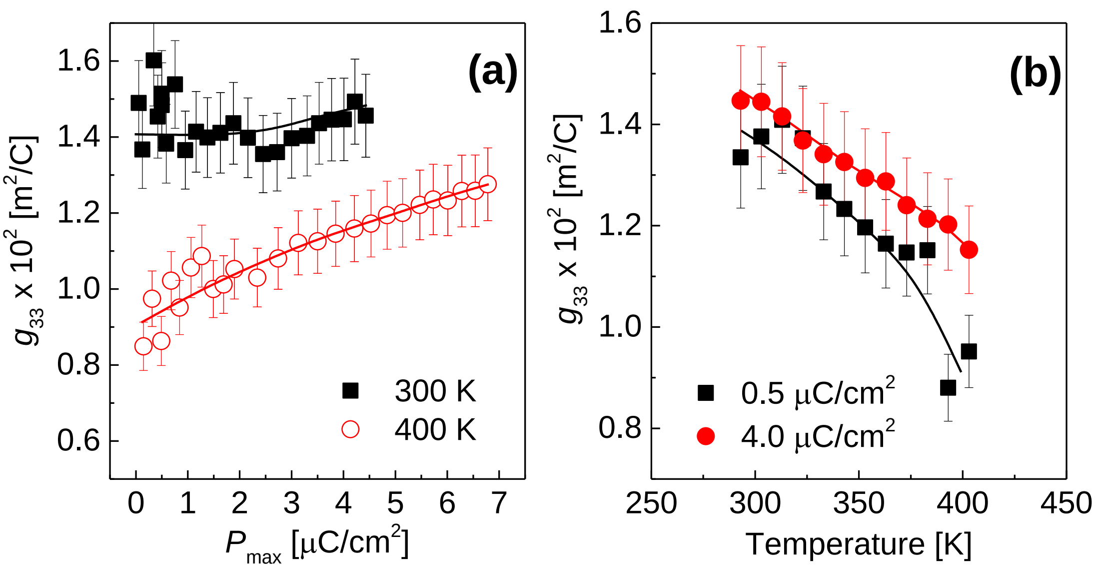

Figure 4.2.35 Piezoelectric coefficient as a function of maximal polarization $g_{33}(P_{max})$ at 300 K and at 400 K (a), as well as $g_{33}(P_{max}=0.5\ \mu C/cm^2)$ and $g_{33}(Pmax = 4.0\ \mu C/cm^2)$ as function of temperature for the composition with x = 0.20 (b).

Such a character of the electric field-induced strain could be expected if $P(E)$ is dominated by the contribution of induced polarization and the piezoelectric effect arises due to the electrostriction. Due to the fact that P_s decreases upon approaching T_t, such a mechanism could also explain the decrease of g_{33} in the same temperature range. Unfortunately, verification of this interpretation is not trivial. It is necessary to have the full data of permittivity and electrostriction tensors to derive the piezoelectric coefficients and in the case of polycrystalline samples it is a difficult task.

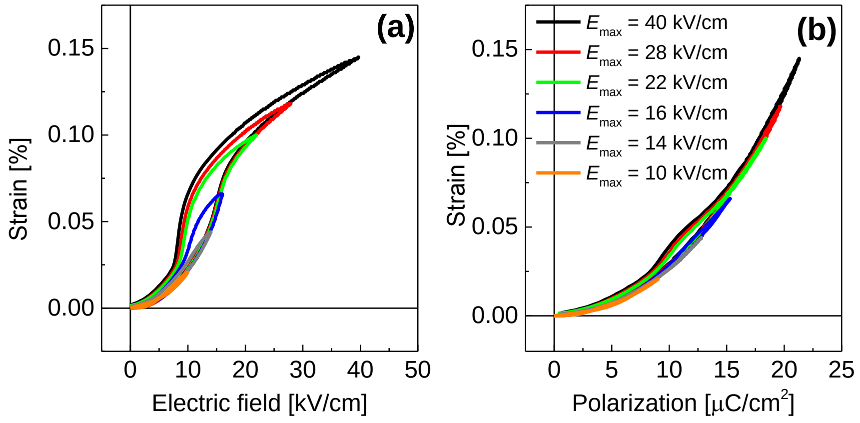

Figure 4.2.36 Strain as a function of the electric field $u(E)$ (a) and as a function of polarization $u(P)$ (b) for the composition with $x = 0.10$ at 300 K at various E_{max}.

Finally, the properties of the electric field-induced strain at the field induced 1st order phase transition are analyzed. The representative composition is $x = 0.10$. Both $P(E)$ and $u(E)$ show a jump with significant hysteresis in the vicinity of the phase transition (see Figure 4.2.36). Strain vs. polarization $u(P)$ has a smooth nonlinear dependence with almost no hysteresis. There is only a small bump in the region of the electric field-induced phase transition from the nonpolar to the ferroelectric state. The description of $u(P)$ according to Eq. 3.4.5 fails in the whole P range, because it is necessary to introduce different electrostriction coefficients in the electric field regions corresponding to the nonpolar and the ferroelectric phases. Q_{11}, obtained in the $E_{\mathrm{max}} < E_{\mathrm{c}}$ electric field region, can be related to Q_{11} in the temperature region where the relaxor state persists in all of the electric field range (Table 4.2). Q_{11}, extracted from $u(P^2)$ at $E_{\mathrm{max}} > E_{\mathrm{c}}$, is approximately 20 % higher. This difference perhaps reflects the difference between mechanisms of $P(E)$ in the ferroelectric and in the nonpolar state. Since there is no additional contribution in $u(P)$ in all of the range of P, the electric field-induced phase transition, in terms of strain, has electrostrictive character.

Table 4.2 Electromechanical coefficients of 0.4NBT-(0.6-*x*)ST-*x*PT and (0.4-*y*)NBT-0.6ST-*y*PT solid solutions. All the data are presented at room temperature except the one with the asterisk.

PT content	$Q_{11}\cdot 10^2$ (m^4/C^2)	d_{init} (pC/N)	d_{max} (pC/N)	$g_{33}\cdot 10^2$ (m^2/C)
0.00	2.2 ± 0.1			
x =0.05	2.3 ± 0.1			
x = 0.10	2.3 ± 0.1*	135 ± 3*	190 ± 10*	1.5 ± 0.1*
x = 0.15		80 ± 3	170 ± 10	1.2 ± 0.1*
x = 0.20		82 ± 3	160 ± 10	1.4 ± 0.1
y = 0.1	2.1 ± 0.1		170 ± 10	1.1 ± 0.1*
y = 0.2	2.1 ± 0.1*	80 ± 10	230 ± 10	1 ± 0.1
y = 0.3	2.4 ± 0.1*	80 ± 10	200 ± 10	1.1 ± 0.1
PMN-17PT	2.2 ± 0.1*		750 ± 10	2.4 ± 0.1

The summary of the electromechanical constants are represented in the Table 4.2. Most of the values are represented at room temperature. The asterisk near the constant indicates that it is not a room temperature value. Some of the compositions have different state at room temperature and that constant cannot be determined. The data on PMN-17PT is also presented for the comparison.

The electrostriction coefficient Q_{11} is concentration independent in both systems. This is a trend which is often observed in many relaxor ferroelectric systems. The electrostriction coefficient in PMN-17PT also has the same value. Similar values were reported for the PMN-10PT[200]. It seems that this is a common feature for relaxors and relaxor-PT solid solution systems. Ba-based ferroelectrics show larger electrostrictive coefficients[201,202]. The high PT composition, namely $y = 0.3$, shows larger Q_{11} but one has to note that it was measured at 400 K temperature. The electrostriction coefficient is often found to be temperature independent[203,204]. Although, some data show weak temperature dependence of electrostriction[200].

This kind of temperature dependence would explain the larger Q_{11} in the 0.1NBT-0.6ST-0.3PT solid solutions. Indeed, the increase of electrostriction coefficient with the increase of temperature was observed for most of the compositions.

The piezoelectric coefficients in NBT-ST-PT solid solutions are nearly the same for all the compositions. The small differences in d_{max} can be explained by the temperature dependence of piezoelectric coefficient. This means that for some compositions the phase transition is closer to the room temperature. The piezo-coefficient increases when the transition temperature is approached. Another explanation can be related to the nature of the piezoelectric effect in the system. It was mentioned before that the temperature dependences of g_{33} indicates that the piezo-effect in these systems occur due to the electrostriction. In this case, the spontaneous polarization is different for all the compositions at the temperature where the piezo-coefficient is determined.

The only composition which stands out in the NBT-ST-PT system is $x = 0.1$. It has the largest d_{init} and g_{33}. This composition might be considered as a morphotropic phase boundary of 0.4NBT-(0.6-x)ST-xPT phase diagram. This result can be explained by the polarization rotation mechanism which is thought to be the cornerstone of the high piezoelectric response in the MPB compositions of relaxor-PT solid solutions. The relaxor part of our solid solutions favors the off-centering of ions along the [111] direction. The lead titanate favors the distortions along the tetragonal *c* axis. 0.4NBT-0.5ST-0.1PT composition is very close to the ferroelectric phase. This means that the application of electric field can easily rotate the [111] displacements along the tetragonal phase. This induces the ferroelectric phase and keeps it stable. The polarization rotation mechanism thus is responsible for higher piezoelectric response relative to some other compositions in NBT-ST-PT solid solutions.

Finally, it is obvious from the Table 4.2 that the piezoelectric properties of NBT-ST-PT solid solutions are not exceptional. The PMN-17PT single crystals which are far away from the morphotropic phase boundary, has much better piezoelectric properties. This is due to the fact that its remanent polarization is larger. The mechanism of piezoelectric effect is the same (biased electrostriction). The only advantage of some compositions in NBT-ST-PT family is that they have the phase transition at higher temperatures than PMN-17PT. This increases the temperature stability of these compositions and might be favorable for some applications. Another advantage is the ability to control the coercive field in rather broad field interval (2.5-10 kV/cm). The PMN-17PT system is only suitable for the soft-piezoelectric applications since the coercive field is rather small (< 3 kV/cm). So, the NBT-ST-PT system gives quite a lot of degrees of freedom for the tunability of piezoelectric properties while PMN-17PT surpasses it with larger piezoelectric coefficients.

4.2.2.5 Local Piezoelectric Response

The PFM images were captured for all the compositions in the (0.4-*y*)NBT-0.6ST-*y*PT system. It was shown in the two previous subsections that the 0.3NBT-0.6ST-0.1PT composition is close to paraelectric behaviour at room temperature. The PFM experiments could not be performed below the room temperature thus it was impossible to reach the temperature which would correspond to the permittivity peak at low frequencies.

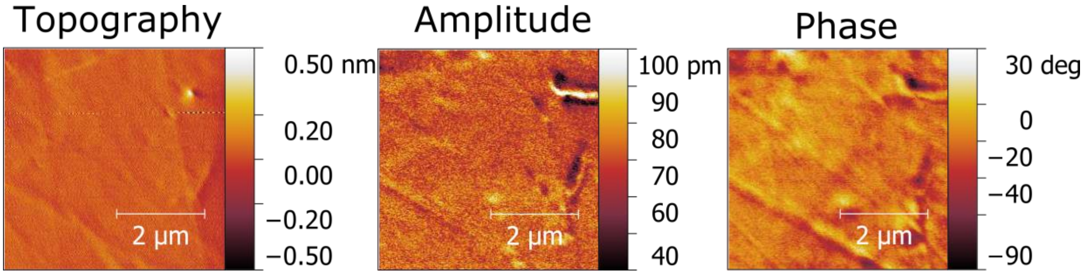

Figure 4.2.37 Room temperature LPFM images of 0.3NBT-0. 6ST-0.1PT solid solutions.

The room temperature LPFM images of 0.3NBT-0.6ST-0.1PT solid solutions are presented in Figure 4.2.37. The amplitude and phase images are quite noisy. It is clearly seen that the phase image mimics the features of topography. It is obvious that no signal related to the local polarization can be observed in the images. This correlates with the macroscopic electromechanical response which shows purely electrostrictive behaviour. There was no evolution of PFM signal when the temperature is changed thus the images does not hold any valuable information.

The more sensitive technique, DART, was also measured for this sample but unfortunately it did not reveal any response which would be similar to canonical relaxor ferroelectrics. This reveals the absence of polar correlations at room temperature even at the nanoscale (or these correlations are very weak and cannot be detected within the experimental limitations).

Figure 4.2.38 presents the LPFM images of 0.2NBT-0.6ST-0.2PT solid solutions. The images are presented at different magnifications. A polar pattern can be seen in the amplitude image (middle panel) of column (b). The labyrinth-like polar pattern can be obviously seen both in amplitude (middle panel of column (c)) and phase (bottom panel of column (c)). These patterns can be considered as a nanodomains (it is clear that the dimensions of the polar areas are not larger than 500 nm) because at room temperature 0.2NBT-0.6ST-0.2PT solid solutions is in ferroelectric phase. The nanodomain pattern is very irregular and it does not resemble a stripe structure like it should be (it supposed to be consequent light and dark stripes). The ceramics have a random orientation of different grains. The PFM signal is much stronger in the lateral mode. The complicated polar pattern might be explained by different orientations of grains as well as different grain sizes. The grain boundary can be observed in the middle panel of Figure 4.2.38 (b). The magnified image (Figure 4.2.38 (c)) was taken in the vicinity of this boundary. The distinction of polar pattern is evident in the previously mentioned image. Within the same grain, complexity of the polar pattern might also arise due to different displacement of ferro-active ions.

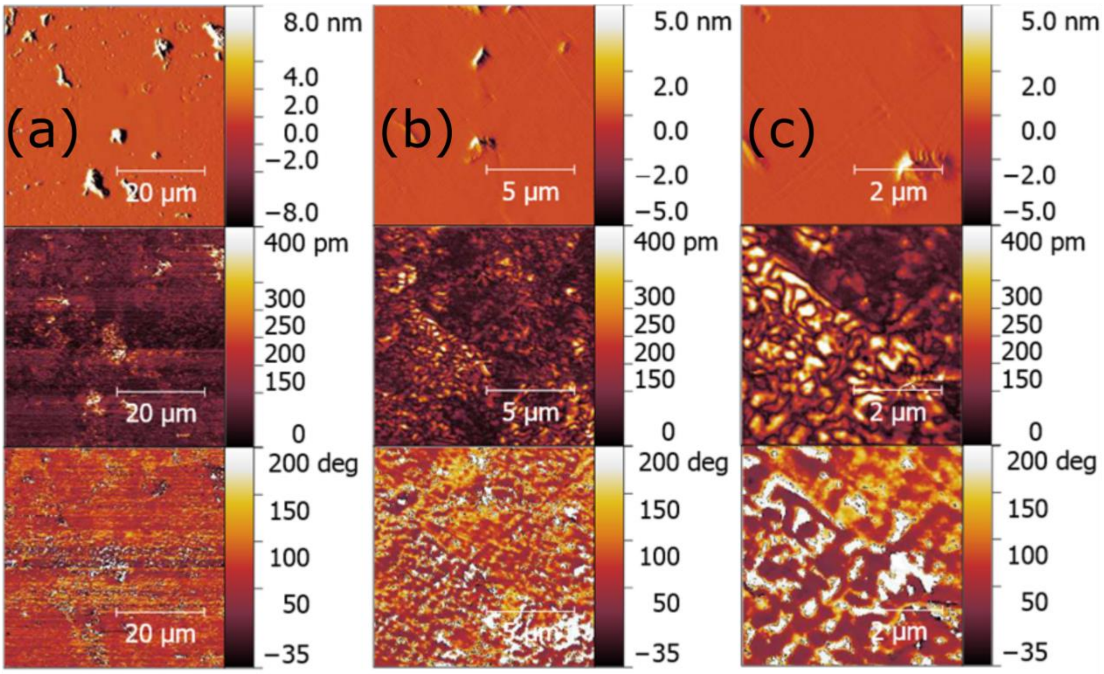

Figure 4.2.38 LPFM images of 0.2NBT-0.6ST-0.2PT solid solutions at different magnification: (a) 50 × 50 µm2; (b) 12.5 × 12.5 µm^2; (c) 5 × 5 µm^2. Top panel represents the topography; middle panel represents amplitude of LPFM signal; bottom panel represents the LPFM phase.

The domain structure resembles the ones observed in rhombohedral side of PMN-xPT compositions[193,194]. It also has similar features to the TTB family materials like strontium barium niobate (SBN)[205]. The significant difference is that 0.2NBT-0.6ST-0.2PT solid solutions have a well-defined structural phase transition which is debatable in the case of PMN-xPT systems. This proves that the correlation between the domains is much stronger in the current case. It is sufficient to form the macroscopic ferroelectric order within the grains.

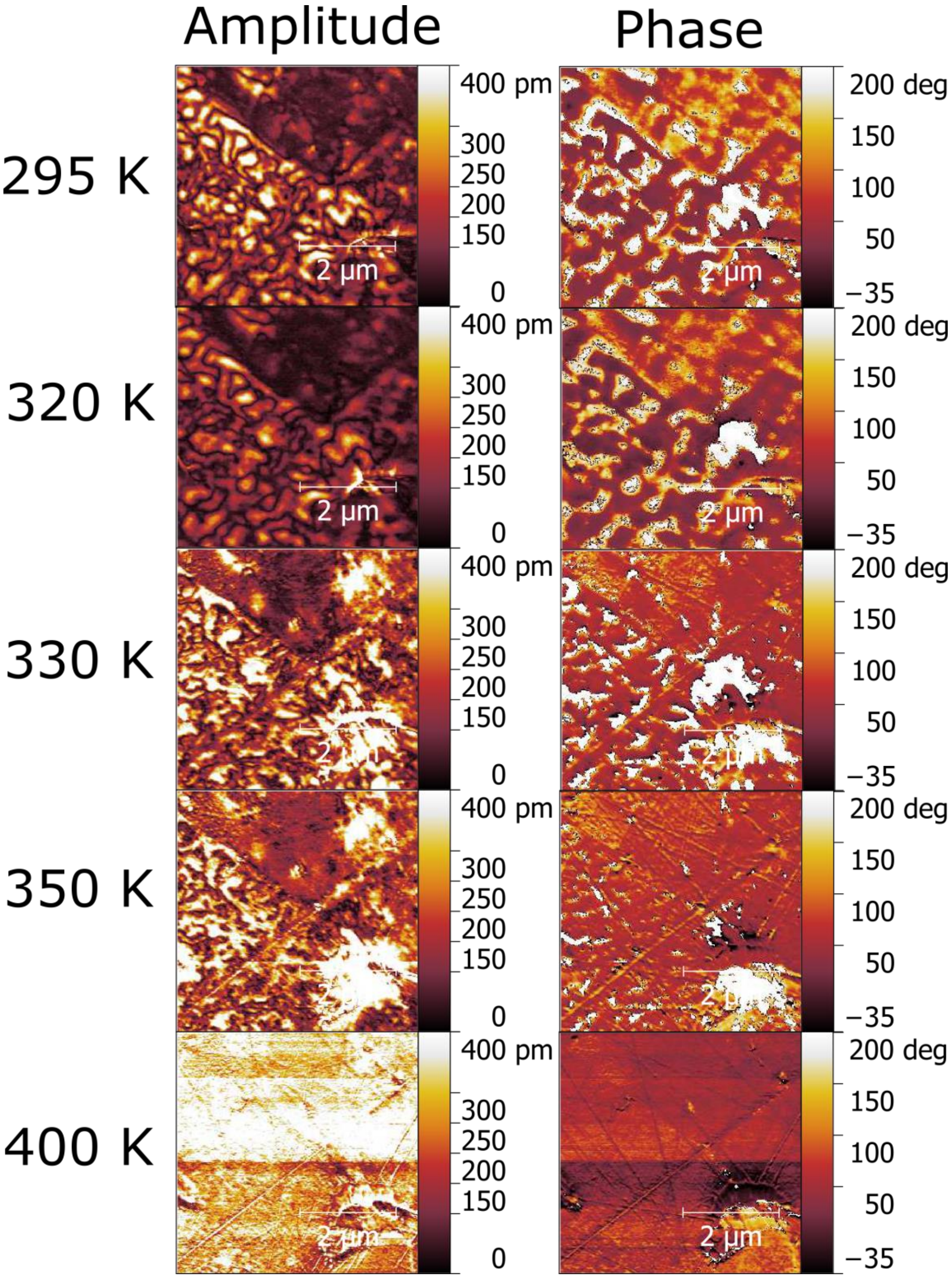

Figure 4.2.39 Temperature evolution of LPFM signal in the 0.2NBT-0.6ST-0.2PT solid solutions. The same area was scanned as in Figure 4.2.38 (c).

The temperature evolution of the LPFM signal is presented in Figure 4.2.39. The labyrinth structure loses intensity with the increase of temperature. Similar structure persists above the phase transition and gradually fades as the temperature increases. It can be seen that the PFM signal is absent in 400 K image (amplitude and phase images reflect the topography completely). The shrinkage of the polar domains can also be observed with the increase of temperature. Some of the nanodomains disappear above the phase transition (the area of darker spots increases). The images above the 320 K are much lighter but this is not related to the PFM signal. The dielectric peak is above the 320 K and thus the permittivity is very large. It seems that due to the electrostatic contribution the signal gets stronger.

Despite the probable superposition with an electrostatic interaction, it is obvious that some polar entities persist in a rather broad temperature range above the T_C. Due to the decrease of the correlation length, the polar entities get smaller. They seem to be isolated from each other by nonpolar areas. This actually reminds the PNRs in nonpolar matrix. Such behaviour is probably the underlying cause of the broad dielectric dispersion above T_c. The nanodomains become as a localized polar fluctuations which significantly contribute to the dielectric permittivity.

The behaviour of polar structures in these ceramics is non-ergodic. The initial measurement was performed on the annealed ceramics. After measurements on heating up to 450 K, the cooling polar structure is not completely reproduced. This indicates strong dependence on the thermal history. After the sample was cooled down from the 450 K, the VPFM images resemble the picture which was initially observed at room temperature LPFM images. It might indicate that within the grains the polarization can be oriented in several directions and might be the reason for such non-ergodic behaviour (the VPFM images are not provided here). It might also be related to the 1st order nature of the phase transition. This composition has quite a broad thermal hysteresis in the dielectric permittivity. This means that we cannot exactly probe the same conditions after cooling down the sample.

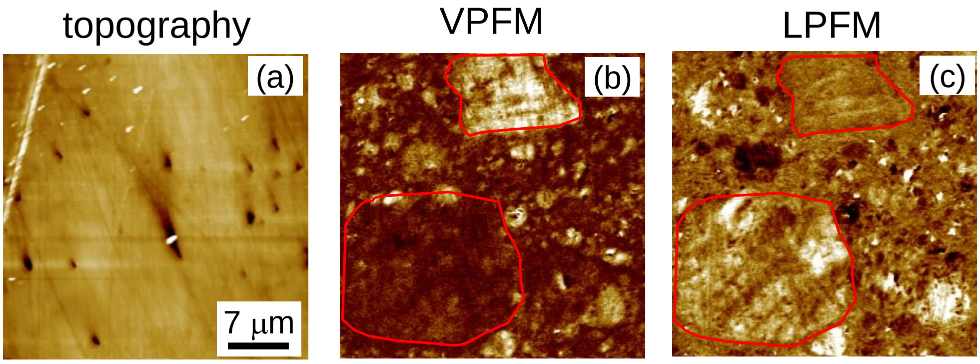

Figure 4.2.40 Topography (a), vertical (b) and lateral (c) PFM images of 0.1NBT-0.6ST-0.3PT ceramics measured at room temperature. Grains with stripe domains are marked red.

The most interesting case for the PFM studies is the 0.1NBT-0.6ST-0.3PT. The macroscopic properties of the phase transition show some evidence that the relaxor phase is absent in this composition. Thus, it is interesting to see possible evolution of the polar structures in this composition and to explain some of the peculiar macroscopic features above the phase transition temperature.

Figure 4.2.40 shows the topography, vertical and lateral PFM images of 0.1NBT-0.6ST-0.3PT taken at room temperature. One can distinguish between two very different domain patterns. In some grains relatively large quasi-regular stripe domains can be seen (these grains are marked red). In other grains much finer and less regular domains are observed.

This inhomogeneity of the polar structure might be related to a variation of the microstructure of the ceramics. The stripe domains are observed in large grains with sizes larger than 10 μm, while the irregular domains are typical for smaller grains with sizes of only a few microns. The larger grains favor the formation of regular domain patterns while smaller grains lead to irregular domains or are single domain. The situation might be similar to the one observed in $BaTiO_3$ ceramics, when a cross-over from a polydomain to single domain state occurs with the decrease of grain size[206]. PFM images of 0.1NBT-0.6ST-0.3PT taken up on heating are shown in Figure 4.2.41. When approaching the phase transition temperature, the PFM signal varies differently in different areas. Around 350 K the PFM contrast in the grains with quasiregular stripe domains disappears. No decay of these domains to smaller nanodomains was observed. This is the temperature where a drastic increase in dielectric permittivity is observed (see Figure 4.2.18). Thus, the 1st order phase transition is related to the properties of larger grains. Apparently, these grains have all the features of normal ferroelectrics. We assume that the dielectric anomaly associated with the 1st order phase transition and the significant increase of permittivity is related to a phase transition in the large grains.

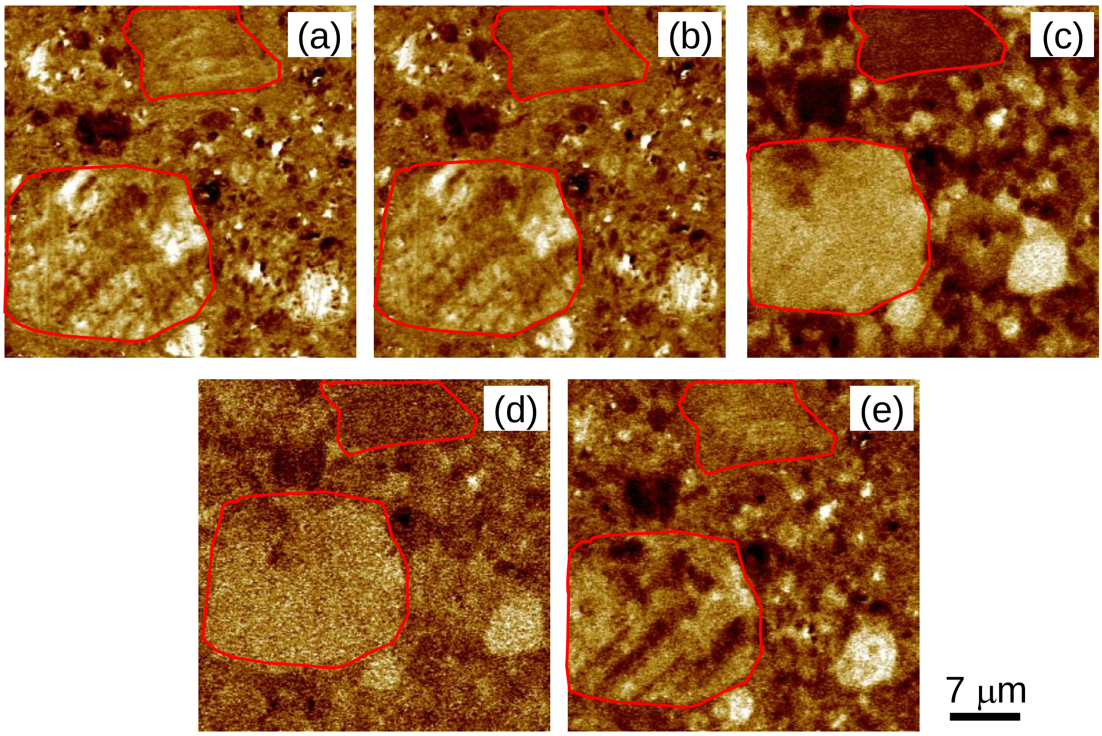

Figure 4.2.41 Lateral PFM images taken on heating at 299 K (a), 323 K (b), 348 K (c), 373 K (d), and after cooling back to 299 K (e).

The PFM signal from regions with irregular domain patterns persists much above the macroscopic phase transition temperature (Figure 4.2.41 (d)). Figure 4.2.42 shows a closer look onto such a region. To enhance the signal to noise ratio the measurements were done in the dual-amplitude resonance tracking mode (DART-PFM) which operates around the cantilever resonance frequency. Here the amplitude of the lateral PFM signal is presented. One can see that the pattern consists of both relatively large micron-size domains and nanodomains with sizes of 100 nm and smaller. Around 350 K the nanodomains decay into even smaller entities persisting at least up to 398 K (at higher temperatures reliable observation of nanodomains was impeded by the thermal drift). It seems that these nanodomains are responsible for the broad dispersion in dielectric permittivity around the Curie temperature. The larger domains show a continuous decay above T_C both in their size and in the intensity of the PFM signal. Some of these domains can be observed even 90 K above the macroscopic Curie temperature (Figure 4.2.42 (h)).

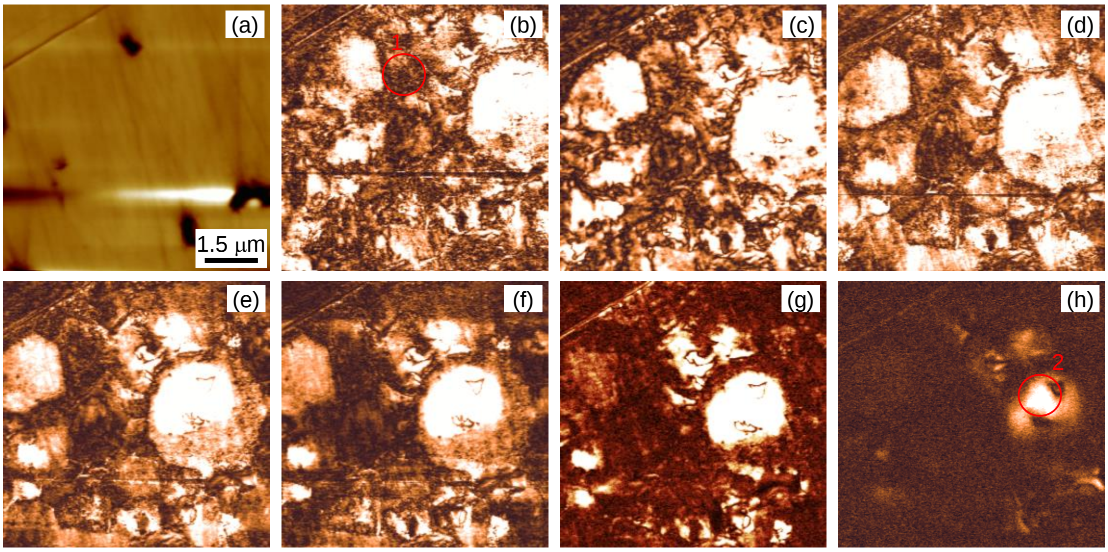

Figure 4.2.42 Topography (a) and DART PFM images (lateral signal) taken on heating at 298 K (b), 323 K(c), 348 K (d), 373 K (e), 398 K (f), 423 K (g), and 448 K (h). A region of nanodomains and a "very stable" domain are marked by circles 1 and 2, respectively.

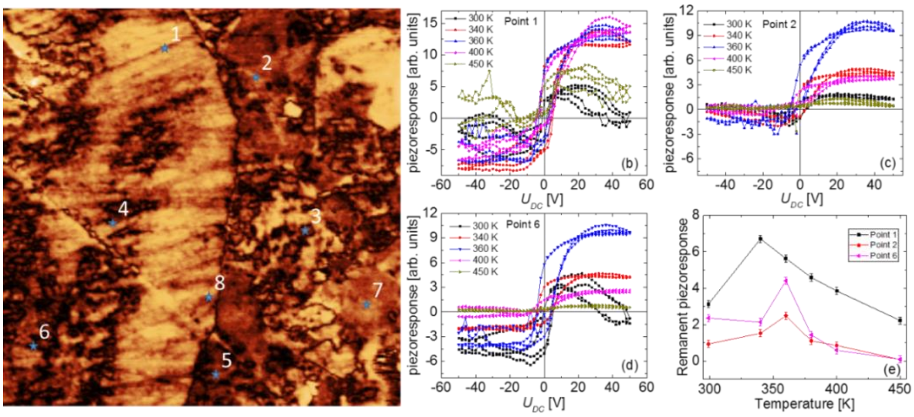

Figure 4.2.43 Local piezoresponse hysteresis loops measured inside a grain with irregular domain patterns. Measurement locations are shown in the DART PFM image (a). Panels (b)-(d) show examples of the hysteresis loops taken at different temperatures. Panel (e) shows the temperature dependences of the remanent piezoresponse for the various locations.

To study the effect of temperature on local polarization reversal we performed switching spectroscopy PFM experiments in several locations inside a region with irregular domains (Figure 4.2.43). The location 1 corresponds to a “very stable” domain, while locations 3 and 6 correspond to nanodomains. The PFM hysteresis loops indicating the locally switchable polarization can be observed up to 400 K and for location 1 even at 450 K. Temperature dependences of the remanent piezoresponse estimated from the local hysteresis loops show a maximum around 360 K that roughly corresponds to the peak of the pyroelectric current (see Figure 4.2.27). Taking into account that the PFM signal is proportional to the value of the local piezoelectric coefficient, such a maximum is expected around the Curie temperature where the piezoelectric coefficient increases.

Figure 4.2.44 shows the PFM images taken after switching spectroscopy experiments at different temperatures. At room temperature all locations were locally poled. Above the macroscopic transition temperature (360 K) regions 1, 4, and 6 still show some remanent polarization which weakens with the increase of temperature. It only becomes insignificant at relatively high temperature (450 K).

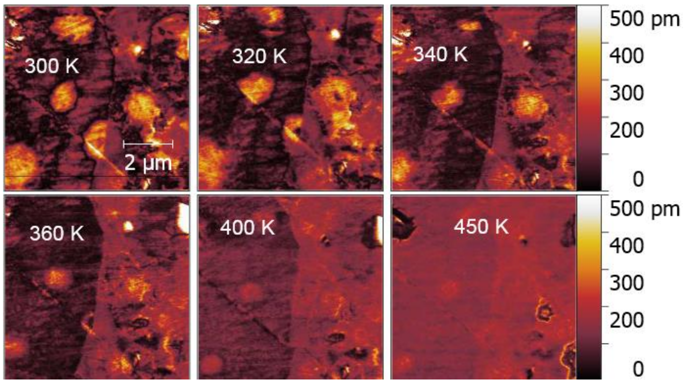

Figure 4.2.44 Temperature evolution of PFM signal obtained from the areas which were poled at room temperature.

The results of the PFM studies allow us to assume that namely the grains with irregular domain structure are responsible for the deviation from the normal ferroelectric behavior in the studied material. The gradual decay of the piezoresponse above the Curie temperature explains the shape of the macroscopic polarization hysteresis loops above the phase transition temperature (Figure 4.2.31 (c)). The polarization related to both nanodomains and residual micron size domains causes the gradual decrease of the macroscopic polarization above the phase transition temperature. Interestingly, some of the domains are very stable and exist much above the phase transition. They still occupy about 8-9 % and 2-4 % of the scanned area at 425 K and 475 K, respectively. One can assume that these domains are pinned by some internal defects or are related to local compositional fluctuations. To check chemical homogeneity of the ceramics the EDS and TOF-SIMS experiments and analysis were performed. The results are presented in Figures S4 and S5 of APPENDIX II. It was found that most of the sample surface shows a homogeneous distribution of A-site elements, namely Pb, Sr, and Bi. Only for some grains a higher Pb/Sr ratio was observed. These grains have a size of about 1 micron and occupy ~ 4 % of the sample area, according to TOF-SIMS. The size and relative occupation allows us to correlate them to the regions showing residual domains at temperatures much higher than the macroscopic T_C (very stable domain in Figure 4.2.42). However, most of the grains showing nanodomains as well as the grains with the large stripe domains have similar chemical composition. Of course, small local variations of the chemical composition on the nanometer scale cannot be resolved by the techniques used and therefore cannot be excluded.

Mechanical stresses can stabilize a polar state in relaxor ceramics much above the transition temperature[207]. A similar effect was observed in the measurement of second harmonic generation in PMN-PT ceramics[208], where the stabilization of PNRs far above T_c was observed in fine-grained ceramics. These residual polar domains might be responsible for the strong deviation from the Curie-Weiss behavior observed above T_c.

An important issue concerning coexistence of distinctly different polar structures is the interaction between them. The macroscopic measurements show that the investigated ceramic sample acts as a single phase material (single switching process, normal ferroelectric phase without additional dispersions below T_c). It might be a proof that grains with irregular domains correspond to the same phase, but due to local chemical inhomogeneities and probably due to local stresses they are not able to form regular domain patterns and show different local behavior.

The PFM studies show that the formation of the ferroelectric phase in 0.1NBT-0.6ST-0.3PT is rather complicated. Different domain patterns form at different temperatures in different regions of the sample. On the one hand, this might be related to local compositional fluctuation. The situation might be similar to materials with the so-called diffuse phase transition, e.g. $Ba(Ti_{1-x}Sn_x)O_3$ with x = 0.10 - 0.15[93]. In these materials, coexistence of ferroelectric domains and paraelectric regions around the phase transition temperature has been observed together with a broad dielectric permittivity peak and absence of frequency dependence of the dielectric peak position. Diffuse phase transition behavior is an intermediate state between a ferroelectric and a relaxor. It appears when the doping introduced disorder is still not sufficient to completely suppress the long range order, but is enough to diminish polar correlations in some parts.

On the other hand, the microstructure, the local mechanical and/or electrical stress fields at defects, and the grain boundaries may stabilize nanodomains in some grains above the global phase transition temperature. To sum up, the internal stresses and chemical disorder result in very complex polar structures containing micro to nano-sized polar domains, which is the underlying cause of the complexity of the macroscopic dielectric response around the phase transition.

4.2.2.6 Summary

The studies of NBT-ST-PT solid solutions revealed that the dielectric anomalies are related to the relaxation mode in all the compositions. The phonon softening is not present at the Γ-point of Brillouin zone.

The domain structures in NBT-ST-PT solid solutions depend on the grain size. Different type of polar structures can coexist in different grains. The complexity of domain structure of NBT-ST-PT solid solutions has weak impact on the piezoelectric properties. The piezoelectricity in the system is of electrostrictive nature. The underlying physics of the electromechanical properties in this family of solid solutions is nearly independent on the sites where lead is introduced. These substitutions can effectively tune the coercive field and transition temperature which is often important for the applications.

The MPB of NBT-ST-PT solid solutions correspond to the compositions with an electric field inducible phase transition. These compositions have the largest electromechanical displacements in the vicinity of electric field inducible phase transition.

5. Conclusions

The following conclusions can be drawn after achievieng the goals of the thesis:

1. The largest contribution to the dielectric permittivity stems from the central mode in the investigated disordered perovskite oxides. The dielectric anomalies are due to the relaxation mode and have a strong order-disorder character. Phonon instabilities play no role in the mechanism of the phase transitions.
2. The electrostrictive behaviour in relaxor-PT solid solutions have the same origin. It is independent on the substitutional/charge disorder of the relaxor counterpart of the solid solutions. The possible improvement of electrostriction might be reached by simultaneous chemical substitution in different lattice sites.
3. The macroscopic properties of relaxor-PT systems are not dependent on the site where the charge disorder is present. They possess the same features of lattice dynamics. Lead titanate plays an important role in Pb-based disordered systems but the introduction of lead to the A-site is not a fruitful way to improve the electromechanical properties.
4. Locally, the two different investigated relaxor-PT systems show quite distinct polar behaviour. It indicates that the interaction between the heavily polarizable matrix and local inhomogeneities is different. It depends on the site where the charge disorder is present. The further studies on a charge disorder in both A and B sites might improve the contribution of domains and domain walls to the piezoelectricity in disordered perovskites.

References

1. von Hippel, A. Ferroelectricity, Domain Structure, and Phase Transitions of Barium Titanate. *Rev Mod Phys* **22,** 221–237 (1950).
2. Devonshire, A. F. XCVI. Theory of barium titanate. *Lond. Edinb. Dublin Philos. Mag. J. Sci.* **40,** 1040–1063 (1949).
3. Devonshire, A. F. CIX. Theory of barium titanate—Part II. *Lond. Edinb. Dublin Philos. Mag. J. Sci.* **42,** 1065–1079 (1951).
4. Burns, G. & Scott, B. A. ‘Dirty’ displacive ferroelectrics. *Solid State Commun.* **13,** 417–421 (1973).
5. Westphal, V., Kleemann, W. & Glinchuk, M. D. Diffuse phase transitions and random-field-induced domain states of the ‘relaxor’ ferroelectric $PbMg_{1/3}Nb_{2/3}O_3$. *Phys. Rev. Lett.* **68,** 847–850 (1992).
6. Rödel, J. *et al.* Perspective on the Development of Lead-free Piezoceramics. *J. Am. Ceram. Soc.* **92,** 1153–1177 (2009).
7. Zhang, K. *et al.* Research progress and materials selection guidelines on mixed conducting perovskite-type ceramic membranes for oxygen production. *RSC Adv.* **1,** 1661–1676 (2011).
8. Glazer, A. M. The classification of tilted octahedra in perovskites. *Acta Crystallogr. B* **28,** 3384–3392 (1972).
9. Woodward, P. M. Octahedral Tilting in Perovskites. I. Geometrical Considerations. *Acta Crystallogr. B* **53,** 32–43 (1997).
10. Zhang, N. *et al.* The missing boundary in the phase diagram of $PbZr_{1-x}Ti_xO_3$. *Nat. Commun.* **5,** 5231 (2014).
11. Bokov, A. A. & Ye, Z.-G. Recent progress in relaxor ferroelectrics with perovskite structure. in *Frontiers of Ferroelectricity* 31–52 (Springer US, 2007).
12. Chu, F., Setter, N. & Tagantsev, A. K. The spontaneous relaxor-ferroelectric transition of $Pb(Sc_{0.5}Ta_{0.5})O_3$. *J. Appl. Phys.* **74,** 5129–5134 (1993).

13. Chu, F., Reaney, I. M. & Setter, N. Spontaneous (zero-field) relaxor–to–ferroelectric-phase transition in disordered $Pb(Sc_{1/2}Nb_{1/2})O_3$. *J. Appl. Phys.* **77,** 1671–1676 (1995).

14. Perrin, C. *et al.* Influence of B-site chemical ordering on the dielectric response of the Pb(Sc 1/2 Nb 1/2)O 3 relaxor. *J. Phys. Condens. Matter* **13,** 10231 (2001).

15. Setter, N. What is a ferroelectric–a materials designer perspective. *Ferroelectrics* **500,** 164–182 (2016).

16. Bussmann-Holder, A. The polarizability model for ferroelectricity in perovskite oxides. *J. Phys. Condens. Matter* **24,** 273202 (2012).

17. Strukov, B. A. & Levanyuk, A. P. *Ferroelectric Phenomena in Crystals: Physical Foundations*. (Springer-Verlag, 1998).

18. Cochran, W. Crystal stability and the theory of ferroelectricity. *Adv. Phys.* **9,** 387–423 (1960).

19. Lyddane, R. H., Sachs, R. G. & Teller, E. On the Polar Vibrations of Alkali Halides. *Phys. Rev.* **59,** 673–676 (1941).

20. Axe, J. D. Apparent Ionic Charges and Vibrational Eigenmodes of $BaTiO_3$ and Other Perovskites. *Phys. Rev.* **157,** 429–435 (1967).

21. Hlinka, J., Petzelt, J., Kamba, S., Noujni, D. & Ostapchuk, T. Infrared dielectric response of relaxor ferroelectrics. *Phase Transit.* **79,** 41–78 (2006).

22. Hlinka, J. *et al.* Coexistence of the Phonon and Relaxation Soft Modes in the Terahertz Dielectric Response of Tetragonal $BaTiO_3$. *Phys. Rev. Lett.* **101,** 167402 (2008).

23. Lines, M. E. & Glass, A. M. *Principles and Applications of Ferroelectrics and Related Materials*. (Clarendon Press, 1979).

24. Zalar, B., Laguta, V. V. & Blinc, R. NMR Evidence for the Coexistence of Order-Disorder and Displacive Components in Barium Titanate. *Phys. Rev. Lett.* **90,** 037601 (2003).

25. Stern, E. A. Character of Order-Disorder and Displacive Components in Barium Titanate. *Phys. Rev. Lett.* **93,** 037601 (2004).

26. Pirc, R. & Blinc, R. Off-center Ti model of barium titanate. *Phys. Rev. B* **70,** 134107 (2004).

27. Bussmann-Holder, A., Beige, H. & Völkel, G. Precursor effects, broken local symmetry, and coexistence of order-disorder and displacive dynamics in perovskite ferroelectrics. *Phys. Rev. B* **79,** 184111 (2009).

28. Mathan, N. de *et al.* A structural model for the relaxor $PbMg_{1/3}Nb_{2/3}O_3$ at 5 K. *J. Phys. Condens. Matter* **3,** 8159 (1991).

29. Bussmann-Holder, A. & Bishop, A. R. Intrinsic local modes and heterogeneity in relaxor ferroelectrics. *J. Phys. Condens. Matter* **16,** L313 (2004).

30. Bussmann-Holder, A., Bishop, A. R. & Egami, T. Relaxor ferroelectrics and intrinsic inhomogeneity. *EPL Europhys. Lett.* **71,** 249 (2005).

31. Gehring, P. M., Wakimoto, S., Ye, Z.-G. & Shirane, G. Soft Mode Dynamics above and below the Burns Temperature in the Relaxor $PbMg_{1/3}Nb_{2/3}O_3$. *Phys. Rev. Lett.* **87,** 277601 (2001).

32. Bishop, A. R., Bussmann-Holder, A., Kamba, S. & Maglione, M. Common characteristics of displacive and relaxor ferroelectrics. *Phys. Rev. B* **81,** 064106 (2010).

33. Burns, G. & Scott, B. A. Index of refraction in 'dirty' displacive ferroelectrics. *Solid State Commun.* **13,** 423–426 (1973).

34. Burns, G. & Dacol, F. H. Crystalline ferroelectrics with glassy polarization behavior. *Phys. Rev. B* **28,** 2527–2530 (1983).

35. Egami, T. Local Structure of Ferroelectric Materials. *Annu. Rev. Mater. Res.* **37,** 297–315 (2007).

36. Hirota, K., Ye, Z.-G., Wakimoto, S., Gehring, P. M. & Shirane, G. Neutron diffuse scattering from polar nanoregions in the relaxor $Pb(Mg_{1/3}Nb_{2/3})O_3$. *Phys. Rev. B* **65,** 104105 (2002).

37. La-Orauttapong, D., Toulouse, J., Robertson, J. L. & Ye, Z.-G. Diffuse neutron scattering study of a disordered complex perovskite $Pb(Zn_{1/3}Nb_{2/3})O_3$ crystal. *Phys. Rev. B* **64,** 212101 (2001).

38. Shvartsman, V. V. & Kholkin, A. L. Polar structures of $PbMg_{1/3}Nb_{2/3}O_3$-$PbTiO_3$ relaxors: piezoresponse force microscopy approach. *J. Adv. Dielectr.* **02,** 1241003 (2012).
39. Bdikin, I. K., Shvartsman, V. V. & Kholkin, A. L. Nanoscale domains and local piezoelectric hysteresis in $Pb(Zn_{1/3}Nb_{2/3})O_3$-4.5%$PbTIO_3$ single crystals. *Appl. Phys. Lett.* **83,** 4232–4234 (2003).
40. Shvartsman, V. V., Dec, J., Łukasiewicz, T., Kholkin, A. L. & Kleemann, W. Evolution of the Polar Structure in Relaxor Ferroelectrics Close to the Curie Temperature Studied by Piezoresponse Force Microscopy. *Ferroelectrics* **373,** 77–85 (2008).
41. Dec, J., Kleemann, W., Shvartsman, V. V., Lupascu, D. C. & Łukasiewicz, T. From mesoscopic to global polar order in the uniaxial relaxor ferroelectric $Sr_{0.8}Ba_{0.2}Nb_2O_6$. *Appl. Phys. Lett.* **100,** 052903 (2012).
42. Shvartsman, V. V., Dkhil, B. & Kholkin, A. L. Mesoscale Domains and Nature of the Relaxor State by Piezoresponse Force Microscopy. *Annu. Rev. Mater. Res.* **43,** 423–449 (2013).
43. Koreeda, A., Taniguchi, H., Saikan, S. & Itoh, M. Fractal Dynamics in a Single Crystal of a Relaxor Ferroelectric. *Phys. Rev. Lett.* **109,** 197601 (2012).
44. Hlinka, J. Do we need the ether of polar nanoregions? *J. Adv. Dielectr.* **02,** 1241006 (2012).
45. Kamba, S. *et al.* Dielectric dispersion of the relaxor PLZT ceramics in the frequency range 20 Hz-100 THz. *J. Phys. Condens. Matter* **12,** 497 (2000).
46. Bovtun, V. *et al.* Broad-band dielectric response of $PbMg_{1/3}Nb_{2/3}O_3$ relaxor ferroelectrics: Single crystals, ceramics and thin films. *J. Eur. Ceram. Soc.* **26,** 2867–2875 (2006).
47. Bell, A. J. Calculations of dielectric properties from the superparaelectric model of relaxors. *J. Phys. Condens. Matter* **5,** 8773 (1993).
48. Bobnar, V., Filipič, C., Levstik, A. & Kutnjak, Z. High-temperature dielectric response of $(1-x)Pb(Mg_{1/3}Nb_{2/3})O_3-xPbTiO_3$: Does Burns

temperature exist in ferroelectric relaxors? *J. Appl. Phys.* **107,** 084104 (2010).

49. Viehland, D., Jang, S. J., Cross, L. E. & Wuttig, M. Freezing of the polarization fluctuations in lead magnesium niobate relaxors. *J. Appl. Phys.* **68,** 2916–2921 (1990).
50. Grigalaitis, R., Banys, J., Sternberg, A., Bormanis, K. & Zauls, V. Dynamics of Polar Clusters in PMN Ceramics: Comparison with PMN Single Crystal. *Ferroelectrics* **340,** 147–153 (2006).
51. Banys, J., Grigalaitis, R., Mikonis, A., Macutkevic, J. & Keburis, P. Distribution of relaxation times of relaxors: comparison with dipolar glasses. *Phys. Status Solidi C* **6,** 2725–2730 (2009).
52. Grigalaitis, R. *et al.* Dielectric Dispersion in Pure PMN and PMN with 10% PT Single Crystals. *Ferroelectrics* **339,** 21–28 (2006).
53. Macutkevic, J. *et al.* Infrared and broadband dielectric spectroscopy of PZN-PMN-PSN relaxor ferroelectrics: Origin of two-component relaxation. *Phys. Rev. B* **74,** 104106 (2006).
54. Grigalaitis, R. *et al.* Dielectric spectroscopy and distribution of relaxation times of PMN-PSN ceramics. *J. Electroceramics* **19,** 433–435 (2007).
55. Höchli, U. T., Knorr, K. & Loidl, A. Orientational glasses. *Adv. Phys.* **39,** 405–615 (1990).
56. Levstik, A., Kutnjak, Z., Filipič, C. & Pirc, R. Glassy freezing in relaxor ferroelectric lead magnesium niobate. *Phys. Rev. B* **57,** 11204–11211 (1998).
57. Blinc, R., Laguta, V. V., Zalar, B. & Banys, J. Polar nanoclusters in relaxors. in *Frontiers of Ferroelectricity* 27–30 (Springer US, 2007).
58. Vollmayr, H., Kree, R. & Zippelius, A. Discrete-state models of orientational glasses. *Phys. Rev. B* **44,** 12238–12262 (1991).
59. Binder, K. & Reger, J. D. Theory of orientational glasses models, concepts, simulations. *Adv. Phys.* **41,** 547–627 (1992).
60. Pirc, R., Blinc, R. & Wiotte, W. Correlated random bonds and random fields in proton glasses. *Phys. B Condens. Matter* **182,** 137–144 (1992).

61. Viehland, D., Li, J. F., Jang, S. J., Cross, L. E. & Wuttig, M. Glassy polarization behavior of relaxor ferroelectrics. *Phys. Rev. B* **46,** 8013–8017 (1992).

62. Pirc, R. & Blinc, R. Spherical random-bond–random-field model of relaxor ferroelectrics. *Phys. Rev. B* **60,** 13470–13478 (1999).

63. Blinc, R. *et al.* NMR and the spherical random bond–random field model of relaxor ferroelectrics. *J. Phys. Chem. Solids* **61,** 177–183 (2000).

64. Blinc, R. *et al.* ^{207}Pb NMR study of the relaxor behavior in $PbMg_{1/3}Nb_{2/3}O_3$. *Phys. Rev. B* **63,** 024104 (2000).

65. Pirc, R., Tadić, B. & Blinc, R. Nonlinear susceptibility of orientational glasses. *Phys. B Condens. Matter* **193,** 109–115 (1994).

66. Hemberger, J., Ries, H., Loidl, A. & Böhmer, R. Static Freezing Transition at a Finite Temperature in a Quasi-One-Dimensional Deuteron Glass. *Phys. Rev. Lett.* **76,** 2330–2333 (1996).

67. Hemberger, J., Böhmer, R. & Loidl, A. Nonlinear susceptibilities and polydispersivity in dipolar glasses. *Phase Transit.* **65,** 233–261 (1998).

68. Maglione, M., Höchli, U. T. & Joffrin, J. Dipolar Glass State in $K_{1-x}Na_xTaO_3$. *Phys. Rev. Lett.* **57,** 436–439 (1986).

69. Bobnar, V., Kutnjak, Z., Pirc, R., Blinc, R. & Levstik, A. Crossover from Glassy to Inhomogeneous-Ferroelectric Nonlinear Dielectric Response in Relaxor Ferroelectrics. *Phys. Rev. Lett.* **84,** 5892–5895 (2000).

70. Glazounov, A. E. & Tagantsev, A. K. Phenomenological Model of Dynamic Nonlinear Response of Relaxor Ferroelectrics. *Phys. Rev. Lett.* **85,** 2192–2195 (2000).

71. Dec, J., Miga, S., Kleemann, W. & Dkhil, B. Nonlinear Dielectric Properties of PMN Relaxor Crystals within Landau-Ginzburg-Devonshire Approximation. *Ferroelectrics* **363,** 141–149 (2008).

72. Miga, S. & Dec, J. Non-linear Dielectric Response of Ferroelectric and Relaxor Materials. *Ferroelectrics* **367,** 223–228 (2008).

73. Miga, S., Dec, J. & Kleemann, W. Non-Linear Dielectric Response of Ferroelectrics, Relaxors and Dipolar Glasses. (2011). doi:10.5772/20380

74. Kleemann, W. *et al.* Uniaxial relaxor ferroelectrics: The ferroic random-field Ising model materialized at last. *EPL Europhys. Lett.* **57,** 14 (2002).

75. Pirc, R., Kutnjak, Z. & Novak, N. Compressible spherical dipolar glass model of relaxor ferroelectrics. *J. Appl. Phys.* **112,** 114122 (2012).

76. Shirane, G., Axe, J. D., Harada, J. & Remeika, J. P. Soft Ferroelectric Modes in Lead Titanate. *Phys. Rev. B* **2,** 155–159 (1970).

77. Remeika, J. P. & Glass, A. M. The growth and ferroelectric properties of high resistivity single crystals of lead titanate. *Mater. Res. Bull.* **5,** 37–45 (1970).

78. Cowley, R. A., Gvasaliya, S. N. & Roessli, B. Soft Modes and Relaxor Ferroelectrics. *Ferroelectrics* **378,** 53–62 (2009).

79. Bovtun, V. *et al.* Central-Peak Components and Polar Soft Mode in Relaxor $PbMg_{1/3}Nb_{2/3}O_3$ Crystals. *Ferroelectrics* **298,** 23–30 (2004).

80. Gehring, P. M., Park, S.-E. & Shirane, G. Soft Phonon Anomalies in the Relaxor Ferroelectric $Pb(Zn_{1/3}Nb_{2/3)})_{0.92}Ti_{0.08}O_3$. *Phys. Rev. Lett.* **84,** 5216–5219 (2000).

81. Swainson, I. P. *et al.* Soft phonon columns on the edge of the Brillouin zone in the relaxor $PbMg_{1/3}Nb_{2/3}O_3$. *Phys. Rev. B* **79,** 224301 (2009).

82. Koo, T. Y. *et al.* Anomalous transverse acoustic phonon broadening in the relaxor ferroelectric $Pb(Mg_{1/3}Nb_{2/3)})_{0.8}Ti_{0.2}O_3$. *Phys. Rev. B* **65,** 144113 (2002).

83. Phelan, D. *et al.* Role of random electric fields in relaxors. *Proc. Natl. Acad. Sci.* **111,** 1754–1759 (2014).

84. La-Orauttapong, D. *et al.* Phase diagram of the relaxor ferroelectric (1-x)$Pb(Zn_{1/3}Nb_{2/3})O_3$-x$PbTiO_3$. *Phys. Rev. B* **65,** 144101 (2002).

85. Hlinka, J. *et al.* Origin of the ``Waterfall'' Effect in Phonon Dispersion of Relaxor Perovskites. *Phys. Rev. Lett.* **91,** 107602 (2003).

86. Kojima, S. & Tsukada, S. Micro-Brillouin Scattering of Relaxor Ferroelectrics with Perovskite Structure. *Ferroelectrics* **405,** 32–38 (2010).

87. Kojima, S., Ahart, M., Sivasubramanian, V., Bokov, A. A. & Ye, Z.-G. Precursor dynamics of $\mathrm{Pb(B_{1/2}B'_{1/2})O_3}$-type relaxor ferroelectrics studied by broadband micro-brillouin scattering. *J. Adv. Dielectr.* **02,** 1241004 (2012).

88. Hehlen, B., Al-Sabbagh, M., Al-Zein, A. & Hlinka, J. Relaxor Ferroelectrics: Back to the Single-Soft-Mode Picture. *Phys. Rev. Lett.* **117,** 155501 (2016).

89. Fu, D. *et al.* Relaxor Pb(Mg<sub>1/3</subNb$_{2/3}$)O$_3$: A Ferroelectric with Multiple Inhomogeneities. *Phys. Rev. Lett.* **103,** 207601 (2009).

90. Kleemann, W. The relaxor enigma — charge disorder and random fields in ferroelectrics. *J. Mater. Sci.* **41,** 129–136 (2006).

91. Nuzhnyy, D. *et al.* Broadband dielectric response of $\mathrm{Ba(Zr,Ti)O_3}$ ceramics: From incipient via relaxor and diffuse up to classical ferroelectric behavior. *Phys. Rev. B* **86,** 014106 (2012).

92. Maiti Tanmoy, Guo R. & Bhalla A. S. Structure-Property Phase Diagram of $\mathrm{BaZr_xTi_{1-x}O_3}$ System. *J. Am. Ceram. Soc.* **91,** 1769–1780 (2008).

93. Shvartsman, V. V., Kleemann, W., Dec, J., Xu, Z. K. & Lu, S. G. Diffuse phase transition in $\mathrm{BaTi_{1-x}Sn_xO_3}$ ceramics: An intermediate state between ferroelectric and relaxor behavior. *J. Appl. Phys.* **99,** 124111 (2006).

94. Wang, D., Bokov, A. A., Ye, Z.-G., Hlinka, J. & Bellaiche, L. Subterahertz dielectric relaxation in lead-free $\mathrm{Ba(Zr,Ti)O_3}$ relaxor ferroelectrics. *Nat. Commun.* **7,** 11014 (2016).

95. Simon, A., Ravez, J. & Maglione, M. The crossover from a ferroelectric to a relaxor state in lead-free solid solutions. *J. Phys. Condens. Matter* **16,** 963 (2004).

96. Kleemann, W., Dec, J. & Miga, S. Superdipole glass ground state of relaxor ferroelectrics. *Ferroelectrics* **499,** 72–75 (2016).

97. Kleemann, W., Dec, J. & Miga, S. The cluster glass route of relaxor ferroelectrics. *Phase Transit.* **0,** 1–11 (2014).

98. Sherrington, D. BZT: A Soft Pseudospin Glass. *Phys. Rev. Lett.* **111,** 227601 (2013).

99. Samara, G. A. The relaxational properties of compositionally disordered ABO_3 perovskites. *J. Phys. Condens. Matter* **15,** R367 (2003).

100. Takenaka, H., Grinberg, I. & Rappe, A. M. Anisotropic Local Correlations and Dynamics in a Relaxor Ferroelectric. *Phys Rev Lett* **110,** 147602 (2013).

101. Filipič, C., Kutnjak, Z., Pirc, R., Canu, G. & Petzelt, J. $BaZr_{0.5}Ti_{0.5}O_3$: Lead-free relaxor ferroelectric or dipolar glass. *Phys. Rev. B* **93,** 224105 (2016).

102. Krauss, W., Schütz, D., Mautner, F. A., Feteira, A. & Reichmann, K. Piezoelectric properties and phase transition temperatures of the solid solution of $(1 - x)(Bi_{0.5}Na_{0.5})TiO_3$–$xSrTiO_3$. *J. Eur. Ceram. Soc.* **30,** 1827–1832 (2010).

103. Shrout, T. R. & Zhang, S. J. Lead-free piezoelectric ceramics: Alternatives for PZT? *J. Electroceramics* **19,** 113–126 (2007).

104. Rödel, J. *et al.* Transferring lead-free piezoelectric ceramics into application. *J. Eur. Ceram. Soc.* **35,** 1659–1681 (2015).

105. Coondoo, I., Panwar, N. & Kholkin, A. Lead-free piezoelectrics: Current status and perspectives. *J. Adv. Dielectr.* **03,** 1330002 (2013).

106. Dittmer, R., Jo, W., Damjanovic, D. & Rödel, J. Lead-free high-temperature dielectrics with wide operational range. *J. Appl. Phys.* **109,** 034107 (2011).

107. Aksel, E., Forrester, J. S., Kowalski, B., Jones, J. L. & Thomas, P. A. Phase transition sequence in sodium bismuth titanate observed using high-resolution x-ray diffraction. *Appl. Phys. Lett.* **99,** 222901 (2011).

108. Vakhrushev, S. B. *et al.* Phase transitions and soft modes in sodium bismuth titanate. *Ferroelectrics* **63,** 153–160 (1985).

109. Pronin, I. P., Syrnikov, P. P., Isupov, V. A., Egorov, V. M. & Zaitseva, N. V. Peculiarities of phase transitions in sodium-bismuth titanate. *Ferroelectrics* **25,** 395–397 (1980).

110. Keeble, D. S. *et al.* Bifurcated Polarization Rotation in Bismuth-Based Piezoelectrics. *Adv. Funct. Mater.* **23,** 185–190 (2013).

111. Dorcet, V., Trolliard, G. & Boullay, P. Reinvestigation of Phase Transitions in $Na_{0.5}Bi_{0.5}TiO_3$ by TEM. Part I: First Order Rhombohedral to Orthorhombic Phase Transition. *Chem. Mater.* **20,** 5061–5073 (2008).

112. Trolliard, G. & Dorcet, V. Reinvestigation of Phase Transitions in $Na_{0.5}Bi_{0.5}TiO_3$ by TEM. Part II: Second Order Orthorhombic to Tetragonal Phase Transition. *Chem. Mater.* **20,** 5074–5082 (2008).

113. Petzelt, J. *et al.* Infrared, Raman and high-frequency dielectric spectroscopy and the phase transitions in Na1/2Bi1/2TiO3. *J. Phys. Condens. Matter* **16,** 2719 (2004).

114. Noheda, B., Cox, D. E., Shirane, G., Gao, J. & Ye, Z.-G. Phase diagram of the ferroelectric relaxor $(1\text{-}x)PbMg_{1/3}Nb_{2/3}O3\text{-}xPbTiO_3$. *Phys. Rev. B* **66,** 054104 (2002).

115. Luo, H., Xu, G., Xu, H., Wang, P. & Yin, Z. Compositional Homogeneity and Electrical Properties of Lead Magnesium Niobate Titanate Single Crystals Grown by a Modified Bridgman Technique. *Jpn. J. Appl. Phys.* **39,** 5581 (2000).

116. Dunce, M., Birks, E., Antonova, M. & Sternberg, A. Phase Transitions in $Na_{1/2}Bi_{1/2}TiO_3\text{-}SrTiO_3\text{-}PbTiO_3$ Solid Solutions. *Ferroelectrics* **405,** 57–61 (2010).

117. Svirskas, S. *et al.* Dielectric properties of 0.4 $Na_{0.\,5}Bi_{0.\,5}TiO_3$–(0.6-x) $SrTiO_3$–$xPbTiO_3$ solid solutions. *Acta Mater.* **64,** 123–132 (2014).

118. Birks, E., Dunce, M., Antonova, M. & Sternberg, A. Phase transitions in modified Na1/2Bi1/2TiO3-SrTiO3 solid solutions. *Phys. Status Solidi C* **6,** 2737–2739 (2009).

119. Dunce, M., Birks, E., Antonova, M., Kundzinsh, M. & Sternberg, A. Phase transitions in $Na_{1/2}Bi_{1/2}TiO_3\text{-}SrTiO_3\text{-}PbTiO_3$ solid solutions. *Integr. Ferroelectr.* **108,** 125–133 (2009).

120. Grigas, J. *Microwave Dielectric Spectroscopy of Ferroelectrics and Related Materials*. (CRC Press, 1996).

121. Banys, J., Lapinskas, S., Rudys, S., Greicius, S. & Grigalaitis, R. High Frequency Measurements of Ferroelecrics and Related Materials in Coaxial Line. *Ferroelectrics* **414,** 64–69 (2011).

122. Kezionis, A., Kazlauskas, S., Petrulionis, D. & Orliukas, A. F. Broadband Method for the Determination of Small Sample's Electrical and Dielectric Properties at High Temperatures. *IEEE Trans. Microw. Theory Tech.* **62,** 2456–2461 (2014).

123. Kužel, P. & Petzelt, J. Time-resolved terahertz transmission spectroscopy of dielectrics. *Ferroelectrics* **239,** 79–86 (2000).

124. Havriliak, S. & Negami, S. A complex plane representation of dielectric and mechanical relaxation processes in some polymers. *Polymer* **8,** 161–210 (1967).

125. Zorn, R. Applicability of distribution functions for the Havriliak–Negami spectral function. *J. Polym. Sci. Part B Polym. Phys.* **37,** 1043–1044 (1999).

126. Zorn, R. Logarithmic moments of relaxation time distributions. *J. Chem. Phys.* **116,** 3204–3209 (2002).

127. Macutkevič, J., Banys, J. & Matulis, A. Determination of the Distribution of the Relaxation Times from Dielectric Spectra. *Nonlinear Anal. Model. Control* **9,** 75–88 (2004).

128. Brüesch, P. *Phonons: Theory and Experiments II: Experiments and Interpretation of Experimental Results*. (Springer-Verlag, 1986).

129. Gervais, F. & Piriou, B. Anharmonicity in several-polar-mode crystals: adjusting phonon self-energy of LO and TO modes in Al_2O_3 and TiO_2 to fit infrared reflectivity. *J. Phys. C Solid State Phys.* **7,** 2374 (1974).

130. BARKER, A. S. & LOUDON, R. Response Functions in the Theory of Raman Scattering by Vibrational and Polariton Modes in Dielectric Crystals. *Rev. Mod. Phys.* **44,** 18–47 (1972).

131. Binnig, G., Rohrer, H., Gerber, C. & Weibel, E. Surface Studies by Scanning Tunneling Microscopy. *Phys. Rev. Lett.* **49,** 57–61 (1982).

132. Bhushan, B. & Marti, O. Scanning Probe Microscopy – Principle of Operation, Instrumentation, and Probes. in *Nanotribology and*

Nanomechanics I 37–110 (Springer, Berlin, Heidelberg, 2011). doi:10.1007/978-3-642-15283-2_2

133. Kholkin, A. L., Kalinin, S. V., Roelofs, A. & Gruverman, A. Review of Ferroelectric Domain Imaging by Piezoresponse Force Microscopy. in *Scanning Probe Microscopy* (eds. Kalinin, S. & Gruverman, A.) 173–214 (Springer New York, 2007). doi:10.1007/978-0-387-28668-6_7
134. Horcas, I. *et al.* WSXM: A software for scanning probe microscopy and a tool for nanotechnology. *Rev. Sci. Instrum.* **78,** 013705 (2007).
135. Nečas, D. & Klapetek, P. Gwyddion: an open-source software for SPM data analysis. *Open Phys.* **10,** 181–188 (2011).
136. Kusz, J., Suchanicz, J., Böhm, H. & Warczewski, J. High temperature X-ray single crystal study of $Na_{1/2}Bi_{1/2}TiO_3$. *Phase Transit.* **70,** 223–229 (1999).
137. Suchanicz, J. Peculiarities of phase transitions in $Na_{0.5}Bi_{0.5}TiO_3$. *Ferroelectrics* **190,** 77–81 (1997).
138. Hiruma, Y., Nagata, H. & Takenaka, T. Thermal depoling process and piezoelectric properties of bismuth sodium titanate ceramics. *J. Appl. Phys.* **105,** 084112 (2009).
139. Schütz, D. *et al.* Lone-Pair-Induced Covalency as the Cause of Temperature- and Field-Induced Instabilities in Bismuth Sodium Titanate. *Adv. Funct. Mater.* **22,** 2285–2294 (2012).
140. Dorcet, V. & Trolliard, G. A transmission electron microscopy study of the A-site disordered perovskite $Na_{0.5}Bi_{0.5}TiO_3$. *Acta Mater.* **56,** 1753–1761 (2008).
141. Suchanicz, J., Roleder, K., Kwapuliński, J. & Jankowska-Sumara, I. Dielectric and structural relaxation phenomena in $Na_{0.5}Bi_{0.5}TiO_3$ single crystal. *Phase Transit.* **57,** 173–182 (1996).
142. Isupov, V. A. Ferroelectric $Na_{0.5}Bi_{0.5}TiO_3$ and $K_{0.5}Bi_{0.5}TiO_3$ Perovskites and Their Solid Solutions. *Ferroelectrics* **315,** 123–147 (2005).

143. Park, S.-E., Chung, S.-J., Kim, I.-T. & Hong, K. S. Nonstoichiometry and the Long-Range Cation Ordering in Crystals of $(Na_{1/2}Bi_{1/2})TiO_3$. *J. Am. Ceram. Soc.* **77,** 2641–2647 (1994).

144. Balagurov, A. M. *et al.* The rhombohedral phase with incommensurate modulation in $Na_{1/2}Bi_{1/2}TiO_3$. *Phase Transit.* **79,** 163–173 (2006).

145. Petzelt, J. Soft Mode Behavior in Cubic and Tetragonal $BaTiO_3$ Crystals and Ceramics: Review on the Results of Dielectric Spectroscopy. *Ferroelectrics* **375,** 156–164 (2008).

146. Luspin, Y., Servoin, J. L. & Gervais, F. Soft mode spectroscopy in barium titanate. *J. Phys. C Solid State Phys.* **13,** 3761 (1980).

147. Heywang, W., Lubitz, K. & Wersing, W. *Piezoelectricity: Evolution and Future of a Technology*. (Springer Science & Business Media, 2008).

148. Berlincourt, D. Piezoelectric ceramic compositional development. *J. Acoust. Soc. Am.* **91,** 3034–3040 (1992).

149. Chen, Y.-H., Hirose, S., Viehland, D., Takahashi, S. & Uchino, K. Mn-Modified $Pb(Mg_{1/3}Nb_{2/3})O_3$–$PbTiO_3$ Ceramics: Improved Mechanical Quality Factors for High-Power Transducer Applications. *Jpn. J. Appl. Phys.* **39,** 4843 (2000).

150. Priya, S., Uchino, K. & Viehland, D. Crystal Growth and Piezoelectric Properties of Mn-Substituted $Pb(Zn_{1/3}Nb_{2/3})O_3$ Single Crystal. *Jpn. J. Appl. Phys.* **40,** L1044 (2001).

151. Luo, L., Li, W., Zhu, Y. & Wang, J. Growth and characteristics of Mn-doped PMN–PT single crystals. *Solid State Commun.* **149,** 978–981 (2009).

152. Kamiya, T., Suzuki, T., Tsurumi, T. & Daimon, M. Effects of Manganese Addition on Piezoelectric Properties of $Pb(Zr_{0.5}Ti_{0.5})O_3$. *Jpn. J. Appl. Phys.* **31,** 3058 (1992).

153. Goldschmidt, V. M. Die Gesetze der Krystallochemie. *Naturwissenschaften* **14,** 477–485 (1926).

154. Roth, W. L. & DeVries, R. C. Crystal and Magnetic Structure of $PbCrO_3$. *J. Appl. Phys.* **38,** 951–952 (1967).

155. Arévalo-López, Á. M. & Alario-Franco, M. Á. Structural Percolation in the $PbM_{1-x}M_x'O_3$ (M, M′ =Ti, Cr, and V) Perovskites. *Inorg. Chem.* **50,** 7136–7141 (2011).

156. Bousquet, M. *et al.* Optical properties of an epitaxial $Na_{0.5}Bi_{0.5}TiO_3$ thin film grown by laser ablation: Experimental approach and density functional theory calculations. *J. Appl. Phys.* **107,** 104107 (2010).

157. Li, M. *et al.* A family of oxide ion conductors based on the ferroelectric perovskite $Na_{0.5}Bi_{0.5}TiO_3$. *Nat. Mater.* **13,** 31–35 (2014).

158. Maier, R. A. & Randall, C. A. Low Temperature Ionic Conductivity of an Acceptor-Doped Perovskite: II. Impedance of Single-Crystal $BaTiO_3$. *J. Am. Ceram. Soc.* **99,** 3360–3366 (2016).

159. Maier, R. A. & Randall, C. A. Low-Temperature Ionic Conductivity of an Acceptor-Doped Perovskite: I. Impedance of Single-Crystal $SrTiO_3$. *J. Am. Ceram. Soc.* **99,** 3350–3359 (2016).

160. Koch, L. *et al.* Ionic conductivity of acceptor doped sodium bismuth titanate: influence of dopants, phase transitions and defect associates. *J. Mater. Chem. C* **5,** 8958–8965 (2017).

161. Kutnjak, Z., Petzelt, J. & Blinc, R. The giant electromechanical response in ferroelectric relaxors as a critical phenomenon. *Nature* **441,** 956–959 (2006).

162. Ishibashi, Y. & Iwata, M. Theory of Morphotropic Phase Boundary in Solid-Solution Systems of Perovskite-Type Oxide Ferroelectrics: Elastic Properties. *Jpn. J. Appl. Phys.* **38,** 1454 (1999).

163. Ishibashi, Y. & Iwata, M. Morphotropic Phase Boundary in Solid Solution Systems of Perovskite-Type Oxide Ferroelectrics. *Jpn. J. Appl. Phys.* **37,** L985 (1998).

164. Shrout, T. R., Chang, Z. P., Kim, N. & Markgraf, S. Dielectric behavior of single crystals near the $(1-x)\ Pb(Mg_{1/3}Nb_{2/3})O_3$-$(x)PbTiO_3$ morphotropic phase boundary. *Ferroelectr. Lett. Sect.* **12,** 63–69 (1990).

165. Zhang Qinhui, Zhao Xiangyong, Sun Renbing & Luo Haosu. Crystal growth and electric properties of lead-free NBT-BT at compositions near the morphotropic phase boundary. *Phys. Status Solidi A* **208,** 1012–1020 (2011).

166. Sawaguchi, E., Maniwa, H. & Hoshino, S. Antiferroelectric Structure of Lead Zirconate. *Phys. Rev.* **83,** 1078–1078 (1951).

167. Sawaguchi, E., Shirane, G. & Takagi, Y. Phase Transition in Lead Zirconate. *J. Phys. Soc. Jpn.* **6,** 333–339 (1951).

168. Kuwata, J., Uchino, K. & Nomura, S. Dielectric and Piezoelectric Properties of $0.91Pb(Zn_{1/3}Nb_{2/3})O_3$-$0.09PbTiO_3$ Single Crystals. *Jpn. J. Appl. Phys.* **21,** 1298 (1982).

169. Ye, Z.-G. High-Performance Piezoelectric Single Crystals of Complex Perovskite Solid Solutions. *MRS Bull.* **34,** 277–283 (2009).

170. Zhang, S. & Li, F. High performance ferroelectric relaxor-$PbTiO_3$ single crystals: Status and perspective. *J. Appl. Phys.* **111,** 031301 (2012).

171. Ahart, M. *et al.* Origin of morphotropic phase boundaries in ferroelectrics. *Nature* **451,** 545–548 (2008).

172. McQuade, R. R. & Dolgos, M. R. A review of the structure-property relationships in lead-free piezoelectric $(1-x)Na_{0.5}Bi_{0.5}TiO_3$–$(x)BaTiO_3$. *J. Solid State Chem.* **242,** 140–147 (2016).

173. Shvartsman, V. V. & Lupascu, D. C. Lead-Free Relaxor Ferroelectrics. *J. Am. Ceram. Soc.* **95,** 1–26 (2012).

174. Guo, Y. *et al.* The phase transition sequence and the location of the morphotropic phase boundary region in $(1 - x)[Pb (Mg_{1/3}Nb_{2/3})O_3]$–$xPbTiO_3$ single crystal. *J. Phys. Condens. Matter* **15,** L77 (2003).

175. Choi, S. W., Shrout, T. R., Jang, S. J. & Bhalla, A. S. Morphotropic phase boundary in $Pb (Mg_{1/3}Nb_{2/3}) O_3$-$PbTiO_3$ system. *Mater. Lett.* **8,** 253–255 (1989).

176. Noblanc, O., Gaucher, P. & Calvarin, G. Structural and dielectric studies of $Pb(Mg_{1/3}Nb_{2/3})O_3$–$PbTiO_3$ ferroelectric solid solutions around the morphotropic boundary. *J. Appl. Phys.* **79,** 4291–4297 (1996).

177. Bokov, A. A. & Ye, Z.-G. Dielectric relaxation in relaxor ferroelectrics. *J. Adv. Dielectr.* **02,** 1241010 (2012).

178. Ye, Z.-G., Noheda, B., Dong, M., Cox, D. & Shirane, G. Monoclinic phase in the relaxor-based piezoelectric/ferroelectric $PbMg_{1/3}Nb_{2/3}O_3$-$PbTiO_3$ system. *Phys. Rev. B* **64,** 184114 (2001).

179. Xu, G., Viehland, D., Li, J. F., Gehring, P. M. & Shirane, G. Evidence of decoupled lattice distortion and ferroelectric polarization in the relaxor PMN-PT. *Phys. Rev. B* **68,** 212410 (2003).

180. Dkhil, B. *et al.* Local and long range polar order in the relaxor-ferroelectric compounds $PbMg_{1/3}Nb_{2/3}O_3$ and $PbMg_{0.3}Nb_{0.6}Ti_{0.1}O_3$. *Phys. Rev. B* **65,** 024104 (2001).

181. Slodczyk, A., Daniel, P. & Kania, A. Local phenomena of (1-$PbMg_{1/3}Nb_{2/3}O_3$-x$PbTiO_3$ single crystals ($0 \le x \le 0.38$) studied by Raman scattering. *Phys. Rev. B* **77,** 184114 (2008).

182. Ye, Z.-G. *et al.* Development of ferroelectric order in relaxor (1-x)$PbMg_{1/3}Nb_{2/3}O_3$-x$PbTiO_3$ (0<~x<~0.15). *Phys. Rev. B* **67,** 104104 (2003).

183. Gehring, P. M., Chen, W., Ye, Z.-G. & Shirane, G. The non-rhombohedral low-temperature structure of PMN–10% PT. *J. Phys. Condens. Matter* **16,** 7113 (2004).

184. Ge, W. *et al.* Lead-free and lead-based ABO_3 perovskite relaxors with mixed-valence A-site and B-site disorder: Comparative neutron scattering structural study of $(Na_{1/2}Bi_{1/2})TiO_3$ and $Pb(Mg_{1/3}Nb_{2/3})O_3$. *Phys. Rev. B* **88,** 174115 (2013).

185. Takenaka, H., Grinberg, I., Liu, S. & Rappe, A. M. Slush-like polar structures in single-crystal relaxors. *Nature* **546,** 391–395 (2017).

186. Kim, T. H., Kojima, S. & Ko, J.-H. Electric field effects on the dielectric and acoustic anomalies of $Pb[(Mg_{1/3}Nb_{2/3})_{0.83}Ti_{0.17}]O_3$ single crystals studied by dielectric and Brillouin spectroscopies. *Curr. Appl. Phys.* **14,** 1643–1648 (2014).

187. Peercy, P. S. Observation of an Underdamped ‘Soft’ Mode in Potassium Dihydrogen Phosphate. *Phys. Rev. Lett.* **31,** 379–382 (1973).

188. Kozlov, G. V., Volkov, A. A., Scott, J. F., Feldkamp, G. E. & Petzelt, J. Millimeter-wavelength spectroscopy of the ferroelectric phase transition in tris-sarcosine calcium chloride [($CH_3NHCH_2OOH)_3CaCl_2$]. *Phys. Rev. B* **28,** 255–261 (1983).

189. Mackeviciute, R. *et al.* The perfect soft mode: giant phonon instability in a ferroelectric. *J. Phys. Condens. Matter* **25,** 212201 (2013).

190. Blinc, R. Order and Disorder in Perovskites and Relaxor Ferroelectrics. in *Ferro- and Antiferroelectricity* (eds. Dalal, N. S. & Bussmann-Holder, A.) 51–67 (Springer Berlin Heidelberg, 2007). doi:10.1007/430_2006_050

191. Helal, M. A., Aftabuzzaman, M., Svirskas, S., Banys, J. & Kojima, S. Temperature evolution of central peaks and effect of electric field in relaxor ferroelectric $0.83Pb(Mg_{1/3}Nb_{2/3})O_3$–$0.17PbTiO_3$ single crystals. *Jpn. J. Appl. Phys.* **56,** 10PB03 (2017).

192. Svirskas, Š., Banys, J. & Kojima, S. Broadband dielectric spectroscopy of Pb-based relaxor ferroelectric $(1\text{-}x)Pb(Mg_{1/3}Nb_{2/3})O_3\text{-}xPbTiO_3$ with intermediate random fields. *J. Appl. Phys.* **121,** 134101 (2017).

193. Shvartsman, V. V. & Kholkin, A. L. Domain structure of $0.8Pb(Mg_{1/3}Nb_{2/3})O_3\text{-}0.2PbTiO_3$ studied by piezoresponse force microscopy. *Phys. Rev. B* **69,** 014102 (2004).

194. Shvartsman, V. V. & Kholkin, A. L. Evolution of nanodomains in $0.9PbMg_{1/3}Nb_{2/3}O_3\text{-}0.1PbTiO_3$ single crystals. *J. Appl. Phys.* **101,** 064108 (2007).

195. Fang, F., Luo, X. & Yang, W. Polarization rotation and multiphase coexistence for Pb(Mg$_{1/3}$Nb<sub>2/3</sub)O$_3$-PbTiO$_3$ single crystals at the morphotropic phase boundary under electric loading. *Phys. Rev. B* **79,** 174118 (2009).

196. Fu, H. & Cohen, R. E. Polarization rotation mechanism for ultrahigh electromechanical response in single-crystal piezoelectrics. *Nature* **403,** 281–283 (2000).

197. Svirskas, Š. *et al.* Dynamics of Phase Transition in 0.4NBT-0.4ST-0.2PT Solid Solution. *Integr. Ferroelectr.* **134,** 81–87 (2012).

198. Nilsen, W. G. & Skinner, J. G. Raman Spectrum of Strontium Titanate. *J. Chem. Phys.* **48,** 2240–2248 (1968).

199. Hall, D. A. Review Nonlinearity in piezoelectric ceramics. *J. Mater. Sci.* **36,** 4575–4601

200. Zhang, Q., Pan, W., Bhalla, A. & Cross, L. E. Electrostrictive and Dielectric Response in Lead Magnesium Niobate–Lead Titanate (0.9PMN-0.1PT) and Lead Lanthanum Zirconate Titanate (PLZT 9.5/65/35) under Variation of Temperature and Electric Field. *J. Am. Ceram. Soc.* **72,** 599–604 (1989).

201. Li, F., Jin, L. & Guo, R. High electrostrictive coefficient Q_{33} in lead-free $Ba(Zr_{0.2}Ti_{0.8})O_3$-$x(Ba_{0.7}Ca_{0.3})TiO_3$ piezoelectric ceramics. *Appl. Phys. Lett.* **105,** 232903 (2014).

202. Zuo, R. *et al.* Giant electrostrictive effects of $NaNbO_3$-$BaTiO_3$ lead-free relaxor ferroelectrics. *Appl. Phys. Lett.* **108,** 232904 (2016).

203. Kuwata, J., Uchino, K. & Nomura, S. Electrostrictive Coefficients of $Pb(Mg_{1/3}\,Nb_{2/3})O_3$ Ceramics. *Jpn. J. Appl. Phys.* **19,** 2099–2103 (1980).

204. Uchino, K., Nomura, S., Cross, L. E., Jang, S. J. & Newnham, R. E. Electrostrictive effect in lead magnesium niobate single crystals. *J. Appl. Phys.* **51,** 1142–1145 (1980).

205. Shvartsman, V. V., Dec, J., Miga, S., Łukasiewicz, T. & Kleemann, W. Ferroelectric Domains in $Sr_xBa_{1-x}Nb_2O_6$ Single Crystals ($0.4 \le \times \le 0.75$). *Ferroelectrics* **376,** 1–8 (2008).

206. Arlt, G. Twinning in ferroelectric and ferroelastic ceramics: stress relief. *J. Mater. Sci.* **25,** 2655–2666 (1990).

207. Shvartsman, V. V. & Kholkin, A. L. Investigation of the ferroelectric-relaxor transition in $PbMg_{1/3}Nb_{2/3}O_3$–$PbTiO_3$ ceramics by piezoresponse force microscopy. *J. Appl. Phys.* **108,** 042007 (2010).

208. Kroupa, J. *et al.* Second harmonic generation and dielectric study of the fine and coarse grain PMN-35PT ceramics. *Phase Transit.* **81,** 1059–1064 (2008).

APPENDIX I

Frequency dependences of order-disorder type 2nd order phase transition

The temperature dependence of dielectric permittivity was modelled in framework of order-disorder model. Figure 1 represents the temperature dependence of inverse relaxation time. The equation of this function is as follows:

$$\begin{cases} \frac{1}{\tau} = \frac{1}{\tau_0} + A_1(T - T_C), \ T > \ T_C \\ \frac{1}{\tau} = \frac{1}{\tau_0} - A_2(T - T_C), \ T < \ T_C \end{cases} \tag{1}$$

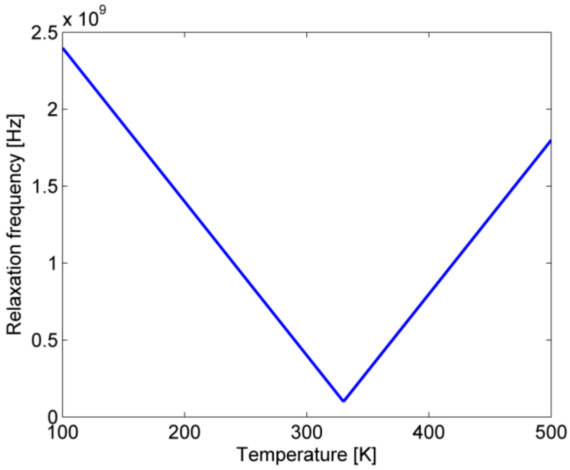

Figure 4.2.1 Temperature dependence of relaxation frequency.

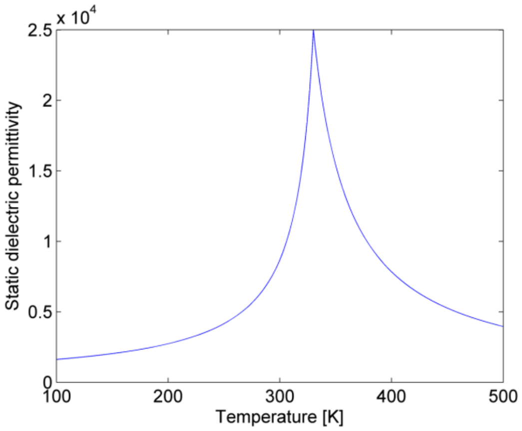

Figure 4.2.2 Temperature dependence of static dielectric permittivity

The Curie temperature T_C = 330 K.

The frequency dependence of complex dielectric permittivity was modelled according to the Cole-Cole equation:

$$\varepsilon^*(\omega) = \varepsilon(\infty) + \frac{\varepsilon(0)-\varepsilon(\infty)}{1+(\mathrm{i}\omega\tau)^{1-\alpha}} \tag{2}$$

$\varepsilon(\infty) = 100$ is the phonon and electron contribution to dielectric permittivity. This parameter is independent of temperature. The static dielectric permittivity $\varepsilon(0)$ was taken to be temperature dependent according to Curie-Weiss law (for the 2nd order phase transition).

$$\begin{cases} \frac{1}{\varepsilon(0)} = \frac{T-T_C}{2C}, \ T > T_C \\ \frac{1}{\varepsilon(0)} = \frac{T_C-T}{C}, \ T < T_C \end{cases} \tag{3}$$

The temperature dependence of static dielectric permittivity is plotted in Figure 2. For the sake of simplicity the Cole-Cole α was taken to be temperature independent as well. The temperature dependences of dielectric permittivity at different frequencies are obtained by inserting Eq. 1 and Eq. 3 to Eq. 2.

Afterwards, the temperature dependences of dielectric permittivity at different frequencies were plotted (Figure 3). Four graphs represent different values of α parameter ($\alpha(T) = const$). Figure 3a represents the scenario where $\alpha = 0$ (i. e. Eq 2 reduces to simple Debye relaxation model). In this case we clearly observe well pronounced minimum in the temperature dependences of dielectric permittivity. When the distribution function is broadened ($\alpha = 0.1; 0.2$) the minimum is still observed. We see that in Figure 3c the minimum is slightly more smeared out. Finally when we reach the $\alpha = 0.4$ minimum is masked and is not observed in any frequencies.

Another interesting point which should be noted, that in figure 3d one can observe slight temperature shift of dielectric maximum at different frequencies. It resembles the relaxor behaviour (although these peaks are quite sharp in comparison to relaxor behaviour but one has to note that this is rough model).

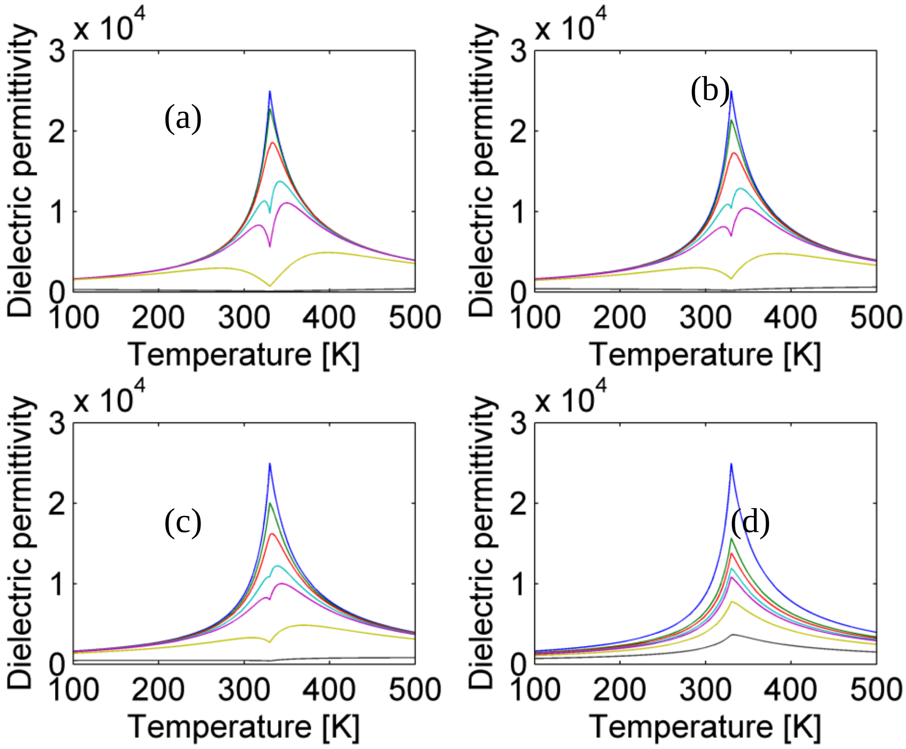

Figure 4.2.3 Temperature dependence of real part of dielectric permittivity with different parameter α: (a) $\alpha = 0$; (b) $\alpha = 0.1$; (c) $\alpha = 0.2$; (d) $\alpha = 0.4$.

+

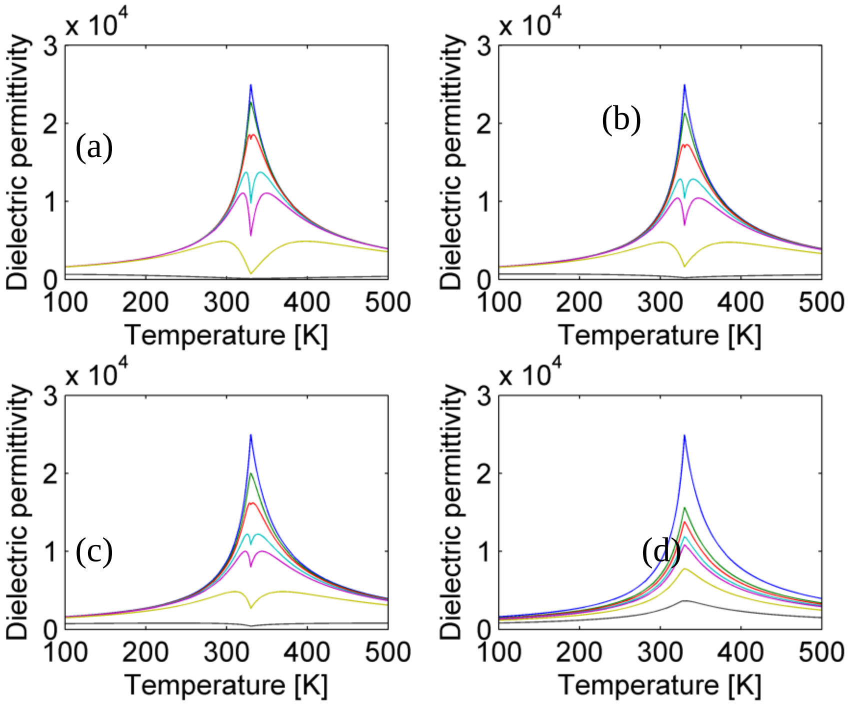

Figure 4.2.4 Temperature dependence of real part of dielectric permittivity with different parameter α: (a) α=0; (b) α=0.1; (c) α=0.2; (d) α=0.4.

Figure 4 represents the temperature dependence of dielectric permittivity. The difference is that the pre exponential factor in Eq. (1) below phase transition is taken to be $A_2 = 2A_1$.

In conclusion, this proves the statements we earlier wrote in the manuscript. We are not sure whether it is necessary to include these data in the manuscript. Maybe it is worth adding it to supplementary material if it is possible by the journal we are planning to submit the article to.

Also, we are doing Modified Curie-Weiss fits for PMN single crystals from two different sources. Unfortunately, we do not have data at waveguide frequencies. We also have results on PMN-10PT crystals which we will analyse. These results will be presented very soon.

Figure 5 represents the temperature dependence of piezoelectric coefficient d_{33} and electrostriction coefficient Q_{11}. These coefficients were determined by the fitting of strain vs. Electric field and strain vs. Square of polarization respectively.

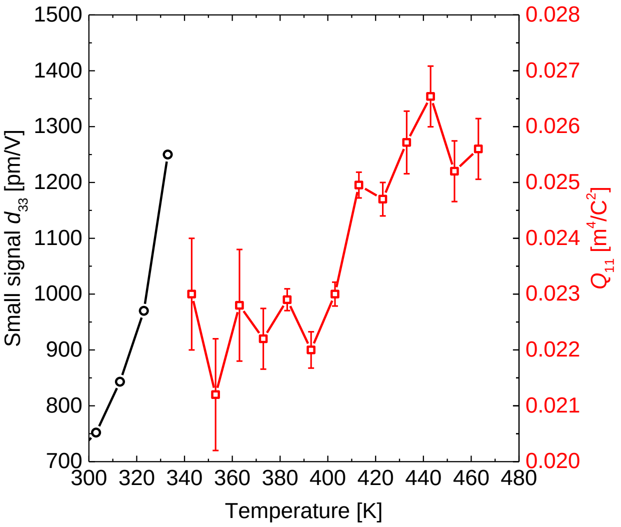

Figure 5 Temperature dependence of piezoelectric coefficient d_{33} and electrostriction coefficient Q_{11}.

APPENDIX II

Structural properties of 0.1NBT-0.6ST-0.3PT solid solutions

Figure S1 represents the temperature dependences of the real part of dielectric permittivity on heating and cooling cycles. A thermal hysteresis is clearly observed thus allowing us to determine that the phase transition is of 1st order. The black curve in fig. S1 represents the temperature dependence of permittivity for the poled sample (sample was poled and then heated). Both experiments gave consistent results. The shift of the phase transition temperature on heating was observed for the poled sample. Different samples were used for this experiment so the discrepancy between the permittivity values might be associated with the errors of sample dimensions.

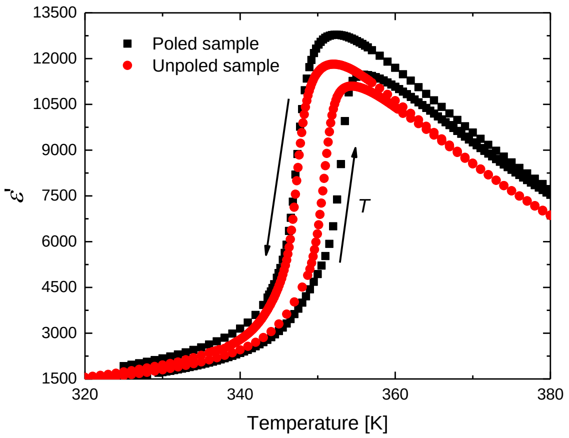

Figure S1. Temperature dependence of dielectric permittivity on heating and cooling cycles. Heating and cooling rate was 0.5 K/min during the measurements.

Figure S2 (a) represents X-ray powder difraction patterns of a 0.1NBT-0.6ST-0.3PT powder at different temperatures. The powder was ground from the ceramics. The experiments were carried out on heating. The phase transition temperature is around 350 – 360 K. Rietveld refinement revealed that the ceramics consist of single phase and the phase transition is from the cubic to the tetragonal phase. The temperature dependences of lattice parameters are presented in Figure S2 (b).

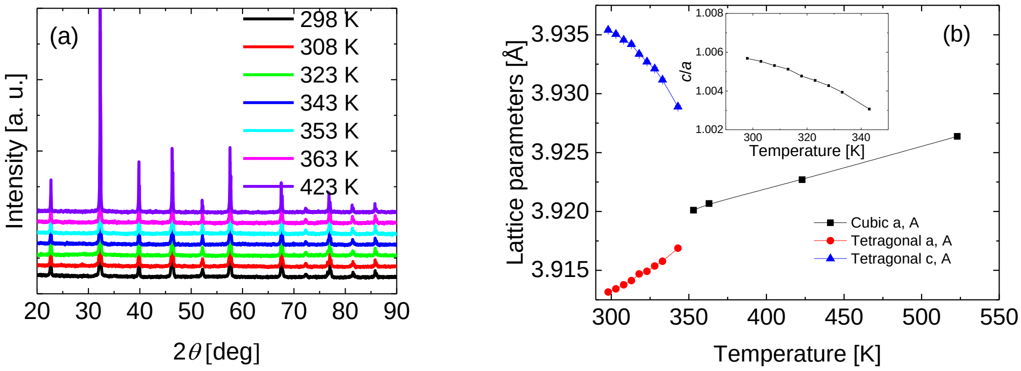

Figure S2 (a) XRD patterns of 0.1NBT-0.6ST-0.3PT powder; (b) Temperature dependence of lattice parameters obtained by Rietveld refinement (inset represents temperature dependence of tetragonality factor);

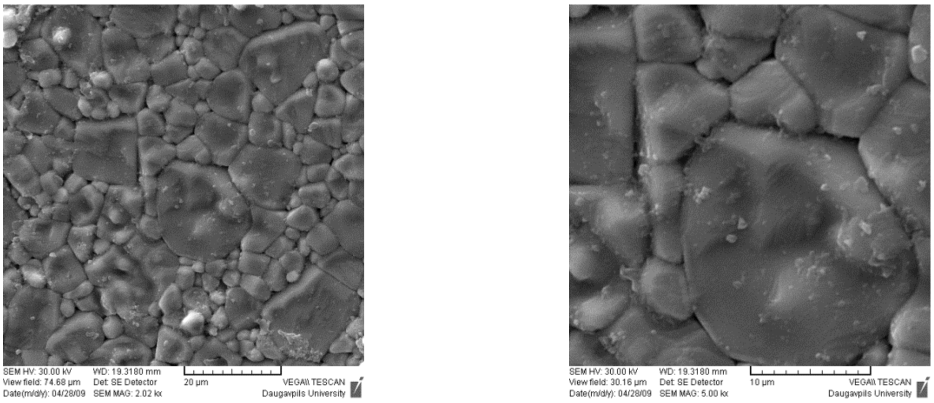

Figure S3 SEM micrographs of 0.1NBT-0.6ST-0.3PT ceramics at room temperature.

SEM micrographs of the 0.1NBT-0.6ST-0.3PT ceramics are depicted in figure S3. The micrographs clearly show that the ceramics consist of two types of grains. There are large micron-sized grains (can reach up to 10 micron in size). Other grains are submicron sized. These micrographs confirm the existence of a bimodal distribution of grain size.

The EDS mapping of ceramics is represented in Fig. S4. The EDS reveals that the ratio of A-site elements in the perovskite lattice is consistent with the current composition. The elements are distributed homogenously in the investigated region. There are few grains which occupy < 10 % of the scanned area where the lead surpasses the amount of strontium but this is not a general trend in the ceramic (it is not secondary phases, just a deviations from the initial composition). Such small amount can be negligible when considering the macroscopic response of the material. It might explain larger PFM signal in some parts of material but it cannot be generalized for all the smaller grains.

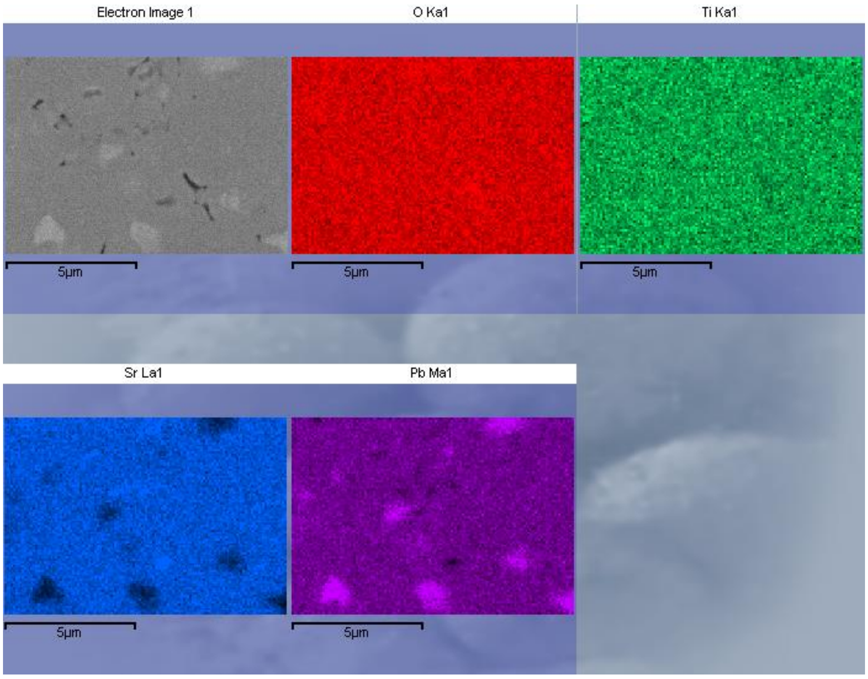

Figure S4 The distribution of different elements in 0.1NBT-0.6ST-0.3PT by EDS analysis.

Figure S5 shows results of TOF-SIMS analysis of the sample. One can see that, in general, the relevant elements (Pb, Sr, Bi) are homogenously distributed across the sample surface. However, there are some grains enriched with Pb against Sr (Fig. S5 d). They occupy approximately 4% of the total sample area.

Figure S6 represents the temperature dependence of inverse permittivity at 5 kHz frequency. The open blue dots represent the temperature dependence of inverse static permittivity. The static permittivity was obtained from the approximation of the frequency dependences of the complex dielectric permittivity. The 5 kHz data points and the static permittivity are in agreement. The deviation from the Curie-Weiss law is evident in this figure and persist at least 100 K above T_C.

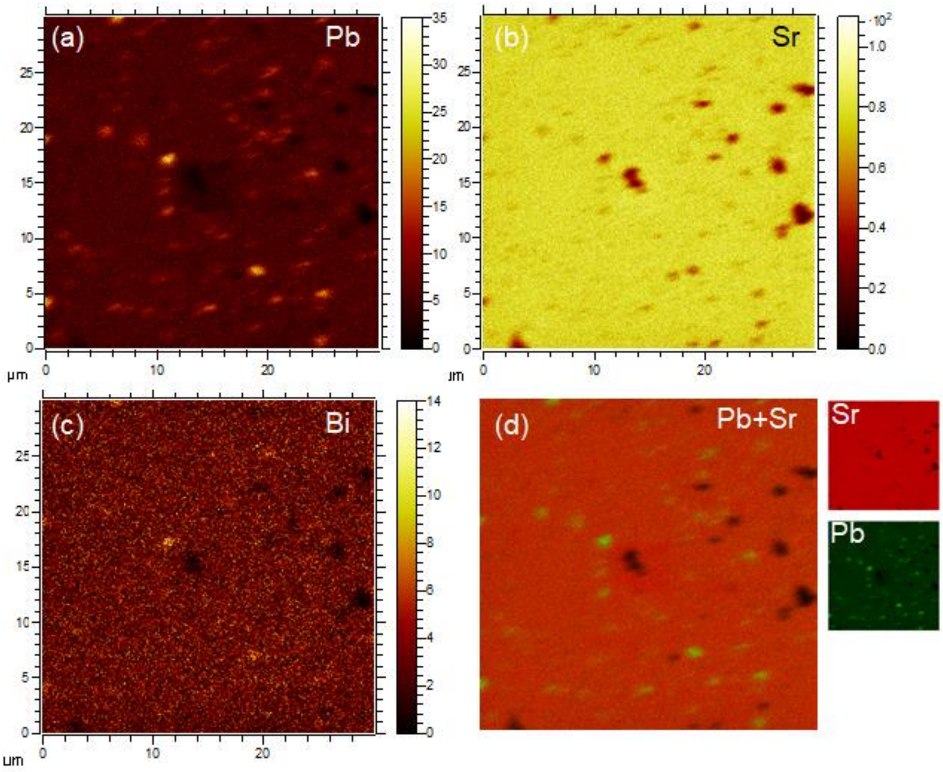

Figure S5. Time of flight secondary ion mass spectrometry. (a)-(c) Maps of A-site cation distributions: Pb (a), Sr (b), and Bi (c). (d) A combined map of Pb and Sr distribution. Green spots in (d) correspond to Pb-enriched grains, dark spots are pores. The size of the shown area is 30×30 μm^2.

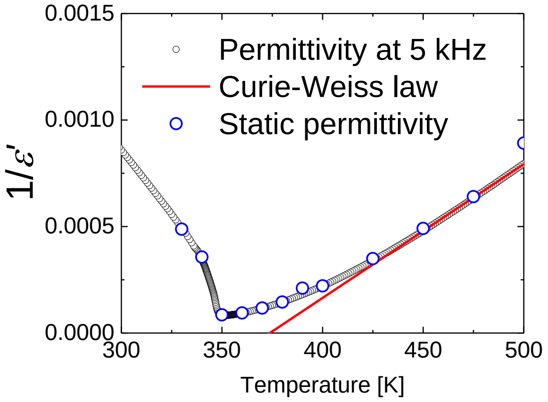

Figure S6 Temperature dependence of inverse dielectric permittivity. Solid line represents the fit by the Curie-Weiss law. The experimental points are taken at 5 kHz frequency. Data at this frequency corresponds to static permittivity, because no dispersion was observed between 5 kHz and 10 MHz.